Liquid Crystalline Thermosetting Polymers as Protective Coatings for Aerospace

Liquid Crystalline Thermosetting Polymers as Protective Coatings for Aerospace

Proefschrift

ter verkrijging van de graad van doctor aan de
Technische Universiteit Delft, op gezag van de
Rector Magnificus prof.ir. K.C.A.M. Luyben, voorzitter van het
College voor Promoties, in het openbaar te verdedigen op dinsdag
16 oktober 2012 om 10.00 uur

door

Gustavo Luis GUERRIERO
Master of Science in Materials Engineering,
Prof. Jorge Sabato Institute of Technology, Buenos Aires, Argentinië
geboren te Isidro Casanova, Buenos Aires, Argentinië

Dit proefschrift is goedgekeurd door de promotor:

Prof.dr.ir. R. Benedictus

Samenstelling promotiecommissie:

Rector Magnificus,	Voorzitter
Prof.dr.ir. R. Benedictus	Technische Universiteit Delft, promotor
Prof.dr.ir. H.E.J.G. Schlangen	Technische Universiteit Delft
Prof.dr. S.J. Picken	Technische Universiteit Delft
Prof.dr.ir. Remko Akkerman	Universiteit Twente
Prof.dr. Joris Degrieck	Universiteit Gent, België
Dr.ir. R.C. Alderliesten	Technische Universiteit Delft
Dr. S.J. Garcia Espallargas	Technische Universiteit Delft
Prof.dr. T.J. Dingemans	Technische Universiteit Delft, reservelid

Dr.ir. R. Alderliesten heeft als begeleider in belangrijke mate aan de totstandkoming van het proefschrift bijgedragen.

This work was financially supported by the CleanSky Eco-Design ITD work packages 211-03 and 212-02, the CleanEra Project, and the Delft University of Technology.

ISBN: 978-90-8891-490-4

Keywords: Liquid crystalline polymers, Thermosets, Coatings, Mechanical properties, Environmental resistance, Atmospheric plasma spraying.

Published by: Uitgeverij BOXPress, Oisterwijk

Dedicated to the loving memory of Aunty Silvia.

Dedicado a la querida memoria de la Tia Silvia.

1945 – 2011

Summary

Environmental regulations are driving the development of new aerospace coating systems, mainly to eliminate chromates and reduce volatile organic compound (VOC) emissions. Among the various potential options for new coating materials, liquid crystalline polymers (LCPs) are attractive due to their unique combination of mechanical properties and chemical resistance. Their use, however, has been limited mainly due to poor adhesion properties. Thermotropic liquid crystalline thermosets displayed the properties of traditional LCPs, while having the potential to overcome their disadvantages. The present research has been set to investigate the real potential of phenylethynyl terminated liquid crystalline thermosets (LCTs) for coating applications.

The coatings were initially manufactured by melt-pressing the LCT resins onto aluminum substrates. This method was selected mainly due to its simplicity and minimal powder requirements. As a first step, the effects of the thermal curing and the molecular weight of the coating resins were investigated. Then, the influence of temperature and molecular orientation were examined. Subsequently, the adhesion and the environmental resistance of the LCT coatings were analyzed. Finally, the applicability of LCTs on aluminum and composite substrates using atmospheric plasma spraying (APS) was explored to address the industrial limitations of melt-pressing (on size, shape, and thermal resistance of the substrate).

Being the first approach to the use of these LCTs as coatings, the present work has contributed to the knowledge and understanding of several aspects of the coating. The incorporation of the end-groups was found to promote the adhesion of the coating compared to the thermoplastic Vectra®, while it did not affect the environmental resistance. In addition, the new polymer chemistry allowed the polymers to be ground into a powder suitable for more versatile deposition methods like APS, expanding the range of applications.

These LCTs, however, also present several disadvantages. An extra curing step at high temperature is required, during which, the properties are not significantly improved. In addition, the LCTs investigated here become more brittle after curing, which can be a disadvantage for tribological applications. Furthermore, mechanical properties such as the elastic modulus are not significantly higher than those of the thermoplastic LCP; and the formation of aggregate-aggregate interfaces constitute paths for crack propagation. Finally, untreated coating substrate interfaces constitute paths for environmental attack.

The main characteristic of these coatings appeared to be their high chemical resistance and low permeability. These coatings are, therefore, applicable for the protection of surfaces exposed to aggressive liquids or flowing gases. Examples include heat exchangers, gearbox housings, undercarriage components, flooring, and hatches. Since these coatings constitute a passive protection, however, the development of a coating system that includes an active protection would be required to extend coating durability.

Samenvatting

Milieuregelgeving drijft de ontwikkeling van nieuwe coatingsystemen voor de lucht- en ruimtevaart. De ontwikkeling is vooral gericht op het elimineren van chromaten en het terugdringen van de uitstoot van vluchtige organische stoffen. Uit de verschillende opties voor nieuwe coatingmaterialen zijn vloeibaar-kristallijne polymeren (VKPs) aantrekkelijk dankzij hun unieke combinatie van mechanische eigenschappen en chemische weerstand. Hun toepassing is echter gelimiteerd door de slechte hechtingseigenschappen. Thermotropische vloeibaar-kristallijne thermoharders vertoonden dezelfde eigenschappen als traditionele VKPs, terwijl ze ook het potentieel hadden om hun nadelen te overwinnen. Het doel van het huidige onderzoek was het onderzoeken van het werkelijke potentieel voor toepassing als coatingmateriaal van phenylethynylbeïndigde vloeibaar-kristallijne thermoharders (VKTs).

De coatings warden initieel vervaardigd door de VKT harsen op een aluminium substraat te smeltpersen. Deze methode werd geselecteerd omwille van haar eenvoudigheid en de kleine hoeveelheid benodigd poeder. Als eerste werden de effecten van het thermisch uitharden en het molecuulgewicht van de coatingharsen onderzocht. Daarna werden de invloed van temperatuur en molecuuloriëntatie onderzocht. Vervolgens werden de hechting en de weerstand tegen omgevingsinvloeden geanalyseerd. Tot slot werd het aanbrengen van VKTs op aluminium- en composietsubstraten met behulp van atmosferisch plasmasproeien (APS) onderzocht, als mogelijkheid om de industriële beperkingen (wat betreft grootte, vorm en thermische weerstand van het substraat) van smeltpersen te ondervangen.

Als eerste aanpak voor het gebruik van deze VKTs als coating, heeft dit werk bijgedragen aan kennis en begrip van een aantal aspecten van de coating. Het opnemen van de eind-groepen bleek de hechting van de coating te verstreken in vergelijking met de termoplast Vectra®, zonder de weerstand tegen omgevingsinvloeden te beïnvloeden. Daarnaast liet de nieuwe polymeerchemie toe dat de polymeren werden vermalen tot een poeder dat geschikt was voor meer veelzijdige afzetmethodes zoals APS, wat het bereik van toepassingen vergrotte.

Deze VKTs hebben echter ook enkele nadelen. Er is een extra uithardingsstap benodigd bij hoge temperatuur. Tijdens deze stap worden de eigenschappen niet significant verbeterd. Daarnaast worden de onderzochte VKTs na uitharding bros, wat een nadeel kan zijn voor tribologische toepassingen. Verder zijn de mechanische eigenschappen zoals de elasticiteitsmodulus niet significant hoger dan die van het thermoplastische VKP en bied de vorming van aggregaat-aggregaat grensvlakken een pad

voor scheurgroei. Ten slotte bieden onbehandelde coating-substraat grensvlakken een pad voor inwerking van omgevingsinvloeden.

De belangrijkste eigenschap van deze coatings bleek hun hoge chemische weerstand en lage permeabiliteit te zijn. Deze coatings zijn dus toepasbaar voor de bescherming van oppervlaktes die worden blootgesteld aan agressieve vloeistoffen of stromende gassen. Voorbeelden zijn warmtewisselaars, versnellingskastbehuizingen, landingsgestelonderdelen, vloeronderdelen en luiken. Aangezien deze coatings een passieve bescherming bieden, zou het ontwikkelen van een coatingsysteem dat een actieve bescherming bevat benodigd zijn om de duurzaamheid van de coating te vergroten.

Contents

Nomenclature

APS	Atmospheric plasma spraying
CAA	Chromic acid anodization
CF	Carbon fiber
CSM	Continuous stiffness measurement
CTE	Coefficient of thermal expansion
DMTA	Dynamic mechanical thermal analysis
DSC	Differential scanning calorimetry
E	Elastic modulus
ER	Elastic recovery
GF	Glass fiber
H	Nano-hardness
HBA	4-hydroxybenzoic acid
HNA	6-hydroxy-2-naphthoic acid
HVOF	High-velocity oxy-fuel
LCP	Liquid crystalline polymer
LCT	Liquid crystalline thermoset
Mn	Number average molecular weight
Mw	Weight average molecular weight
OM	Optical microscopy
PAA	Phosphoric acid anodization
PE	Polyethylene

PE-COOH	N-(4-carboxyphenyl)-4-phenylethynyl-phthalimide
PE-OAc	N-(4-Acetoxyphenyl)-4-phenylethynyl-phthalimide
PEEK	Polyether ether ketone
PEI	Polyetherimide
PEPA	4-(phenyl-ethynyl)-phthalic anhydride
PMMA	Poly(methyl methacrylate)
POM	Polarized optical microscopy
PPS	Polyphenylene sulfide
S	Contact stiffness
SEM	Scanning electron microscopy
TEM	Transmission electron microscopy
TG	Thermogravimetry
Tg	Glass-transition temperature
TLCP	Thermotropic liquid crystalline polymer
TS	Thermal spraying
VOC	Volatile organic compounds

1 Introduction

1.1 Overview

Environmental regulations and functional requirements are driving the development of new coating systems. Liquid crystalline polymers (LCPs) have been in the market for decades, and their superior mechanical properties and chemical resistance are well recognized. These properties, together with their very low thermal expansion, are attractive for the coating industry; however, their low adhesion and difficult processability into coatings has hindered their application in this field. Novel thermosetting LCPs, or liquid crystalline thermosets (LCTs), have the potential to overcome these problems thanks to the engineering of the molecular structure of the polymer.

1.2 Background

The aerospace industry places a high performance demand on the coatings used in aeronautical structures. Vast temperature variations produce dimensional changes on both structure and coating. Temperature and pressure changes also cause condensation of water, which collects inside unpressurised or unheated areas of the structure. With increasing altitude, lower pressures make residual liquid in the coating much more volatile, and the less dense and less polluted atmosphere increases UV radiation. High humidity and salt concentrations in the atmosphere promote weathering and corrosion. Fluids used in the aircraft, such as aggressive phosphate-ester based hydraulic fluids, can attack coatings from the surface or through the interface with the substrate.

Currently, the required adhesion, protection against corrosion and degradation, aesthetics and other specialized functions are obtained using several layers of coatings. Typical coating systems comprise three individual coating layers [1]. The first layer, a conversion coating, is the product of substrate pretreatment. It is usually a very thin ($\leq 10\,\mu m$) inorganic layer that provides corrosion protection and improved adhesion between the substrate and the primer. The primer, which is the second layer, consists of a pigmented organic resin matrix, typically a two component epoxy with a thickness of around $25\,\mu m$, and it is the main provider of corrosion protection. The top-coat is typically a polyurethane resin with thicknesses from 50 to $200\,\mu m$,

and is the main barrier against environmental influences such as extreme climates and ultra-violet rays; it also provides decoration and camouflage.

1.2.1 Problems with current coatings

To meet the high demands, aerospace coatings have been traditionally formulated with ingredients regarded as hazardous either to health or the environment, such as chromate pigments or large quantities of strong solvents. Organic coatings alone are not sufficient to protect an underlying metal substrate from corrosion. In general, a coating contains micro-pores, areas of low cross-link density or high pigment volume concentration that provide paths for diffusion of corrosive agents such as water, oxygen, and chloride ions to the coating/metal interface. Therefore, it is often necessary to incorporate inorganic or organic inhibitors into paint systems [1, 2]. Hexavalent chromium (Cr^{6+}) compounds are the most effective passivating inhibitors, activated under site specific conditions, and have been used for decades. But hexavalent chromium compounds are genotoxic carcinogens, causing irreversible genetic damage or mutations by binding to DNA, primarily through inhalation [3].

On the other hand, there are also requirements for temperature and UV resistance, flexibility, adhesion, water resistance, fluid resistance, and corrosion resistance. Coatings need to be flexible and adhesive (promoted mainly by the primer). To meet these demands, the aircraft industry has traditionally required a large quantity of solvents, enabling a two-component composition to be used and applied by spray application. Historically, a wide variety of solvents have been used, such as methyl-ethyl-ketone (MEK), toluene, xylene, and methyl-iso-butyl-ketone (MIBK) [4]. In addition, high volumes of solvents are involved also in the paint stripping process, prior to repainting, necessary to reduce weight build-up and allow inspection of the structure. Traditional strippers consist mainly of methylene chloride and phenol. Excessive exposure to organic solvents may cause intoxication and increase cancer risk; and aircraft painting workers exposed to the highest concentrations have shown a decline of 19.5 % in the sperm mobility [5].

1.2.2 Environmental regulations

For about two decades, environmental protection organisations have demanded improvements on the applied technologies, imposing strong limits and control. In the U.S., the Clean-Air Act addresses volatile organic compounds (VOCs) that contribute to the formation of ground-level ozone, with a significant impact on solvent users. The Air Resources Board (ARB) developed a reactivity-based aerosol coatings rule, approved by the Environmental Protection Agency (EPA) in 2005, which encourages reductions in the use of higher reactivity VOCs, instead of mass-based regulations. In addition to being regulated as VOCs, some aviation coatings are also regulated as “hazardous air pollutants” (HAPs). EPA has developed regulations in

1995 that apply to "major sources" of HAP emissions. HAPs are air toxic pollutants known to, or suspected of, causing cancer or other serious health effects.

In Europe, the Solvents Directive from the European Commission Environment, which regulates industrial emissions of VOCs, started in 2003. European regulations on Registration, Evaluation and Authorization of chemicals and their safe use, known as the REACH regulations, came into force in 2007. REACH calls for the progressive substitution of the most dangerous chemicals, when suitable alternatives have been identified. Chromates used as corrosion inhibitors for pre-treatment and coating of metals in aerospace are included as a Substances of Very High Concern (SVHC) according to the article 57 of REACH Regulations. SVHC may have serious or often irreversible effects on human health or the environment.

In summary, current regulations demand two main actions for the aerospace industry: elimination or reduction of VOCs, and elimination of chromates. These are regulatory affairs that have evident impact on suppliers and customers of these substances.

Options for complying with regulations are to switch to an alternative technology or reformulate coating composition. The aircraft industry tends to move cautiously, and reformulation is a preferred option. For a possible reformulation of active inhibitors, the most promising candidates are magnesium [6] and cerium [7] compounds; molybdates [8], vanadates [9, 10] and phosphates [11] are also investigated. To reduce solvent usage and improve performance, an option is to reduce resin viscosity, but at the expense of increasing paint cycles (surface drying is slower and remains sticky until chemical curing starts), and reducing pot-life [12].

Other approaches are based on alternative technologies. High-solids systems have been developed, but they increase weight and do not eliminate solvents [13]. In water based paints [14], the amount of water is not limited, providing better application properties and lower VOC levels, but these systems have higher curing temperatures, and require higher energy consumption for drying. The ultimate improvement in VOC levels would be to completely eliminate solvent use with alternative technologies such as powder or radiation cured coatings. Powder coatings are the choice of many other industries such as the automotive. Materials such as polyesters and acrylics are used on car components for both internal and external applications, such as suspension systems, underbody, windscreen wipers, filters housing, seat frames, and aluminum or steel wheel hubs. But for the use in aviation, it is necessary to consider that the powder usually has to be stoved at temperatures detrimental for aerospace aluminum alloys. In addition, non-solvent coating technologies also have restrictions on the shape of substrates [15], and the up-front capital costs required for new equipment can be high.

There are already several chrome free systems developed by Deft, Sherwin-Williams, and AkzoNobel Aerospace Coatings, and the military sector has taken the lead in the qualification of chrome-free primers and pre-treatments [16]. But the elimination of chrome from primers and pre-treatments continues to be the challenge that keeps

researchers developing new products.

Currently, most aircraft coatings are applied by thin-film spray cured at ambient temperature, mainly in exterior painting. Other methods, such as powder coating, are used where sprayed paints can not meet requirements such as resistance to specific fluids or wear [17]. Powder coating materials currently used in aircrafts include PPS, PEEK, and epoxy resins; and are applied, for example, on landing gear and turbine parts, door handles, and struts [17–19].

1.2.3 How LCPs could help the aerospace industry?

The replacement of Cr^{6+}, elimination of VOCs, and compliance with HAP regulating laws are not the only concerns. To reduce waste generation, extend the life of a component, and reduce weight and maintenance costs are also objectives of the aerospace industry. Several barrier coatings have been developed or modified to follow environmental regulations and increase performance; and new appliation methods include plasma-deposition, sol-gel, electro-deposition, and powder coating [1].

Several academic and industrial researchers have recognized the potential of Thermotropic Liquid Crystalline Polymers (TLCPs) for coating applications, due to their outstanding combination of fracture toughness, chemical resistance, and barrier properties over a wide temperature range [20–23]. These properties are mainly obtained due to the formation of an ordered melt, or liquid crystalline phase (mesophase), which produces a self-reinforcing phenomenon. One of the most studied TLCPs is the thermoplastic Vectra® (Ticona GmbH), which exhibits an exceptionally low coefficient of thermal expansion (CTE), high temperature stability and chemical resistance [24].

Thermoplastic TLCPs have two main problems, the complex coating manufacture process required, and their poor adhesion properties [25]. This has restricted the use of TLCPs in coating applications and coextruded films. In addition, they have high melt processing temperatures and a hierarchical fracture behavior, which makes it inherently difficult to grind TLCPs and obtain a powder suitable for powder-coating techniques [26].

Liquid crystalline thermosets (LCTs) are a potential solution. Recently, a new family of phenylethynyl end-capped Vectra-based oligomers was introduced [27]. These LCTs are expected to have increased surface activity due to the end-groups. Therefore, these new LCTs are predicted to have the aforementioned properties inherent of LCPs, with greatly improved adhesion. Another advantage of these LCTs is that due to the lower mechanical properties of the reactive oligomer intermediate, they can be easily milled into fine powders suitable for powder-coating applications. One may then expect these new LCTs to overcome commercial TLCPs drawbacks and be successful protective, environmentally compliant coatings, especially in aggressive environments such as hydraulic fluids or de-icing agents used in aerospace.

1.3 Research questions

As mentioned previously, LCTs have interesting properties for coating applications. However, the behavior of thin coating films may differ from that of bulk polymers. Moreover, factors like substrate influence and coating-substrate interaction and adhesion should be also taken into account. Therefore, previous research on LCTs may not be directly applicable to estimate the suitability of LCTs as coatings.

Many questions need to be answered before LCT coatings can be applied on an aircraft component. In this early stage of their development, the first question that needs to be answered is: Can thermosetting liquid crystalline polymers find applications as coatings in aerospace? This is a broad inquiry that implies answering a wide range of questions from how can the polymer be applied as a coating to the compliance with requirements and regulations from the aerospace or aircraft industry. This work constitutes the first approach to the use of phenylthynyl terminated LCTs for coating applications, and therefore focuses on the following questions:

- Coating manufacturing and properties. What are the effects of material and processing variables on the properties of LCT coatings?
- Coating substrate interactions. What is the influence of the environment and substrate preparation on the coating properties?
- What are the obstacles, from the materials science point of view, for the application of LCTs in the aerospace industry?

1.4 Aim of the thesis

The general objective of this work is to contribute to the development of a non-hazardous coating with improved scratch/wear and corrosion resistance, eliminating the use of solvents. This means increased durability under harsh conditions and compliance with environmental regulations.

In particular, the main goal of this thesis is to evaluate the applicability of LCTs as a barrier/protection coating in the aircraft industry, and contribute to the knowledge required for its potential application. In other words, we aim at contributing to the

- knowledge of LCT coatings behavior and properties.
- understanding of the influence of material and processing parameters such as curing time, molecular weight, molecular orientation.
- understanding of the coating interactions with the environment.

1.5 Methodology

Two powder coating techniques have been selected for the manufacture of the coatings, based on the polymer properties and behavior. The first technique, here referred to as melt-pressing, is attractive due to its simplicity and minimal powder requirements. Despite its limitations, melt-pressing allows the application of these systems without a time consuming process development and optimization, and it has been used throughout the thesis. The second one, plasma spray, is introduced in the last section as an alternative technology capable of increasing the versatility and applicability of the LCTs. The plasma spray method also addresses the drawbacks found with the previous technique.

The substrate selected is an aluminum alloy AA5083-H111. This was selected for being a non-heat-treatable alloy, to ensure that the substrate is not strongly affected during the melt-pressing and curing of the coatings. LCT coatings were also applied on polyetherimide (PEI) composites using plasma-spray. PEI, reinforced with either carbon or glass fibers, is a thermoplastic composite undergoing extensive research for aerospace applications, and was selected due to the high glass transition temperature of the PEI matrix.

Throughout the thesis, two main techniques were used for the mechanical characterization of the coatings: nanoindentation and microscratch. The basic concepts of indentation and scratch testing are among the first experimental methods developed for materials characterization. But it is thanks to the latest technological developments, that these techniques started to be used for the scientific study of thin polymer films and coatings in a micro- and nanoscale. These methods provide quantitative information unattainable with other techniques, and are still maturing. This work, while benefiting from their use, contributes to their development and understanding.

1.6 Outline

This thesis is divided into nine Chapters. Chapter one reviews the current situation of coatings in aerospace and introduces these novel polymers and the motivation for this work. The second Chapter briefly reviews the development of LCPs and LCTs to understand their relevance for coatings science, in particular for applications within the aerospace industry. Subsequently, in Chapter three, we describe the polymer synthesis, the coating preparation, and the experimental techniques used in this work.

In Chapters four to seven, the coating properties are investigated. Chapter four focuses on the evolution of mechanical, physical, and morphological properties during the crosslinking of the LCT. In Chapter five, the effects of molecular weight of the reactive oligomer, and, consequently, end-group concentration are investigated.

Chapter six presents an investigation on the influence of temperature and molecular orientation; and in Chapter seven, the adhesion and durability of the coatings are examined. In this Chapter, the effects of substrate pretreatments and different environments on the LCTs are analyzed in and compared to the performance of the thermoplastic.

Chapter eight introduces an alternative coating technique that will provide more versatility and flexibility for the use of LCTs as coatings. The successful development of this technique would allow the use of more temperature sensitive substrates, more complicated shapes, and automated processes. Finally, the last Chapter analyses the main findings, leading to the final conclusions and possible answers to the main question that motivated this study.

2 Background Information

2.1 Overview

Thermotropic Liquid Crystalline Polymers (TLCPs), a particular type of LCPs, are in the market since the 1970s. TLCPs are characterized by a highly ordered mesomorphic phase between the crystalline solid and the isotropic liquid. Extensive research led to the development of numerous new, wholly aromatic TLCP systems with high tensile strength, stiffness, and impact resistance along the direction of extrusion or flow during processing. The achievement of these properties is attributed to the retention, upon cooling, of the orientation of the rigid rod-like molecular chains in the nematic mesophase, a phenomenon known as self-reinforcement. The aromatic structure of these polymers also ensures high melting points and thermal stabilities. This has traditionally led to the use of these polymers in injection moldable structures requiring high modulus, strength, and thermal stability. This work explores the use of recently developed thermosetting TLCPs for coating applications.

2.2 Aerospace coatings

The term "Aerospace Coating" comprises a wide spectrum of organic and inorganic materials from paints and polymers to metals and ceramic nanoparticles. The performance requirements of coatings for aerospace applications are considerably demanding. For instance, subsonic aircrafts are designed to perform within a temperature range from to -55 to 80 ^{o}C [28]. Coatings can be exposed to chemicals such as runway and air-frame de-icing fluids. Moreover, ozone-depleting substances, such as methyl chloroform, are still used in some aircraft maintenance processes [29]. Other parts such as heat exchangers, gearbox housings, jet engine air intakes, undercarriage components, shafts, thrust nozzles, and turbine blades are subjected to even more extreme operating conditions. Therefore, protective coatings must be able to resist extreme temperatures as well as chemical attack and service wear and abrasion, while fulfilling basic aircraft requirements, such as minimum weight and reliability. All in all, no single coating can meet the demands of every part and section of an aircraft, and a variety of multilayer systems were developed to efficiently satisfy different demands. The sprayed paint used to protect the fuselage, can not protect the

blades of a turbine; and the inorganic powder thermal sprayed on the blades would add too much weight if sprayed on the fuselage.

Liquid crystalline polymers (LCPs) such as Kevlar® and Vectra® have been used in a number of high performance applications including the airbag fabrics for the recent NASA Mars lander missions (the Spirit and Opportunity robots), as well as Mars Pathfinder that deployed the Sojourner rover [30]. In the previous chapter, we have seen that the superior properties of TLCPs such as Vectra® are also of high interest for surface protection. Low coefficients of thermal expansion (CTE), for instance, lower internal stresses [31]. Excellent barrier to gases and moisture, i. e. low permeability, is another favorable element to their use in coating applications [32–35]. They are also known as self-reinforcing materials [36], due to their particular molecular behavior, which provides improved mechanical properties. TLCPs posses as well an excellent solvent resistance, retention of properties at high and cryogenic temperatures, and flame-retardant properties [24]. In addition, TLCPs have very low melt viscosity, which facilitates their processing via injection molding and extrusion. Its rapid crystallization allows extremely fast molding cycles, and the lack of densification upon solidification facilitates high precision molding [37]. But what is a thermotropic liquid-crystalline polymer and how can they achieve such a combination of properties?

2.3 Liquid crystallinity and liquid crystalline polymers

2.3.1 Liquid crystallinity

Liquid crystalline polymers (LCPs) are capable of forming regions of highly ordered structure while in the liquid phase. This liquid crystalline phase, also known as mesophase, has a degree of order intermediate between a crystalline solid and an isotropic liquid.

There are different kinds of mesophases, characterized by a different arrangement of the constituent molecules. In LCPs, the most common one is the nematic [38], in which the molecules tend to arrange parallel to a common direction defined by the director n (Fig. 2.1 a) and show long-range order but lack positional order. The smectic phase (Fig. 2.1 b), characterized by a bidimensional order, where the molecules lie parallel and form molecular layers, is also present in many LCPs.

The transition to a mesophase can be observed by temperature changes, in the case of thermotropic liquid crystals. On the other hand, in lyotropic LCPs the mesophase appears upon dissolution, as the effect of specific interactions between a solute and a solvent. This phase behavior can be reversible (enantiotropic) or can show up only upon heating or cooling (monotropic).

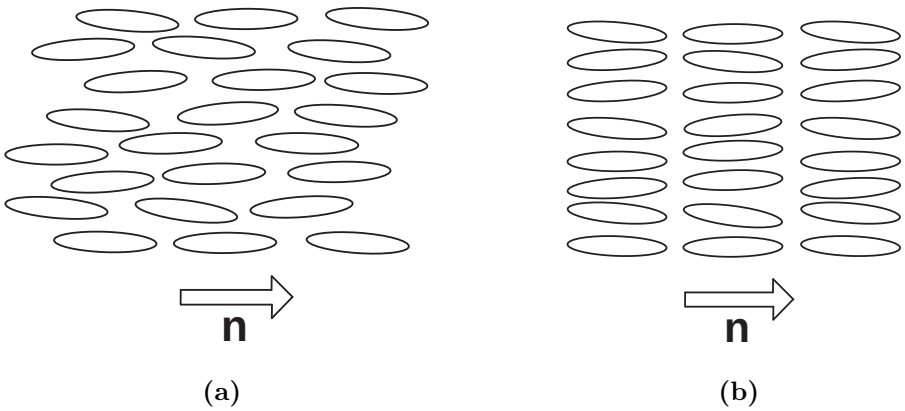

Figure 2.1 – Schematic representation of the nematic (a) and smectic (b) phases

2.3.2 Molecular structure of LCPs

Conventional thermoplastic polymers consist of long backbones that form a random coil configuration (Fig. 2.2 a). In semi-crystalline thermoplastic polymers, crystalline sections are surrounded by amorphous regions (Fig. 2.2 b), and a stiffer product results from the crystallinity, which permits use above the glass-transition temperature (T_g). Higher module and higher tensile strengths occur when polymer molecules are extended and aligned with the load direction. Under the shear fields of extrusion, injection molding, or fiber spinning, these long molecules tend to align. But the chains remain partially coiled; and, on the removal of stress, the molecules partially lose their orientation and tend to recoil [39]. In the case of LCPs, the molecular alignment in a mesophase occurs spontaneously, and the macroscopic orientation of mesophases is thermodynamically stable.

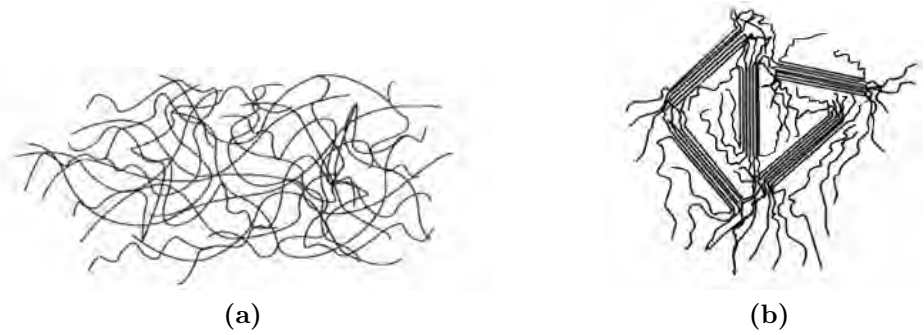

Figure 2.2 – Schematic representation of amorphous (a) and semi-crystalline (b) isotropic polymers

Tsykalo [40] explains that the two most important theoretical models of LCPs were developed by Onsager and Flory. He summarized these two models and concluded that liquid crystalline aromatic polyamides and aromatic polyesters allow the

achievement of a practical modulus approaching that of the theoretical maximum due to the fulfillment of three important requisites for high modulus thermoplastics [41]:

1. The individual molecules must be stiff
2. Their alignment must be nearly perfect
3. The ratio of the aromatic to aliphatic linkages must be high.

Collyer [42] explains that in the case of LCPs, it is the chemistry that provides a higher extended chain conformation rather than the improvement in the design of processing equipment. The rigid portions responsible for the mesophase can be either connected head-to-tail, forming the polymer backbone in main-chain LCPs (Fig. 2.3 a), or linked to the polymer main chain in side-chain LCPs (Fig. 2.3 b).

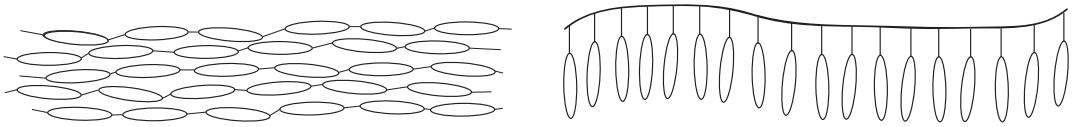

Figure 2.3 – Schematic representation of main-chain (a) and side-chain (b) LCPs

In LCPs, the molecules may be arranged in domains (Fig. 2.4), similar to the magnetic domains of a ferromagnetic material. Within these domains, the molecules are aligned; and the average direction of the molecules in each domain is the director n (Fig. 2.1). There is generally no relationship between the directors in adjacent domains; however, like in a ferromagnetic material, all the directors may be aligned. In the case of LCPs, the domains can be aligned by shear forces during processing.

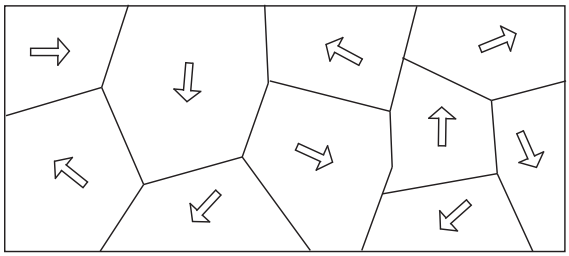

Figure 2.4 – Schematic representation of ramdomly oriented domains in an LCP

Collyer [42] compared the polymer molecules in LCPs to cut logs in log jams on a river. If the groups of logs are oriented in the direction of the stream they readily flow away. This orientation also aligns all the logs in all the groups giving an extended alignment, which is the required conformation to give high modulus in LCPs. This analogy indicates that the good mechanical properties of LCPs should be accompanied by low melt viscosity and hence an unusual ease of processing. This is, in fact, the case.

The willingness of the molecules of LCPs to remain aligned gives the polymer surfaces the characteristic "fingerprint" appearance [43, 44] of liquid crystals (Fig. 2.5), and fracture surfaces examined with SEM reveal fibrous chains in the bulk material (Fig. 2.6). Additionally, the mechanical properties of LCPs are similar to those of fiber reinforced thermoplastics. For these reasons, LCPs are often referred to as self-reinforcing polymers [36, 42].

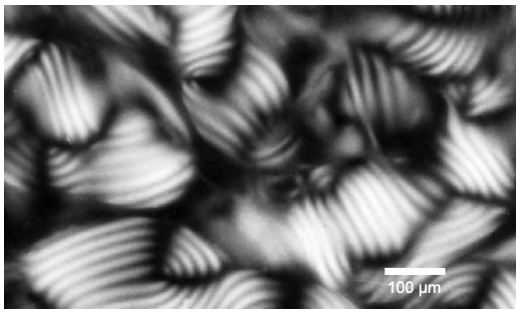

Figure 2.5 – Collagen fingerprint pattern typical of a liquid crystalline phase [43]

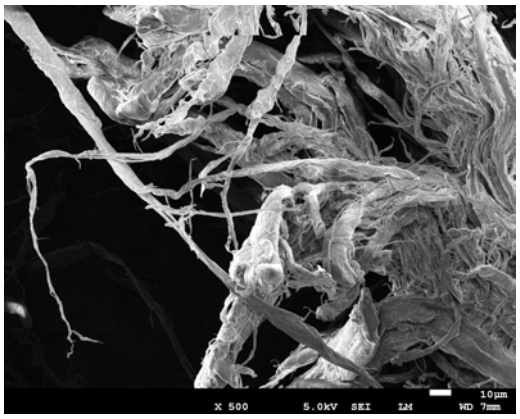

Figure 2.6 – Scanning electron micrograph of a Vectra® A950 pellet after milling

2.3.3 Microstructure of LCPs

The microscale domain structures of LCPs can be visualized using polarized optical microscopy (POM) [45, 46]. From the basic theory of optics, it is known that light is blocked by two polarizers at 90° with respect to each other [47]. When a thin LCP film is placed between the polarizers, the characteristic birefringence of the liquid-crystalline sample rotates the plane of polarization. As a consequence, light is now partially transmitted by the second polarizer, and the domain structure of the LCP is revealed. As an example, Fig. 2.7 shows the liquid crystalline domains of a Vectra® A950 film. The texture of the LCTs is equivalent to that presented in Fig. 2.7.

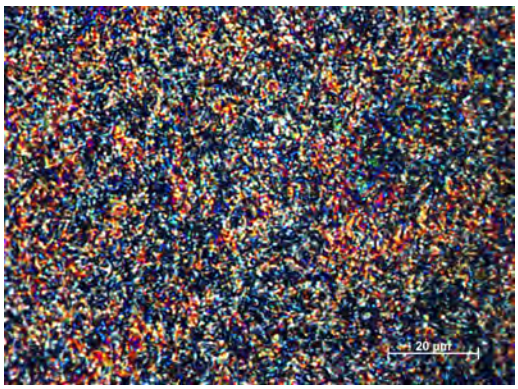

Figure 2.7 – Nematic texture of Vectra® A950 film observed placing the sample between crossed polarizers

Hobdell [48] and Goldbeck-Wood [49] investigated the microstructure of a Vectra-type LCP with a molecular weight of 5000 $\frac{g}{mol}$ using SEM. TEM and wide-angle X-Ray diffraction were also used to investigate microstructure [37]. The commercial thermoplastic TLCP Vectra®, forms a nematic phase, the most simple liquid crystalline phase, where there is long range orientational order with only short-range positional order. However, the range of microstructures observed microscopically is still considerable, with banded lamellas and very fine 'tight' textures (Fig. 2.8). Viewed on the molecular scale, thermotropic molecules are quite complex, often consisting of aromatic groups connected via ester links, for example. They are frequently random copolymers with different mesogens (the fundamental units of a liquid crystal) being connected along the chain at random in order to reduce the crystal melting point. However, once a molecule is sufficiently stiff and straight to form a liquid-crystalline phase, the influence of the chemical structure on the texture at the microstructural level is limited.

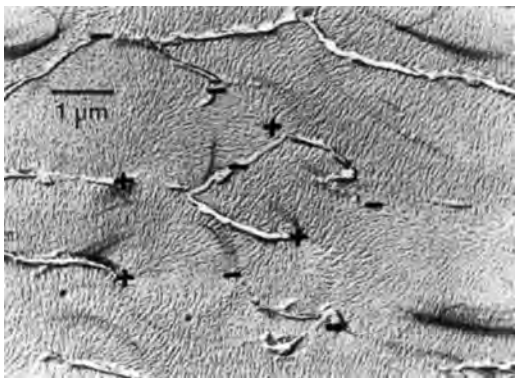

Figure 2.8 – Transmission electron micrograph of an etched LCP film. Both lamellae and fibrils are revealed [37].

In 1993, Hudson explained that solid films, due to the fast crystallization of LCPs, are expected to have a degree of crystallinity of approximately 30 to 40 % [37]. But

this crystallization occurs within seconds, in a first crystallization step, and the rapid transformation process is replaced by a slow process that occurs on annealing. This second crystallization step is a very slow post-crystallization [50], and yields degrees of crystallinity that may exceed 60 %. The annealing causes an improvement of the ordered structure in terms of the degree of crystallization, and not the development of a different phase. These processes occur over more than 10^7 s of annealing time. Annealing at 210 ^{0}C for two hours has little or no effect on the structure [37], the crystals become slightly more perfect but the degree of crystallinity remains the same.

Butzbach proposed a crystallization mechanism for Vectra-type LCPs that would explain this two step process of structure formation. He explains [50] that the crystallization process becomes severely restricted in the course of crystallization since different parts of a chain become attached to growing crystalline regions (Fig. 2.9). The local orientational and positional orders in the remaining nematic regions are then fixed. Any further progress has to occur via translational and reorientational motions of chains that are attached to other crystals. This implies that the structure formation process gets slower and slower as crystallization continues.

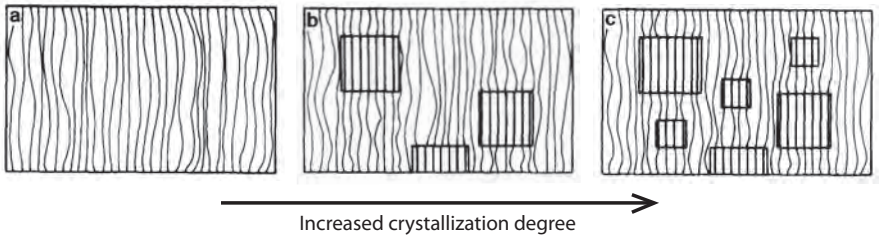

Figure 2.9 – Schematic ilustration of the crystallization mechanism of LCPs [50]

One can expect the shorter polymer chains of liquid crystalline oligomers to be more sensitive to annealing. In fact, Hudson proved that the larger the liquid crystalline polymer chain, the lower the achievable degree of crystallinity [37].

2.4 Development of liquid crystalline polymers

2.4.1 Liquid crystalline polymers

Kevlar is a lyotropic para-aramid developed at DuPont in 1965, typically spun into fibers. The chemical structure of this aramid consists of linearly substituted aromatic rings linked by amide groups. Kevlar production is expensive because of the difficulties arising from using concentrated sulfuric acid, needed to keep the water-insoluble polymer in solution during its synthesis and spinning. In addition, UV radiation degrades and decomposes Kevlar, and it is rarely used outdoors without protection against sunlight.

Economy [51], working on the development of systems that could be processed in the absence of solvents, discovered in the mid 1960s a synthetic route for preparing a p-hydroxybenzoic acid homopolymer (PHBA). This polymer, however, required metal forming processes to be forged. Trying to modify the PHBA by incorporating terephthalic acid (TA) and bisphenol (BP) to produce a melt processable co-polymer, he prepared the first liquid-crystalline copolyester. A family of LCPs based on PHBA/TA/BP was soon commercially available under the trade name of Ekonol (currently Xydar). This was the first thermotropic liquid crystalline polymer (TLCP).

Researchers such as Kuhfuss and Jackson [52] were some of the firsts to report on the thermotropic liquid crystalline behavior in polymers in the 1970s. But the major effort on liquid crystalline polyesters was from 1981 to 1991, motivated by the interest of the industry in LCPs. Since then, TLCPs have been extensively developed; and today, they are sold by manufacturers under a variety of trade names.

Xydar was followed by Vectra® from Celanese, a linear aromatic copolyester. This thermoplastic TLCP consists of 73 % para-hydroxybenzoic acid (p-HBA) and 27 % para-hydroxynapthoic acid (p-HNA). This is a semi-flexible random copolymer with number (M_n) and weight (M_w) average molecular weights of 14.7 and 38.2 kg/mol, respectively [37]. The glass-transition temperature (T_g) of this polymer is approximately 100 ^{o}C and it melts at 280 ^{o}C [24]. The weight-average molecular length is approximately 200 nm, six times the lamellar repeat. The dimensions of the lamellae, which forms rapidly upon cooling from the mesophase, are approximately 10 nm along the chain direction (i. e. about one-sixth of the molecular length) and 100 nm long laterally. The fibrils are indeed seen to be orthogonal to the lamellae [37]; and the lamellae have a regular and uniform period of approximately 34 nm, a length of approximately 100 nm, and the height (estimated from shadow lengths), is approximately 10 nm (Fig. 2.10). Because the molecules are extended in both the liquid crystalline and the crystalline phase, the mechanical properties of the lamellae and the interlamellar regios are similar [37]. They posses very low CTE (4.0 µm/m-^{o}C in the parallel and 38.0 µm/m-^{o}C in the normal directions). Furthermore, the changes on crystallization of these materials are small, unlike in flexible semi-crystalline polymers; and the density difference between crystal and frozen nematic is negligible [49].

TLCPs have found applications in many industries, mainly processed by injection molding [38]. LCPs can be melt-processed on conventional equipment at high speeds with excellent replication of mold details. In fact, the high ease-forming of LCPs is an important competitive advantage against other plastics, as it offsets high raw material cost. Because of their various properties, LCPs are useful for electrical and mechanical parts, food containers, and any other applications requiring chemical inertness and high strength. LCPs are particularly attractive for microwave frequency electronics due to low relative dielectric constants, low dissipation factors, and commercial availability of laminates. Packaging Microelectromechanical Systems (MEMS) is another area where LCPs have recently gained more attention [53].

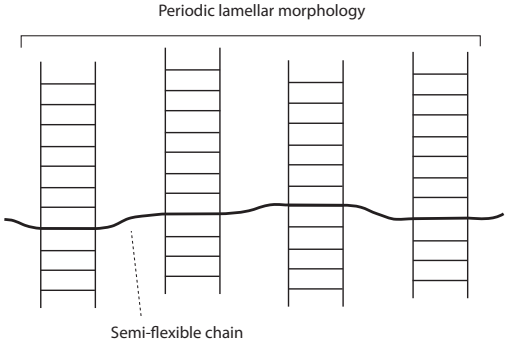

Figure 2.10 – Schematic showing an extended semi-flexible chain incorporated into a periodic lamellar morphology

All-aromatic amorphous polymers posses high T_g, but they are very hard to process into powders for powder-coating applications. A way around is to work with M_n from 5000 to 9000 $\frac{g}{mol}$ (oligomer range), which have lower melt viscosities and improved melt processing [38]. An example of this approach is PETI-5 from NASA, but its unconventional monomers and expensive protic solvents give it a great economic disadvantage.

2.4.2 Development of liquid crystalline thermosets (LCTs)

LCTs are crosslinkable LCPs, a concept first proposed by De Gennes in 1969 [54]. LCTs retain the ordered structure, and form a tridimensional organized network. The first liquid crystalline networks were elastomers synthesized in early 1980s [55]; and densely crosslinked LCTs appeared in the 1990s [56–58]. The works of Barclay [55] and Shiota [59] are reviews on acrylate, epoxy, rigid-rod, and elastomeric liquid crystalline networks.

The two most studied types of LCTs are epoxies and rigid-rods. Epoxy liquid crystalline thermosets (E-LCTs) were developed as a potential replacement for polymers such as epoxies and aryletherketones [38, 60, 61]. They build up the mesophase during the initial curing step, when the epoxy monomers and the curing agent react and give rise to a lightly branched linear pre-polymer. By continuing the cure in the nematic state, crosslinks cause the gelation of the system, fixing the liquid crystal phase [62]. Their physical properties are greatly dependent on the curing reactions. Crosslinking density and distribution, development of the liquid crystalline phase and its retention after curing are strongly dependent on the curing agent and temperature. Induced macroscopic alignment of the domains has to be done during the evolution of the linear pre-polymer, prior to the gelation of the system. The thermal stability is quite broad. Farren [63], for instance, studying the influence of mesogen concentration on the thermal properties of E-LCT based on biphenyl- and biphenol-based diepoxide monomers. He reported loss of 5 % of weight at temperatures ranging from 310 ºC to 360 ºC and CTE from 45×10^{-6} to 82×10^{-6} $\frac{1}{K}$ for an

unaligned E-LCT.

2.4.3 Rigid-rod LCTs

The second type of LCTs are based on liquid crystalline rigid-rods (mesogens) end-capped with reactive groups. These LCTs are a "one part" thermoset, and require no additional curing agent prior to application or curing. In these materials, the reactive end-groups should remain latent during polymerization and processing, with the cure temperature high enough to avoid premature crosslinking during processing, but lower than the nematic-isotropic transition to ensure the retention of the nematic order. In addition, it should not produce any volatiles during curing, which could affect the final properties [38].

In early 1990s, amide-based mesogens with their end-groups were one of the first rigid-rod LCTs to be synthesized, but the melting endotherm and the curing exotherm were very close [64, 65]. In order to lower the onset of melting and improve the processing window, aromatic esters were synthesized using the same amide-based end-groups. These esters have lower melting temperatures compared to amides due to the lack of intermolecular hydrogen bonding. But here, curing took place in the isotropic phase, and gas evolution and void formation were also observed. By the end of that decade, phenylethynyl and aryl-ethynyl end-capped ester-based mesogens were synthesized [66, 67]. These ester-based LCTs retained their liquid crystalline order and exhibited high thermal stabilities. A different approach was developed by researchers at NASA in 2005, who synthesized phenylethynyl end-capped liquid crystal oligomers via a melt-condensation process [38, 68]. During the synthesis, the end-groups are used to control the molecular weight of the reactive oligomer, and these reactive oligomers can be thermally cured in a successive high-temperature step.

These new LCTs were studied as matrix materials for composite structures, and have shown clear advantages over other thermoplastic and thermosetting LCPs, such as improved adhesion and processability [38, 69–71]. Motivated by their adhesion and processing benefits, we will study, along this thesis, some of the factors determining the applicability of phenylethynyl-terminated liquid crystalline oligomers as protection coatings for aerospace.

2.4.4 Phenylethynyl end-capped liquid crystal oligomers

2.4.4.1 The reactive end-groups

The introduction of phenylethynyl-endcapping groups into low molecular-weight oligomers was confirmed to be an effective approach to improve the melt processability of aromatic polyimides [72, 73], and have been used to develop thermosetting resins for aerospace structural applications [66, 74].

The phenylethynyl end-groups permit a wide processing window with a cure onset of 250-360 ºC. Curing of these resins requires heating at 350-400 ºC for 60-90 min and yields a thermally stable, insoluble, and intractable material [75, 76]. Among the different end-capping agents, 4-(phenyl-ethynyl)-phthalic anhydride (PEPA) (Fig. 2.11) is preferred because of its facile synthesis and low toxicity. PEPA-terminated oligomers consistently display excellent thermal and mechanical properities and a narrow cure temperature, affording a large processing window. Roberts [75] explains that the overall properties of the thermoset are determined by the structure and thermal stability of the crosslinks formed; but, as he pointed out, this cured resins are difficult to characterize because of their insoluble/intractable nature. To determine the structure of cured phenylethynyl-terminated oligomers, he used solid-state ^{13}C nuclear magnetic resonance (NMR) difference spectroscopy. Several cured products were identified and assigned to four different classes of cure products: aromatics, products from backbone addition, polyenes, and cyclobutadiene cyclodimers (Fig. 2.12). True crosslinks, chain extensions, and branchlike structures were observed. The relative proportions of the various cure products, and hence mechanical properites, were determined by the molecular weight of the oligomer, final cure temperature, and the structure of the backbone. Lower molecular weight oligomers tend to result in improved crosslinking with branching and chain extension to a lesser extent.

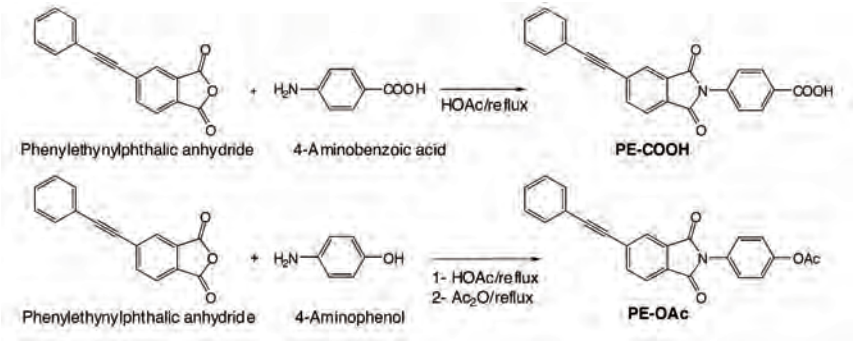

Figure 2.11 – Synthesis of phenylethynyl reactive end-groups [27]

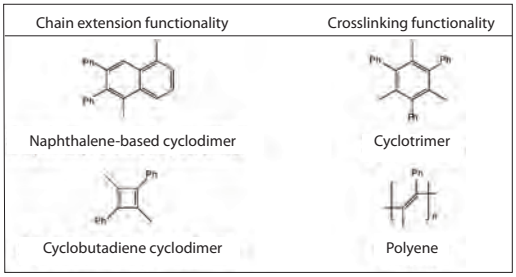

Figure 2.12 – Cured products of phenylethynyl end-group chemistry proposed by Roberts [75]

2.4.4.2 The oligomer backbone

Phenylethynyl end-capped oligomers, based on 4-hydroxybenzoic acid (HBA) and 6-hydroxy-2-naphthoic acid (HNA), were synthesized using standard high-temperature melt-condensation techniques (Fig. 2.13). The synthesis procedure and properties of two series of these polymers were reported by Knijnenberg et. al. in 2006 [27]. In his work, he studied the influence of the HBA/HNA ratio and oligomer molecular weight on the thermal and physical properties of the reactive oligomers and their cured products.

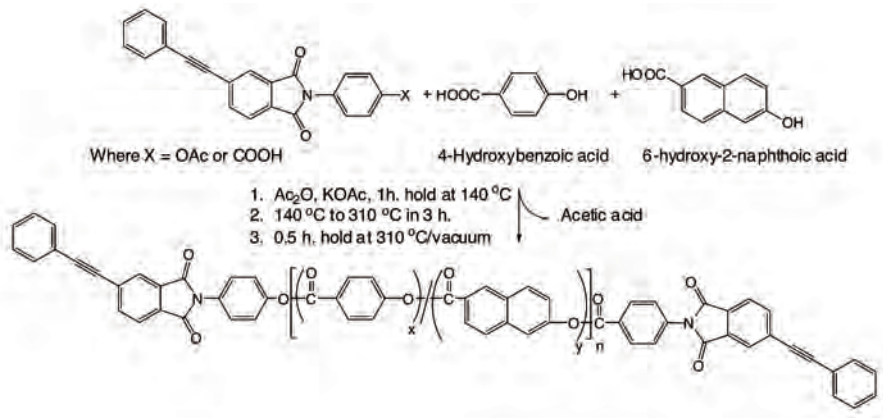

Figure 2.13 – Melt polymerization route towards the synthesis of phenylethynyl terminated LCTs [27]

Knijnenberg et al. also showed that these reactive oligomers have stable melt viscosities during an isotermal hold at 300 ^{o}C for 30 min. This is of mayor importance for the processing of these resins, since it shows that the reactive end groups remain latent during the isothermal hold. These LCTs can be melt-processed within a wide temperature window, in which the reactive end-groups remain latent. Further heating above the cure onset temperature activates the end-groups, producing chain extension and crosslink, fixing the structure. It was seen as well, that the end-group chemistry does not interfere with the formation of the liquid crystalline phase [27, 77]. In addition, Dynamic mechanical thermal analysis (DMTA), indicated that the molecular weight of the precursor oligomer seems to have little to no effect on the storage modulus (E') of the final cured film.

The main backbone composition used in the present work is that of the commercial liquid crystalline thermoplastic Vectra® A950. This polymer is formed by a 73 mol% HBA and 27 mol% of HNA. The LCTs prepared via this route showed improved thermal and mechanical properties over their high molecular weight counterpart. In addition, the synthesis of low molar mass reactive oligomers allowed the preparation of true rigid-rod systems with up to 95 % of HBA or HNA.

2.5 Polymer coatings

Polymer coatings are used in a growing range of applications from wear and chemical resistance to nonstick cookware. Typical examples are Polyethylene (PE), nylons, polyesters, and fluoropolymers. PE and PE copolymers are noted for their flexibility and high strain rates (>500 %); however, they should not be used when service temperatures exceed 75 ºC. Nylons, polyesters, and fluoropolymers have higher temperature resistance than the PE family of resins. Nylon coatings are hard and have excellent wear and abrasion resistance, but are generally prone to absorb significant amounts of water. Fluoropolymers such as ETFE, ECTFE, PVDF and PFA are noted for their low friction coefficients and their excellent resistance to chemicals over a wide temperature range [78]. The properties of these coatings, however, are often limited by poor scratch resistance (which is related to their low modulus and low tensile strength) and high water and gas permeability [79].

Most high performance polymers have low glass-transition temperature (T_g), which limits significantly their final working temperature. In many cases, they also need to be processed at temperatures close to their decomposition temperature (T_d), where side reactions produce brittle products and foaming. Thermoplastics with the highest temperature stability include polyphenylene sulfide (PPS), polyether-ether-ketone (PEEK), and LCPs. PPS coatings are inherently flame resistant, have an excellent solvent, abrasion, and wear resistance, and are used extensively in the chemical processing industry. PEEK is also resistant to most chemicals, melts at 335 ºC, and has low moisture absorption. It has very low smoke and toxic-gas emissions, and is commercially available as powder for powder coating. LCPs display high melt temperatures (>300 ºC); and they have an excellent combination of chemical and heat resistance, dimensional stability, low permehability, and hardness. Commercial materials include Vectra® (Ticona) and Xydar® (Solvay Plastics). Vectra®, for instance, has an excellent thermal stability, inherent flame retardancy, high rigidity and strength (typical modulus, from 10 GPa to 24 GPa; tensile strength, from 125 MPa to 255 MPa), moisture absorption less than 0.03 %, and inertness to acids, bleaches, chlorinated organic solvents, alcohol, and fuels [78]. Currently, LCPs are not commercialized as powders, mainly due to the difficulty to grind these polymers.

2.5.1 LCP coatings

Several authors have recognized the potential of commercial and research grade LCPs for coating applications [20–22, 80–83]. Coatings were prepared by different techniques such as hot-press [84], solvent casting [23], wire wound bars [83], spin-coating [82, 85], and casting [20, 22]. Yoshida et. al. [83], for instance, studied the potential applicability of LCPs as coatings for pre-painted steel sheets, i. e., steel sheets coated prior to forming process. This application requires films flexible and hard enough to resist the manufacturing process and provide the necessary scratch

resistance to the finished product. Another interesting example is the application of spin-coated LCP films with potential ferroelectric properties for application in electro-optics [85].

A few researchers reported also the benefits of unaligned LCT coatings. The important increase in fracture toughness of E-LCT coatings compared to isotropic epoxy resins was explained by Giamberini [62] as a result of the cracking deviation from a straight line by the anisotropic regions of a macroscopically isotropic unaligned LCT.

The use of linear liquid crystalline polyurethane as primer increases the wet adhesion stability of a polymeric coating on steel [22]. Highly ordered polymers applied as primer or adhesive should be able to hinder the permeation of water to the interface. The effectiveness of the primer layer depends on the polyurethane structure, the thickness of the polyurethane layer, and its drying conditions. The permeation of water through the polyurethane layer correlates with the degree of order of the polyurethane. Hence, the interfacial bonds are not weakened as is often the case when water penetrates to the interface; therefore, ordered structures can provide protection against corrosion. In this respect, LCPs are superior to surfactant- or polyacid-based primers [82].

Poor adhesion properties have restricted the use of TLCPs in coating applications and coextruded films. With their molecular diffusion almost wholly limited to translation along the molecular axis (anisotropic diffusion), and the large amount of interdiffusion necessary to homogeneously join two films, rigid rod-like molecules such as thermoplastic TLCPs, resulted in unsuccessful structural adhesives [84]. Muhlebach [86] have shown that polymers containing ester groups undergo inter-chain transesterification reactions which act to randomize the structure. The thermoplastic copoliester Vectra®A shows stable polymer-polymer adhesion strength up to 150 ºC. However, inter-chain transesterification reactions might improve adhesion only with some specific polymeric substrates [84], and have no influence on the polymer-metal interfase.

The inert surfaces of thermoplastic TLCPs, of main importance for their chemical resistance, provide neither the physical nor chemical bonds required for good adhesion with other surfaces [25]. The inert surface of Vectra® A950, for instance, does not react with compatibilizers such as maleic-anhydride grafted polypropylene (PP); though there is a compatibilization effect attributed to hydrogen bonding interactions between the grafted PP and the LCP [87]. Several authors have investigated diverse surface treatments to enhance polymer-substrate adhesion in applications like packaging or printed circuit boards, but with limited results (see for example [88–90]).

Frich [84] studied the corrosion and wear resistance of Vectra® A950 coatings obtained hot pressing its powder onto an Aluminum alloy 2024-T3 substrate. The coatings showed resistance to 100 h in boiling water, 13 h in aqueous solution containing 20 % HCl and these coatings were not attacked by any of the common organic

solvents. He measured an O_2 diffusion coefficient of only 7.3×10^{10} $\frac{cm^2}{sec}$, and an effective barrier to various gases and moisture. He reported wear resistance ten times that of epoxy, and ability to elongate with the substrate up to 40 % with no cracking. Frich explains that an elongation of 40 % is probably due to the ability of the rod-like molecules to align themselves along the elongation direction. On the other hand, Vectra® A datasheets report an elongation at break of only 3.4 %[1] . Moreover, the properties of the aluminum substrate used degrade at temperatures above 120 ºC. Nevertheless, these results indicate the potential applicability of these materials as adhesives and protective coatings for various metals. Adhesion of TLCPs, however, remains a challenge.

It was shown that several authors have investigated diverse treatments to enhance adhesion, but with limited results. In addition, TLCPs have high melt processing temperatures and a hierarchical fracture behavior that makes difficult their grinding for powder coating techniques (Fig. 2.14). In summary, complex manufacturing processes and poor adhesion properties have restricted the use of TLCPs in coating applications and coextruded films.

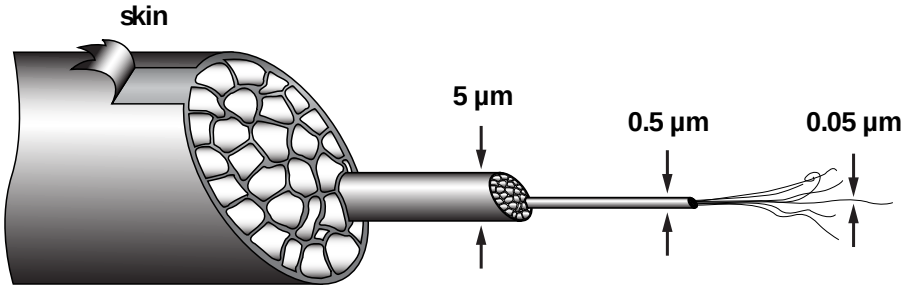

Figure 2.14 – LCP fracture model proposed by Sawyer et. al. [26]

The recently developed LCTs based on Vectra® A backbone oligomers with phenylethynyl reactive end-groups are expected to have increased surface activity due to the end-group polarity. Therefore, these new LCTs are predicted to have the high properties inherent of TLCPs, with greatly improved adhesion properties. Another advantage of these LCTs is that due to the lower mechanical properties of the reactive oligomer, they are easily milled for powder coating, before curing to form the final, crosslinked coat. One may then expect these new LCTs to overcome commercial TLCPs drawbacks and be successful protective coatings, especially in aggressive environments such as hydraulic fluids or de-icing agents used in aerospace applications.

[1]Data available on-line at www.matweb.com and www.campusplastics.com

2.5.2 LCTs as powder coatings

Jannesari investigated the thermal curing of liquid crystalline thermosets with potential as resins for powder coatings [91]. Powder coating processes are gaining great importance in recent years due to their environmental benefits, such as cero volatile organic compound (VOC) emissions. However, despite the attractive properties of these LCTs, their high melting and curing temperatures limit the possible substrate materials. Melt-pressing the powder onto the substrate requires the substrate to be heated to the Tm of the resin. Other powder coating techniques, such as electrostatic spray, may require only a preheating of the substrate at lower temperatures, but the resin still needs to be cured at temperatures detrimental for most substrates used in aerospace.

In the 1990s, researchers successfully applied the first polymer coating using thermal spray (TS) [92]. TS is a powder coating technique not limited by the melt viscosity or thermal conductivity of the substrate material. During TS, particles or wires of the coating material flow through a nozzle, where it is heated and accelerated towards the substrate by a thermal jet. Upon impact on the substrate, the individual molten or softened droplets spread, cool, and solidify to form a continuous coating [93]. Thermosetting resins may be cured during the spraying process, without heating the substrate to the crosslinking temperature of the coating. It is an effective method to produce coatings with a large range of thicknesses on a variety of substrate materials. In addition, coating applications are not restricted by the size of the part being coated and coatings can be readily applied in the field, which is important for industrial applications. Nevertheless, coating performance is strongly influenced by processing parameters and the subsequent coating microstructure that develops. Carefully designed processing conditions are necessary to obtain optimal heat input into the powder and to prevent polymer degradation [93]. Sufficient heat input, optimal substrate preparation, and material changes during deposition must be carefully balanced so that the polymer deforms and adheres well to the substrate; nevertheless, this technique would allow the application of LCTs on a wider variety of composites and aluminum alloys typically used in aerospace.

2.6 Conclusion

In aerospace, there is no single-solution one-layer coating. There is a variety of specific requirements for a wide range of aircraft sections and aerospace structures. These requirements are currently achieved using a variety of multilayer coating systems; however, environmental concerns are driving the development of new materials and processes. The natural tendency is the selection of optimum materials and processes for each particular application, in order to fulfill the specific requirement in an efficient and environmentally friendly way.

In the current work, we aim at investigating the use of newly developed LCTs as

an efficient, environmentally friendly coating for high demanding sections of aircraft and aerospace structures. In particular, we investigate the potential use of phenylethynyl-terminated LCTs in a primer free pre-treatment/coating system for chemical (and wear) protection of aluminum (and composites) in aerospace structures.

3 Materials, Coating Preparation, and Characterization Methods

3.1 Summary

This chapter describes the various materials, processes, and characterization methods used during this research. The first part describes the synthesis of the LCT resins and substrate properties. Next, the main coating process used is presented. And finally, the various characterization methods and tests used throughout this work are described.

3.2 Materials

3.2.1 Coating materials

3.2.1.1 Synthesis of LCTs

Synthesis of phenylethynyl end-groups

A 2 L Erlenmeyer flask equipped with a mechanical stirrer and reflux condenser was charged with 1.1 L glacial acetic acid and 4-phenylethynylphthalic anhydride (0.5 mol, 124.12 g). The mixture was slowly heated to 120 ^{o}C and when all solids were dissolved, the temperature was reduced to 90 ^{o}C and 4-aminobenzoic acid (0.5 mol, 68.57 g) was added. A thick suspension formed almost immediately and was stirred for 2 h at reflux temperature. After the reaction mixture was cooled to 70 ^{o}C, the precipitated crystals were collected by filtration and washed with acetic acid (2x) and ethanol (2x). The off-white N-(4-carboxyphenyl)-4-phenylethynyl-phthalimide (PE-COOH) was dried under vacuum at 150 ^{o}C for 48 h.

N-(4-hydroxyphenyl)-4-phenylethynyl-phthalimide (PE-OH) was prepared in a similar fashion. A 2 L Erlenmeyer flask equipped with a mechanical stirrer and reflux condenser was charged with 1.1 L glacial acetic acid and 4-phenylethynylphthalic anhydride (0.5 mol, 124.12 g). The mixture was slowly heated to 120 ^{o}C and when all solids were dissolved, 4-aminophenol (0.5 mol; 54.56 g) was added. The thick suspension formed almost immediately and was stirred for 2 h at reflux temperature. After cooling to 70 ^{o}C, the precipitated crystals were collected by filtration

and washed twice with acetic acid and twice with ethanol. Subsequently, the phenol end group was acetylated by refluxing PE-OH in anhydrous acetic anhydride at 200 °C for 2 h. N-(4-Acetoxyphenyl)-4-phenylethynyl-phthalimide (PE-OAc) precipitated during cooling as bright yellow crystals. The title compound was again collected by filtration, and washed with acetic acid (2x) and ethanol (2x), and dried under vacuum at 150 °C for 48 h.

The molecular structure of the carboxylic and the phenolic phenylethynyl end-group is presented in Fig. 2.11. The thermal behavior of the phenylethynyl end-groups was analyzed using differential scanning calorimetry (DSC) at 10 $\frac{^{\circ}C}{min}$. The DSC traces are shown in Fig. 3.1. The compounds show sharp melting endotherms at 236 °C and 346 °C respectively, and an exothermic reaction between 350 and 400 °C, indicating the crosslinking of the reactive functionalities.

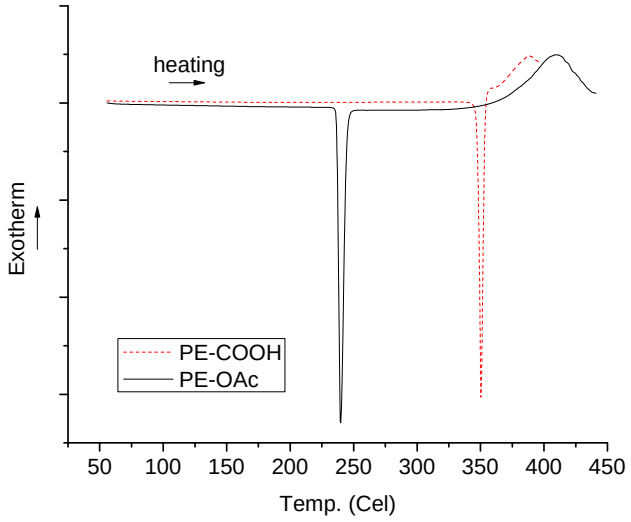

Figure 3.1 – DSC traces of the PE-COOH and PE-OAc reactive end groups, first heat, recorded at 10 °C/min

Synthesis of the phenylethynyl end-capped oligomers

A targeted molecular weight (M_n) is prepared by controlling the concentration of reactive end groups using the Carothers equation [94]; an increasing end-group content will limit the maximum achievable M_n of the oligomers. Tab. 3.1 lists the reagents used for the synthesis of the oligomer.

The liquid crystalline oligomer with a fixed backbone structure consisting of 73 mol% 4-hydroxybenzoic acid (HBA) and 27 mol% 6-hydroxy-2-naphthoic acid (HNA) was synthesized using standard melt condensation techniques (Fig. 2.13). For the synthesis of the 5000 g/mol reactive oligomer, a 2000 mL three-neck round-bottom flask equipped with a sealed glass paddle stirrer was flushed with nitrogen, and

Table 3.1 – Reagents used for the synthesis of the 5000 $\frac{g}{mol}$ oligomer series , as calculated with the Carothers equation

Target M_n	HBA	HNA	PE-OAc	PE-COOH	Ac_2O
5000 g/mol	251.85 g	126.90 g	26.67 g	25.69 g	0.259 L
	1.825 mol	0.675 mol	0.07 mol	0.07 mol	2.75 mol

charged with 4-hydroxybenzoic acid (HBA), 6-hydroxy-2-naphthoic acid (HNA), N-(4-acetoxyphenyl)-4-phenylethynyl-phthalimide (PE-OAc), N-(4-carboxyphenyl)-4-phenylethynyl-phthal-imide (PE-COOH), and potassium acetate. After adding acetic anhydride, the reaction mixture was slowly stirred under a nitrogen atmosphere and heated to 140 ºC to allow acetylation to take place. After a 1 h isothermal hold, the temperature of the reaction mixture was slowly increased to 330 ºC using a heating rate of 1 ºC/min. During this process acetic acid was collected as the condensation byproduct. During the final stages of the polymerization the nitrogen flow was cut off and vacuum was applied in order to remove the last traces of acetic acid. The reaction flask was allowed to cool overnight, and the final product was removed from the flask and processed into a powder. To ensure that all acetic acid was removed we dried the powder under vacuum at 250 ºC for 24 h; the heat treatment also removes any possible low molecular weight components present in the oligomers. Polarized optical microscopy equipped with a hot stage was used to confirm the nematic nature of the products.

3.2.1.2 Other coatings materials

Additionally, reactive oligomers with targeted M_n of 1000, 9000, and 13000 $\frac{g}{mol}$ were previously synthesized in our facilities at the Delft University of Technology by Knijnenberg et. al. [27], and kindly provided for the present research. A reference sample with no end-groups and a M_n of approximately 30000 $\frac{g}{mol}$ was also synthesized and used in this work. The molecular structure of this reference sample is equivalent to the commercial LCP Vectra® A950. Along the present study, the samples were labeled YKXX, where YK indicates the M_n of the reactive oligomer (e.g.: 5K = 5000 $\frac{g}{mol}$), and XX is the curing time in minutes. The commercial thermoplastic counterpart LCP Vectra® A950 was obtained from Ticona GmbH (Kelsterbach, Germany).

3.2.2 Substrate materials

For this work, the substrate selected was a 2 mm thick aluminum AA5083-H111 (Salomon's Metalen B.V., Groningen, the Netherlands) plate, a non-heat treatable aluminum-magnesium alloy. This particular alloy was selected for being non-heat-treatable, to ensure that the substrate is not strongly affected during the melt-pressing and curing of the coatings. Its corrosion performance in most environments

is superior to other aluminum alloys (with the exception of the 1000 series); and is mainly used in marine applications [95]. It is also very common in applications with working compression [96], such as pressure vessels, tanks, fittings, and van bodies. The AA5083 alloy is, however, subjected to both pitting and crevice corrosion [97].

Since this aluminum alloys is non-heat treatable, and therefore low strength, it is not typically considered a material for use on commercial airplanes [98]. However, the aluminum 5000 alloy series is used in aircraft non-structural applications [99], primarily in hydraulic systems , and oxygen, fuel, and oil lines of commercial aircraft [99, 100]. For example, the AA5052 alloy is used in aircraft components and tubes [100], and the 5059 is also used in experimental rocket cryogenic tanks.

AA5083 and AA5086 extrusions and roll forms are used by many aircraft manufacturers such as Boeing, Lockheed Martin, Gulfstream, Embraer, and Bell [101]. The AA5083 series in particular, is suitable for cryogenic applications down to $-165\,^{o}$C, since it does not show the ductile-brittle transition phenomenon. Super-plastically formed (SPF) AA5083 aluminum components have replaced aluminum castings, fiberglass assemblies, and components fabricated by SPF from other aluminum alloys [98]. SPF applications of AA5083 at Boeing include: aluminum hardware [98], the 737 (Fig. 3.2) and 777 (Fig. 3.3) wing tip light housing [102], the 767 moisture shroud that protects the electronics under the cockpit (Fig. 3.4), and the 737 outboard leading edge strakelet (Fig. 3.5) [98, 103].

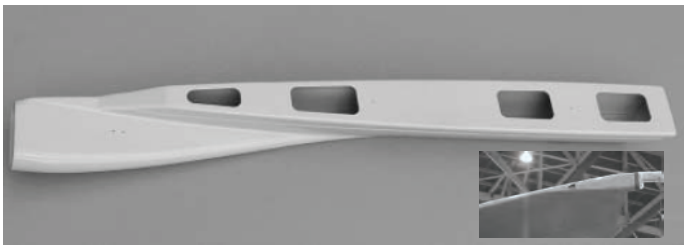

Figure 3.2 – Outboard light housing, installed on the wing of the Boeing 737 aircraft [102]. The inset shows the completed SPF 737 outboard light housing made of AA5083.

Figure 3.3 – SPF AA5083 777 wing tip light housing [98]

Figure 3.4 – 767 superplastically formed moisture shroud assembly comprised of two SPF AA5083 components [98]

Figure 3.5 – SPF AA5083 strakelet on the 737 wing leading edge (adapted from [98])

Effect of coating and curing on the microstructure and mechanical properties of the substrate

Uncoated coupons were exposed to the thermal cycles required for the application and curing of the LCT coatings (described below). Metallographic images of polished and etched samples show a slight growth in banded precipitates (Fig. 3.6). To determine how this might affect the mechanical properties of the substrate, tensile tests of the aluminum substrate were performed according to the ASTM E 8M-04 standard. After the melt pressing and curing thermal cycles, a drop in the yield strength from 160 MPa to 140 MPa was observed, and no further changes were identified (Fig. 3.7).

3.2.2.1 Alternative substrate materials

Aircraft aluminum alloys AA2024-T3 and AA7075-T6 were also used for salt-fog spray testing (Chapter 7). Additionally, in Chapter 8, the LCT was also plasma-sprayed (described below) on glass-fiber (GF) and carbon-fiber (CF) reinforced

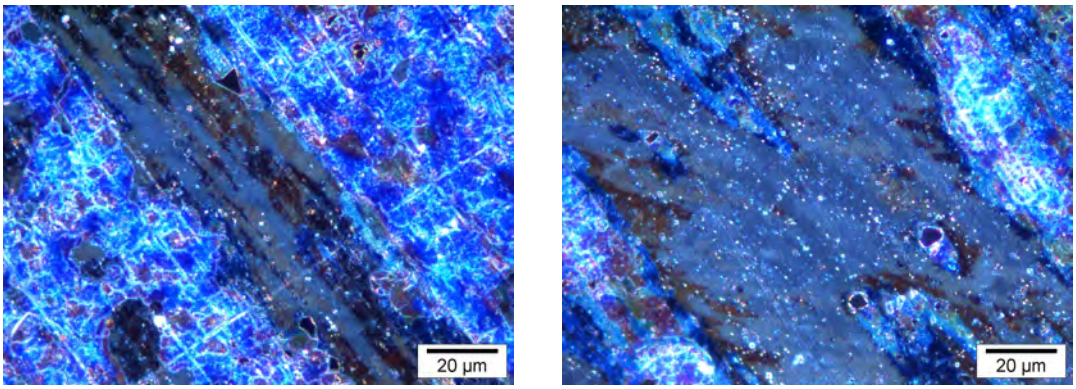

(a) **(b)**

Figure 3.6 – Microstruture of the AA5083 aluminum substrate (a) as received (b) after melt pressing and curing

polyetherimide (Cetex® PEI, TenCate Advanced Composites Inc., CA, USA) composites. The GF and CF reinforced PEI matrix composites consisted in a ten ply $\pm 90^{o}$ lay-up, consolidated in a hot-press during under a temperature and pressure of 320 ^{o}C and 10 bar, respectively. The final thickness of the laminates was 2.35 mm for the GF, and 3.25 mm for the CF reinforced laminates. Polyetherimide (PEI) thermoplastics are undergoing extensive research for aerospace applications, and were selected as matrix due to its high glass transition temperature of 210 ^{o}C.

3.3 Coating preparation

3.3.1 Substrate pretreatments

For the present work, substrates were thoroughly cleaned with an industrial solvent (PFSR, PT Technologies, Watergrasshill, Ireland) and ethanol. Then, the substrates were grit-blasted with 90-150 µm glass beads right before the coating application, to ensure a freshly exposed aluminum surface. All panels were grit-blasted on both sides to reduce deformation due to induced residual stresses. After grit-blasting, the panels were cleaned with an air jet to remove residual metallic particles and glass beads.

During the study of adhesion (Chapter 7), the substrates were pretreated in three additional ways. Firstly, coatings were applied on as-received aluminum. In this case, substrates were clean and degreased with acetone, and no further pretreatment was applied. In the context of this work, we will refer to theses reference samples as non-pretreated (NP). Additionally, two different anodization processes were investigated: chromic acid anodization (CAA) and phosphoric acid anodization (PAA). Prior to the anodization, substrates were prepared according to our standard

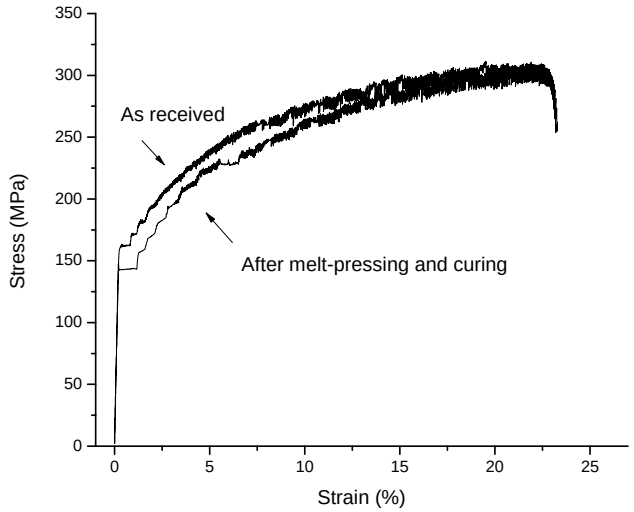

Figure 3.7 – Tensile test results of aluminum AA5081-H111 before and after the thermal cycles corresponding to the melt-pressing at 310 ºC for 5 min and the curing at 370 ºC for 1 h

lab procedure, as follows. First, AA5083-H111 aluminum plates were cleaned with acetone, and submerged in an alkali degreasing solution of P3 RST[1] (4 Kg per 100 L water). Subsequently, substrates were rinsed in distilled water and submerged in a pickling solution of chromic acid (5 Kg per 100 L water) and sulfuric acid (14.3 L per 100 L water). Afterwards, the aluminum plates were rinsed in distilled water and introduced in the respective anodization baths. The chromic and phosphoric anodizations were performed according to standardized protocols from Fokker for AA2024 and AA7075 aluminum series. On these materials, the CAA and PAA processes are expected to yield oxide layers between 2 to 5 µm and 0.2 to 0.5 µm thick, respectively. The thicknesses of the anodization layers obtained on the AA5083 were approximately 3 µm and 0.85 µm for the CAA and PAA treatments, respectively. The morphology of the oxide layers is shown in Fig. 3.8. Lastly, anodized substrates were dried 24 h at 35 ºC.

3.3.2 Coating method

For the purpose of the present research, and based on the polymer properties and behavior, melt-pressing was selected for the manufacture of the coatings. Melt-pressing is attractive due to its simplicity and minimal powder requirements; and it has been used throughout this thesis. The polymers were melt-pressed onto aluminum substrates of 150 x 120 mm using a computer controlled hot-press LAP100 (Gottfried Joos Machinefabrik GmbH & Co. KG, Pfalzgrafenweiler, Germany). Kapton® films, 25 µm and 80 µm thick, were used to control the thickness of the coatings

[1] Alkaline cleaner for metals, Henkel AG&Co. KGaA, Germany.

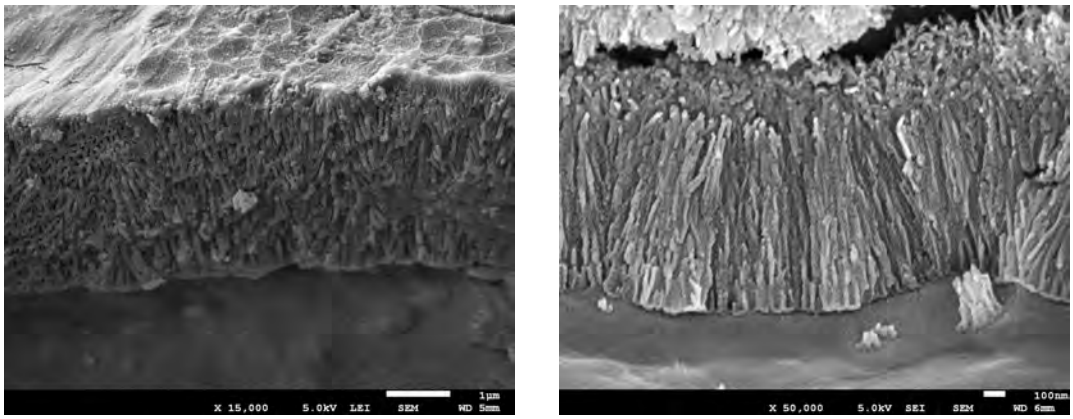

(a) **(b)**

Figure 3.8 – SEM images of brittle fractures of chromic (a) and phosphoric (b) acid anodization layers growth on the aluminum AA5083-H111 substrate. Fractures were performed at N_2(l) temperature.

and as a release film for the mold. The mold was heated to 310 ºC at a rate of approximately 8 $\frac{^{\circ}C}{min}$ without applied force. Once the system reached the indicated temperature, a pressure of 2.5 MPa was applied. The system was held at 310 ºC and 2.5 MPa for 5 min; the temperature was then reduced to 30 ºC at 10 $\frac{^{\circ}C}{min}$. Micrographs of polished cross-sections of coatings on GB substrates showed that for all the end-capped and non-end-capped resins, there is good melt flow and wetting of the surfaces (Fig. 3.9). Melt-pressed oligomer coatings were subsequently cured under vacuum. The curing time and temperature applied ranged from 30 to 75 min, and from 350 to 370 ºC, respectively. The thickness of the coatings was measured at several points by eddy currents using a coating-thickness gauge for non-ferromagnetic metals (Positector 6000, Checkline Europe B.V., Enschede, the Netherlands), and average values were calculated. The final thickness of the coatings was found to be highly dependent on the Mw of the oligomer, and ranged from 30 to 120 µm.

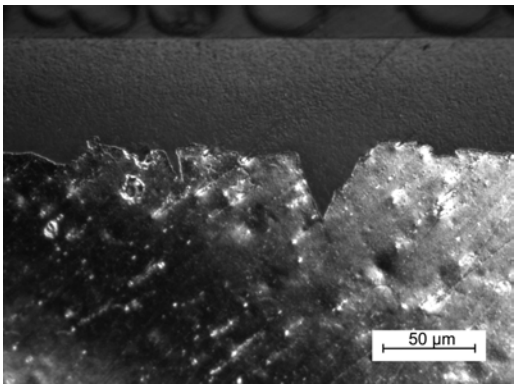

Figure 3.9 – Cross-section of a melt-pressed reactive LCT coating on grit-blasted AA5083-H111 aluminum

For the study of uniaxially aligned coatings (Chapter 6), oriented LCT samples where prepared by adapting the melt-pressing technique. A 9000 $\frac{g}{mol}$ reactive oligomer was forced to flow along a narrow mold during melt-pressing. The coating was then cooled to room temperature, and subsequently cured 60 min at 370 ºC, to finally obtain an approximately 35 µm thick coating. The 9000 $\frac{g}{mol}$ was preferred to the 5000 $\frac{g}{mol}$ oligomer, since its lower mobility would reduce the loss of macroscopic order during curing.

In Chapter 8, plasma-spraying is introduced as an alternative technology capable of addressing the industrial limitations of melt-pressing, increasing the versatility and applicability of the LCTs. Deposition was performed using an atmospheric plasma-spray (APS) system F4MB-XL by Sulzer Metco Europe GmbH (Kelsterbach, Germany), in collaboration with the Surface Engineering Institute at the Faculty of Mechanical Engineering, RWTH Aachen University, Germany.

3.4 Characterization methods

3.4.1 Thermal properties

Thermal analyses were performed using a differential scanning calorimeter (DSC, Sapphire) and a thermo balance (TG/DTA, Pyris Diamond), both from PerkinElmer, Inc. (Massachusetts, USA). For these analyses, sample material was collected by gently removing polymer from melt-pressed coatings.

3.4.2 Micrographic imaging

Bright-field optical microscopy (OM) was performed using a reflection optical microscope (Axiovert 40MAT, Carl Zeiss microimaging GmbH, Gottingen, Germany). Polarized optical microscopy (POM) at various temperatures was performed using a transmission optical microscope (DM/LP, Leica Microsystems GmbH, Wetzlar, Germany), coupled to a hot-stage (TMS 94, Linkam Scientific Instruments Ltd., Surrey, UK) placed between two 360º rotating polarizers. Coating cross-sections were polished to a 1 µm finish. No etching was required.

Lower secondary electron imaging was performed in a field-emission scanning electron microscope (SEM) JSM-7500F (Jeol Ltd., Tokyo, Japan), with a Gallium source accelerated at 5 KV. For SEM analysis, samples were prepared by sputtering an ultrathin gold layer to avoid electrostatic charging on the surfaces. A confocal laser scanning microscope (CM) LEXT OLS 3100 (Olympus GmbH, Hamburg, Germany) was also used for surface morphology and failure analysis and roughness measurements.

3.4.3 Mechanical properties

3.4.3.1 Nanoindentation

Depth-sensing nanoindentation was used to measure the, so called, reduced elastic modulus (E) and nano-hardness (H) of surface and subsurface layers of the coatings. A nanoindentation test consists in the movement of an indenter into the surface of the material and the continuous measurement of force and displacement during the loading and the unloading cycles. Loads as small as 1 nN and displacements of about 0.1 nm can be accurately measured [104]. The Berkovich indenter (Fig. 3.10), with a typical tip radius of about 50 nm, has become the standard tip for nanomechanical testing of thin films and shallow indentations.

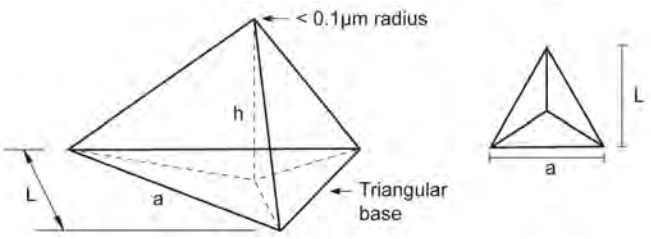

Figure 3.10 – Berkovich tip used for the nanoindentation of thin films and coatings [105]

A typical load-controlled nanoindentation is presented in Figure 3.11a. The initial hold step is included to incorporate the corrections due to thermal drift. Since significant creep-like behavior and time-rate dependent results are expected during the nanoindentation of visco-elasto-plastic materials, such as LCPs, a traditional load function includes also a holding at the peak load and when 90 % of the load is released [106]. The resulting indentation curve of an elastic-plastic sample is presented in Figure 3.11b.

The so called contact stiffness (S= $\frac{1}{compliance}$) can be inferred from the initial slope of the unloading curve, and the reduced Young's modulus (E_r) can be calculated using Oliver and Pharr's method [107]. The E of the coating can then be calculated knowing the Poisson's ratio of the material. Nanoindentation measured H is defined as the maximum load, P_{max}, divided by the indentation area. To gain real-time nanohardness values from a load-displacement graph, an area function obtained from the known tip-shape function is used. This tip-shape function includes a compensation for elastic load during the test; however, it requires adequate knowledge of the visco-elasto-plastic response of the material. Extensive information about the theory and the derivation of the formulas can be found elsewhere [107].

The so-called continuous stiffness measurement (CSM) technique, which uses oscillating signal forces coupled to the load function (Fig. 3.12), allows the continuous measurement of S [104]. This technique has a time constant at least three orders of magnitude smaller than the conventional methods; and therefore, it is more suitable

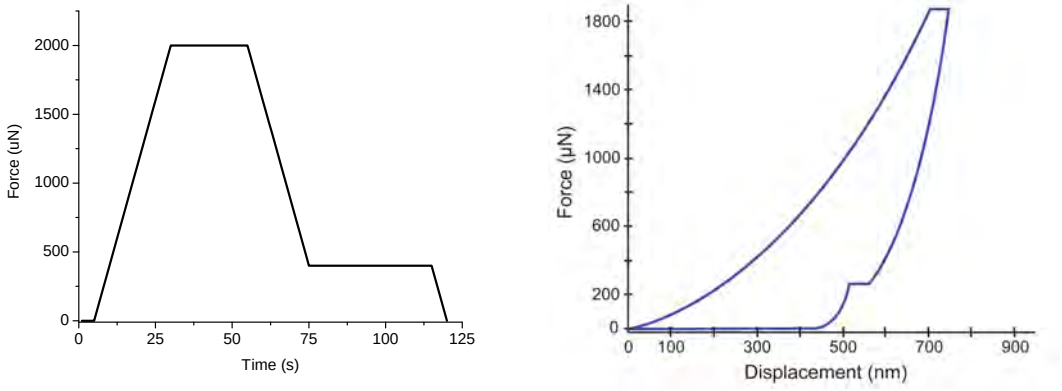

(a) **(b)**

Figure 3.11 – (a) Typical load controlled indentation cycle used for the nanoindentation of polymers; (b) Typical indentation curve showing the load-displacement relation for a polymer subjected to the load cycle showed in Fig. 3.11 a.

for measuring materials with time-dependent properties [105]. In addition, using the CSM method, the E and H can be calculated as a continuous function of time or indentation depth.

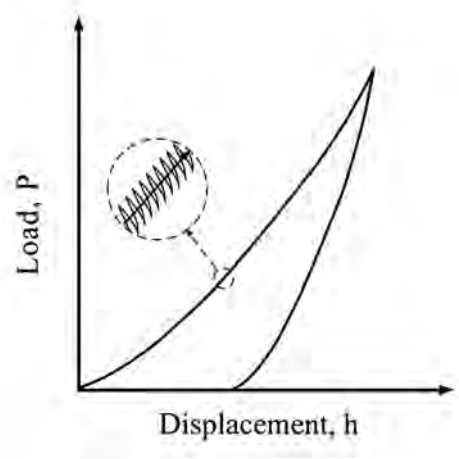

Figure 3.12 – Typical indentation curve using the CSM technique. The inset shows the oscillation signal coupled to the load, which allows the continuous measurement of the contact stiffness [104].

In the present work, nanoindentations were performed with a G200 nanoindenter from Agilent Technologies, equipped with a standard Berkovich tip. Unless otherwise stated, the CSM module was used, since significant creep-like behavior and time/rate-dependent results are expected [106]. The equipment was used in penetration controlled mode, and set to a maximum penetration of 2 µm to avoid influence from the substrate [108]. A frequency of 45 Hz was used for the CSM. The val-

ues of hardness and elastic modulus obtained at penetration depths from 500 to 1800 nm were averaged to determine the hardness and elastic modulus for each test. Typically, 25 indents were obtained for individual specimens, and the average was calculated.

For the in-situ measurement of E and H at various temperatures ranging from -35 to +160 ºC (Chapter 6), a temperature-controlled stage holder was coupled to the nanoindentation system (Fig. 3.13). Due to the temperature-controlled stage, the CSM module could not be coupled. Typically, 10 indents were obtained for individual specimens. Oliver and Pharr's method [107] was used to analyze the unloading section of the nanoindentation load-displacement curves, and average values were calculated.

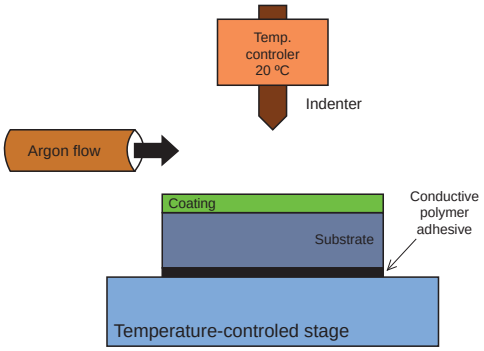

Figure 3.13 – Schematic representation of the nanoindentation system coupled to a temperature-controlled stage holder

3.4.3.2 Microscratch

Scratch tests provide quantitative material deformation data for the analysis of bulk materials, coatings, and thin films; and it has been extensively used for the characterization of polymers [109–114]. A typical microscratch testing set-up is schematically represented in Fig. 3.14.

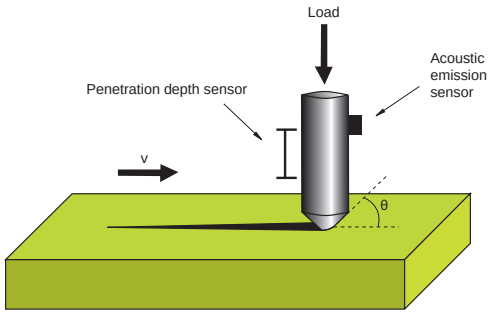

Figure 3.14 – Schematic representation of the microscratch testing of coatings

During the test, the system records a variety of parameters such as normal load, penetration depth, and acoustic emissions. Subsequently, by means of a post-scan, the residual depth can be determined, and properties such as the elastic recovery (ER) calculated. The ER indicates the elastic recovery with respect to the total penetration depth during scratching, and it was calculated using the following equiation: $ER = \frac{(h_{ep}-h_p)}{h_{ep}} \times 100$. Where h_{ep} is the total penetration depth and h_p is the residual depth measure with a post-scan immediately after scratching. This parameter does not incorporate complete visco-elastic recovery, since h_p is measured immediately after performing the scratch.

For this thesis, the micro-scratch tests were performed using a computer controlled microindenter coupled with an optical microscope (CSM Instruments S.A., Switzerland). A standard diamond Rockwell tip with a radius of 100 µm was used. Two different test methods were performed during this study: i) a constant load test consisting of a pre-scan to determine the profile of the surface, and the subsequent scratching at constant loads of 1, 2, 4, and 6 N. Immediately after the scratch, a post scan was performed to measure the residual depth of the groove. And ii) a progressive load test consisting of a pre-scan, and followed by a scratch with a linearly increasing load from 0.04 to 30 N along a scratch lengths from 8 mm. After the progressive test, the post-scan was omitted to maintain surface features intact for fractographic analysis. The first method would provide information about load/depth specific effects such as plastic deformation, while the second would allow the analysis of the overall fracture behavior and coating-substrate interaction, relating loads to specific failures.

The scratch tests were unlubricated, which means that the material in contact with the front part of the indenter experiences both stick and slip boundary conditions as a result of the adhesive component of the scratch force. It is also necessary to indicate here that, at the microscale, the local inhomogeneities and roughness have less impact. On the other hand, the interaction with the substrate becomes more relevant, since the penetration depth is usually higher than 10 % of the thickness of the coating [108].

The failure modes associated with the scratch test were identified by post-facto observation of the scratch track using SEM and CM. The loads indicated on the SEM images were calculated graphically, by measuring the distance from the start of the scratch, and knowing that after an 8 mm scratch, the final load was 30 N.

3.4.4 Adhesion

Lap-shear [115, 116] test samples, with an overlap of 15 x 24 mm (Fig. 3.15a), were prepared by melt-pressing the polymers between two cleaned and grit-blasted aluminum panels. A polymer layer of approximately 150 µm was obtained by first mixing the ground polymer with a 5 % (wt/wt) of 90-150 µm diameter glass beads. The press- and thermal-cycles used to prepare the samples for lap-shear testing

were identical to those previously presented for coatings manufacture. Direct tensile testing was used to measure pull-off strengths. Pull-off test samples were prepared bonding a 25 mm diameter cylindrical steel stud to the coating with a structural two component epoxy-based adhesive (Araldite® 2015, Huntsman, Basel, Switzerland). After bonding, the coating was gently cut around the stud. A symmetric stud bonded to the base of the substrate acted as restraining device (Fig. 3.15b); and the lap-shear and pull-off strengths were calculated dividing the force (F) by the overlap/contact area. The studs were fixed to a self aligning coupling system to avoid non-tensile stresses. The test machine was a tensile Universal 250 KN Zwick GmbH & Co. KG (Ulm, Germany). The cross-head rates were 1.3 and 2.5 $\frac{mm}{min}$ for the lap-shear and the pull-off tests, respectively.

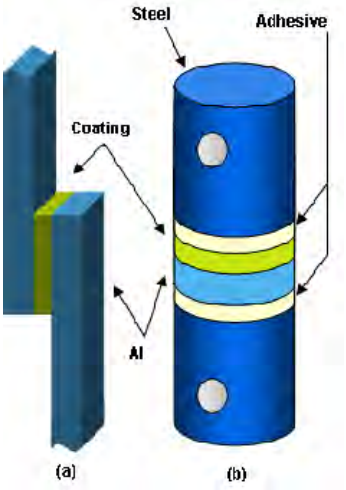

Figure 3.15 – Schematic illustration of the lap-shear (a) and pull-off (b) samples used for adhesive-bond testing of the coating.

3.4.5 Environmental resistance

Salt-fog spray accelerated corrosion tests were performed in a Karl Weiss salt-spray cabinet S-1000 (Liedekerke, Belgium), using a 5 % NaCl solution in H2O at 35 ^{o}C according to the ASTM B117 standard [117]. Cross-cut coated coupons of 50 x 50 mm were exposed to the saline fog for 1000 h. After exposure, samples were visually inspected for blistering, peeling, and gloss change.

The resistance to hot moisture was tested in a climatic cabinet series C40/1000 from CTS GmbH (Hechingen, Germany). Cross-cut coated coupons of 50 x 50 mm were exposed to a temperature of 60 ^{o}C with a 95 % relative humidity during 1000 h; subsequently, samples were visually inspected for coating failure.

The resistance to various aviation fluids (see Tab. 3.2) was investigated by full immersion tests. Cross-cut coated coupons of 50 x 25 mm were exposed for 500 h at

22 ºC. The weight gain of the samples was measured in a precision balance (AB204-S, Mettler-Toledo B.V., Tiel, the Netherlands), with a tolerance of 0.1 mg. Exposed samples were thoroughly cleaned with ethanol and weighed before and after exposure. The edges of the samples were not protected in any of these three testing methods.

Table 3.2 – Selected aviation fluids for full immersion tests

Fluid	**Description**	**Dangerous Components / Constituents**
Skydrol 500 B-4 (Solutia)	Fire Resistant Hydraulic Fluid	Tributyl phosphate (19.8%); 2-ethylhexyl 7-oxabicyclo[4.1.0] heptane-3- carboxylate (<10%)
Turbo Oil 2380 (Air BP)	Synthetic lubricating turbine oil	Tricresyl phosphate (1-5%); n-phenyl-1-naphthylamine (1-5%)
Shell Jet A1	Aviation Turbine Fuel	Kerosine (petroleum) hydrodesulphurised
HI-FLO (Prist)	Anti-Icing Aviation Fuel Additive	Diethylene Glycol Monomethyl Ether (>99%)
Isopropyl Alcohol (Reymerink)	Windshield de-ice fluid	Isopropanol
Jet-Clean 91 (Turco)	Aircraft Cleaner	Water based, completely biodegradable
Shell Tellus Oil 46	Hydraulic Oil	Highly refined mineral oils; <3% (w/w) DMSO-extract
AeroShell Fluid 12	Synthetic lubricating oil for general purpose aircraft use	Barium dinonylnaphthalene sulfonate (1-5%)

4 Crosslinking of Phenylethynyl Terminated LCT Coatings

4.1 Summary

The different environmental and curing conditions of LCT coatings applied on aluminum might influence the curing behavior with respect to that of previous research based on bulk samples. The evolution of thermal properties, morphology, and mechanical properties in the nano- and microscale were, therefore, investigated at various stages during the curing process. It was found that, although there is a limited effect of curing on the more superficial section of the coating, the thermal and elastic properties improve during the initial approximately 60 min of curing. On the other hand, curing consistently delays failures and increases scratch resistance during about 75 min, when there is a shift towards interfacial failure. An optimum curing time from 60 to 75 min was identified, although the final choice would depend on the specific application of the coating.

4.2 Introduction

The first step necessary to characterize a new crosslinkable coating material, and define potential applications, is to obtain an optimally cured coating. It is, therefore, necessary to understand first the curing behavior of the material. The curing of these phenylethynyl terminated LCTs was largely investigated during their development and the study of their initial applications in composite structures [27, 38, 68, 70, 71, 118]. The curing behavior of coatings, however, might differ from that of the bulk material. The coating process causes the polymer to undergo a different thermal history. Moreover, the intimate contact with the aluminum substrate and different curing conditions will affect the final product even further. Roberts et. al. [75] emphasized that the relative proportions of the various cure products, and, hence, mechanical properties, were dependent not only on the molecular weight and structure of the oligomer, but also on the thermal history and curing temperature. Additionally, they concluded that because of their insoluble/intractable nature, the cured phenylethynyl resins are difficult to characterize.

The aim of the present chapter is to contribute to the understanding of the complex crosslink behavior of phenylethynyl-terminated LCTs as coatings applied onto aluminum. The evolution of physical and mechanical properties was investigated at various stages during the curing process. In the first part of this work, the evolution of the surface morphology and thermal properties was analyzed. In the second part, we addressed the development of surface and subsurface mechanical properties using nanoindentation and constant load scratch test. In the last part, the scratch behavior and interface properties were analyzed by means of scratch tests with linearly increasing load.

4.3 Materials and characterization

A 5000 $\frac{g}{mol}$ reactive LCT oligomer was synthesized, and melt-pressed onto a grit-blasted (GB) aluminum AA5083-H111 substrate, as described in Chapter 3. The samples were then cured for 0, 30, 45, 60, and 75 min at 370 ^{o}C; the final thickness of the coatings was approximately 60 µm.

Thermal analyses were performed using a differential scanning calorimeter (DSC) and a thermo balance (TGA). The surface morphology was investigated using a scanning electron microscope (SEM) and confocal microscopy (CM); CM was also used for roughness measurements. For SEM analysis, samples were prepared by sputtering an ultra-thin gold layer to avoid electrostatic charging on the surfaces. The thickness of the LCT coatings was measured on several points by eddy currents using a coating thickness gauge for non-ferromagnetic metals, and average values were calculated.

The elastic modulus (E) and hardness (H) of the coatings were measured using a nanoindenter coupled with a constant stiffness measurement (CSM) module. Typically, 25 indents were obtained for individual specimens, and the average was calculated. The elastic recovery (ER) and scratch behavior was investigated using a microscratch tester equipped with a 100 µm radius Rockwell tip. Constant load tests were performed at normal loads of 1, 2, 4, and 6 N; and progressive load tests consisted in a linearly increasing load from 0.04 to 30 N along a scratch length of 8 mm. Scratches were performed three times per coating system; and the failure modes associated with the scratch test were identified by post facto observation of the scratch track using SEM and CM.

4.4 Results and discussion

4.4.1 Thermal analysis

Thermal analysis of melt-presses coatings was performed to investigate the effect of coating application and curing on the thermal behavior of the LCTs. Fig. 4.1

shows the DSC measurements of a 5000 $\frac{g}{mol}$ LCT coating before and after curing it for 30 and 60 min. The LCT showed a T_g of 100 ºC and T_m of approximately 280 ºC, which are in agreement with the values reported previously [27]. Since the transitions in semicrystalline and liquid crystalline polymers are highly dependent on the thermal history of the sample, the material extracted from the coatings was annealed in vacuum at 250 ºC for 24 h prior to the thermal analysis.

Fig. 4.1 shows a progressive reduction and subsequent elimination of the melting endotherm. This reduction and elimination of the melting endotherm is an indication of crosslinking and reduced mobility of the reactive oligomer, with the subsequent restriction of the melting behavior [27]. After curing, the T_g of these polymers becomes barely detectable with DSC. Dynamic mechanical analysis (DMA) of cured free standing LCT films reported a T_g of approximately 120 ºC for the cured 5000 $\frac{g}{mol}$ oligomer [27].

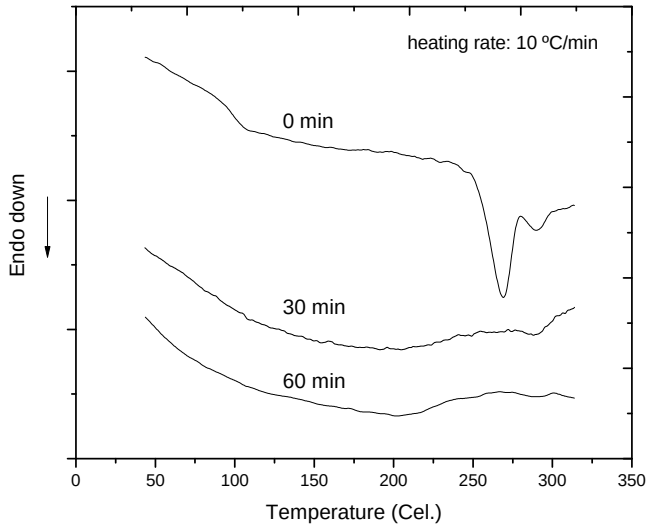

Figure 4.1 – Differential scanning calorimetry of the 5000 $\frac{g}{mol}$ LCT after 0, 30, and 60 min showing a progressive reduction and elimination of the enthalpy of transition corresponding to the melting endotherm

The DSC traces of the reactive oligomer show two minima in the melt endotherm. These two different types of transition processes were earlier observed by Knijnenberg [119], and were related by Cheng and Chung et. al. [120, 121] to a fast crystallization and a subsequent process associated with crystal perfection. The results indicate that the first (and fast) crystallization is restricted during the initial crosslinking, but short range movements can still occur. It is important to mention here that these crystallizations are not necessarily related to the molecular alignment and domain formation. LCPs like Vectra® are semi-crystalline polymers, where the crystals are formed by sections of adjacent aligned molecule segments (see Chapter 2, Fig. 2.9).

The thermal stability of the LCT is related to the crosslinking degree, and is a potential indicator of the progress of the curing during the study of phenylethynyl terminated thermosets. The TGA measurements presented in Fig. 4.2 show a progressive increase in the thermal stability of the LCT with increasing curing time. Curing the 5000 $\frac{g}{mol}$ oligomer during 60 min at 370 ^{o}C increases the T_{99} and T_{98} by 16 % and 8.5 %, respectively.

As we can see in Fig. 4.2, the thermal stability increases very rapidly during the first 45 min. After this initial period, not all end-groups have necessarily reacted to produce chain extension or crosslinking, but the crosslinking rate seems to decrease to a great extent. After 60 min of curing, there is only a small increase in the stability, suggesting that after 45 min there is a considerable reduction in the mobility of the molecules and the polymer is close to reach saturation in its crosslinking capability.

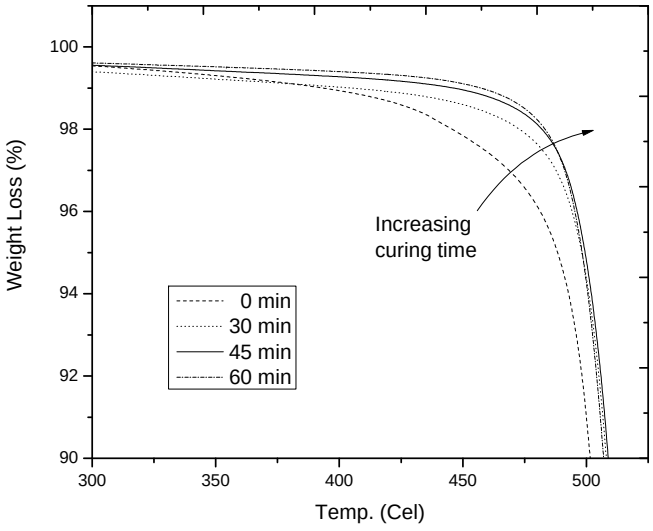

Figure 4.2 – Thermogravimetric measurements of the 5000 $\frac{g}{mol}$ LCT coating on aluminum after curing 0, 30, 45, and 60 min

4.4.2 Surface properties

The evolution of the coating topography, as observed by confocal microscopy (CM), is illustrated in Fig. 4.3. The pressed film had a smooth and uniform surface; however, the surfaces become progressively rougher with increasing curing time. The arithmetic average of the amplitude of the surface height shows a logarithmic increase in surface roughness with increasing curing time from 0 to 75 min (Fig. 4.4).

The morphology observed on the surface of cured coatings is related to the molecular orientation and the characteristic macroscopic fibrillar formation of LCPs [26, 122–124]. It can be observed, therefore, that melt-pressing produces non-oriented LCP

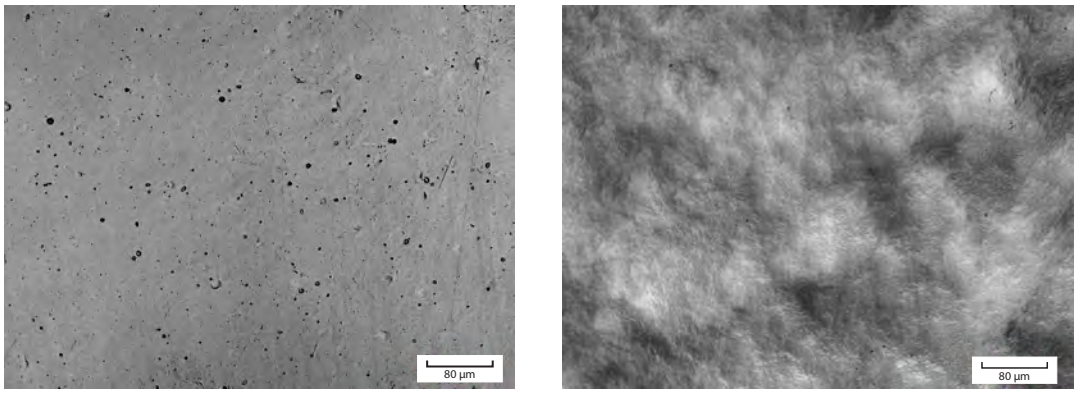

(a) **(b)**

Figure 4.3 – Confocal microscopy image of the surface morphology of a 5000 $\frac{g}{mol}$ LCT coating on aluminum after (a) 0 and (b) 60 min curing

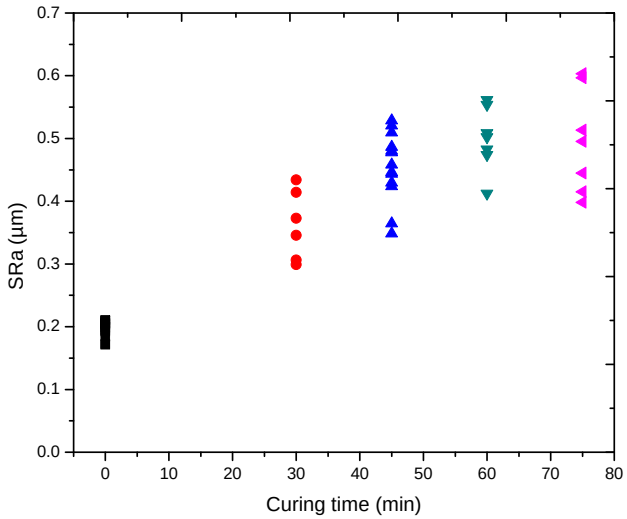

Figure 4.4 – Surface roughness (arithmetic average) of a 5000 $\frac{g}{mol}$ LCT as a function of curing time

coatings. This lack of a net macroscopic orientation during the melt-pressing of LCPs has been previously reported [125, 126].

A theory proposed by Sumiya et. al. [123] suggests that there is a correlation between crosslinking and aggregation, leading to inhomogeneity in mass and density, roughening polymer films. Recent studies have also investigated the role of crosslinking in the surface roughening of polymers [122], and concluded that polymer aggregation due to crosslinking induces surface roughening. The results presented here further support thes observations, since the studied LCTs contain no volatiles and roughness variations can be attributed to polymer re-ordering rather than emissions to the environment. This inhomogeneity, however, may lead to residual stresses and

affect the adhesion at the coating substrate interface.

4.4.3 Sub-surface properties

In the context of this work, the sub-surface is defined as the region of the coating just below the coating-air interface. It can extend to a maximum of approximately 10 % of the coating thickness, where properties start to be affected by the presence of the substrate [108]. The properties of this region may differ from that of the bulk due to the proximity of the external surface, where we could expect, for instance, chemical interactions with the environment or a gradient in shear stresses due to friction with the wall. A nanoindenter coupled to a CSM module was used to asses the elastic modulus and hardness of the LCT coatings at the sub-surface level, to a maximum depth of 2 µm. Fig. 4.5 and Fig. 4.6 present the average measured elastic modulus and hardness, respectively, as a function of curing time.

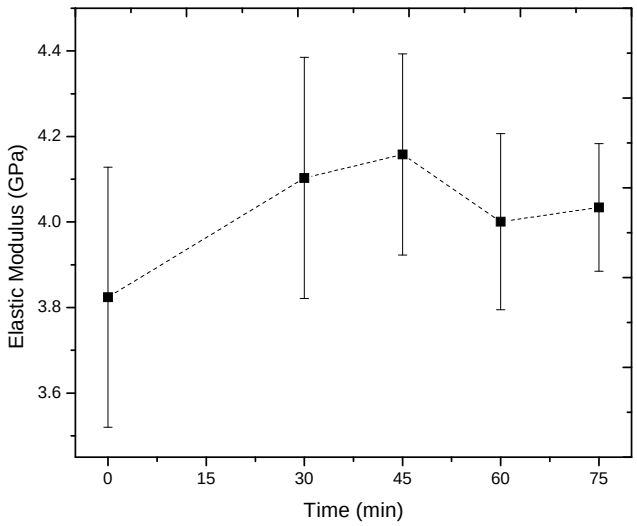

Figure 4.5 – Nanoindentation measured elastic modulus of a 5000 $\frac{g}{mol}$ LCT as a function of curing time at 370 ºC

The elastic modulus increases with the curing time, reaching a maximum of 9 % increase after 45 min of curing. This suggests that the sub-surface coating becomes stiffer, which is an indicative of a higher crosslinking density. The overlapping of the dispersion, however, is greater than the difference in the average measurements, and this hinders the identification of a clear trend in the variation of the properties. The hardness, on the other hand, seems to decrease slightly; although the overlap in the dispersion is also present.

These findings indicate that properties are not strongly affected by the curing process in a superficial level of the coating. This behavior could be related to surface phenomena, by which the surface could be undergoing a different curing behavior

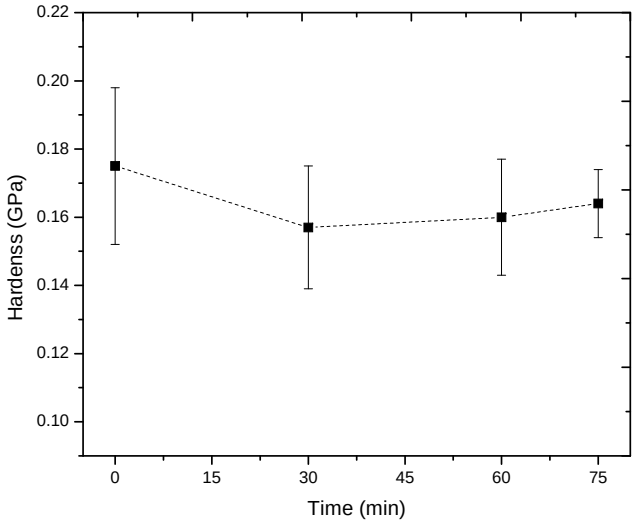

Figure 4.6 – Nanoindentation measured harness of a 5000 $\frac{g}{mol}$ LCT as a function of curing time at 370 ºC

than the bulk. In addition, nanoindentation measurements are influenced, for example, by surface roughness and local molecular orientation. On the other hand, during curing under vacuum, the heat flows from the rack of the oven to the substrate, and then into the coating; and a thermal gradient can develop through the thickness of the LCT layer, affecting curing kinetics. Therefore, since the gelation time increases from 10 to 54 min when the curing temperature is reduced from 370 to 340 ºC [118], the reduced improvement in the subsurface properties may be also affected by slower crosslinking kinetics in this region.

4.4.4 Bulk properties

During a microscratch test, the tip penetrates deeper than 10 % of the thickness of the coating, to a region where the mechanical properties are affected by the presence of the substrate. In the context of this work, we will refer to this region of the coating as the bulk. Fig. 4.7 shows the elastic recovery of a 5000 $\frac{g}{mol}$ LCT, measured directly after performing scratches with constant loads of 1 N and 2 N. The penetration depths were approximately 8.5 µm for a normal load of 1 N, and 15 µm for a load of 2 N. The figure indicates that curing the LCT for 45 min increases the elastic properties of the bulk 12 % and 27 % under loads of 1 N and 2 N respectively.

It is necessary to indicate here that the thermoplastic and thermosetting polymeric response to localized induced mechanical strain can be appropriately described as visco-elasto-plastic [109]. This means that part of the elastic strain will recover immediately, while the rest will recover over a period of time; and any permanent change in dimension after the visco-elastic recovery represents the plastic strain. The

results presented in Fig. 4.7 were obtained by means of a post-scan of the groove immediately after performing a scratch, and time-dependent elastic recovery may therefore not be completely included in these strain measurements. The elastic recovery is also affected by the mechanical failure of the material, as observed on the reactive oligomer (0 min) scratched at 2 N. Despite the influence of the microcracking on the ER of this data-point, the results show a clear trend, non dependent on the load.

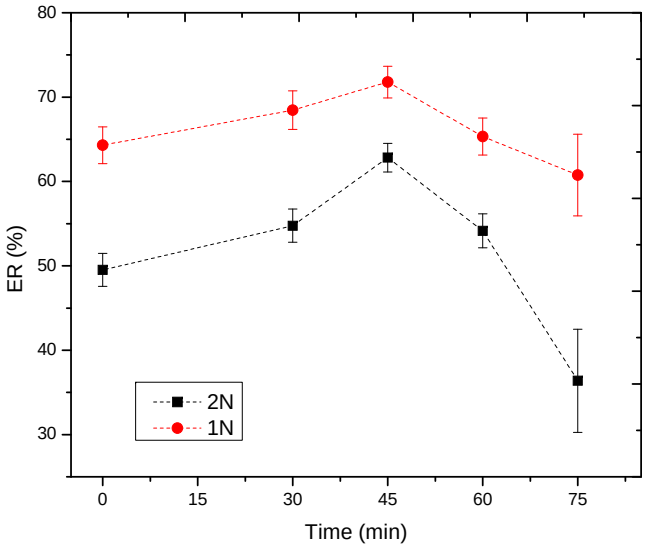

Figure 4.7 – Elastic recovery (ER) from a scratch performed at a constant load of 1 N and 2 N as a function of curing time at 370 °C

Fig. 4.7 shows that the elastic properties start decreasing at curing times longer than approximately 45 min; and after 75 min the ER has dropped considerably. To gain more understanding of this behavior and the overall scratch resistance of the coating, we analyzed the scratched surfaces with SEM.

SEM images of the grooves are presented in Fig. 4.8. At a load of 1 N, the scratches show equivalent plastic deformation independently from the curing time. Grooves with the same width and similar ridges are produced by plastic drawing and material pile-up at the sides of the scratch (Fig. 4.8 a to d). This shows that even though LCTs are brittle at ambient temperatures, ductile deformation and ploughing is present. Other brittle polymers like PMMA show the same behavior. Gauthier et. al. [111] explains that on visco-elasto-plastic materials like polymers, the matter affected by the tip is not removed but pushed in front of it, in this region, the compressive stresses generated by the tip cause large hydrostatic pressure, which favors shear and plastic deformation [109].

After the LCT starts crosslinking, the surface of the scratch presents pseudo fish-scale damage. This feature is smaller and more superficial than the fish-scale damage typical of ductile and weak polymers such as PP [112]. Periodical damages like fish-

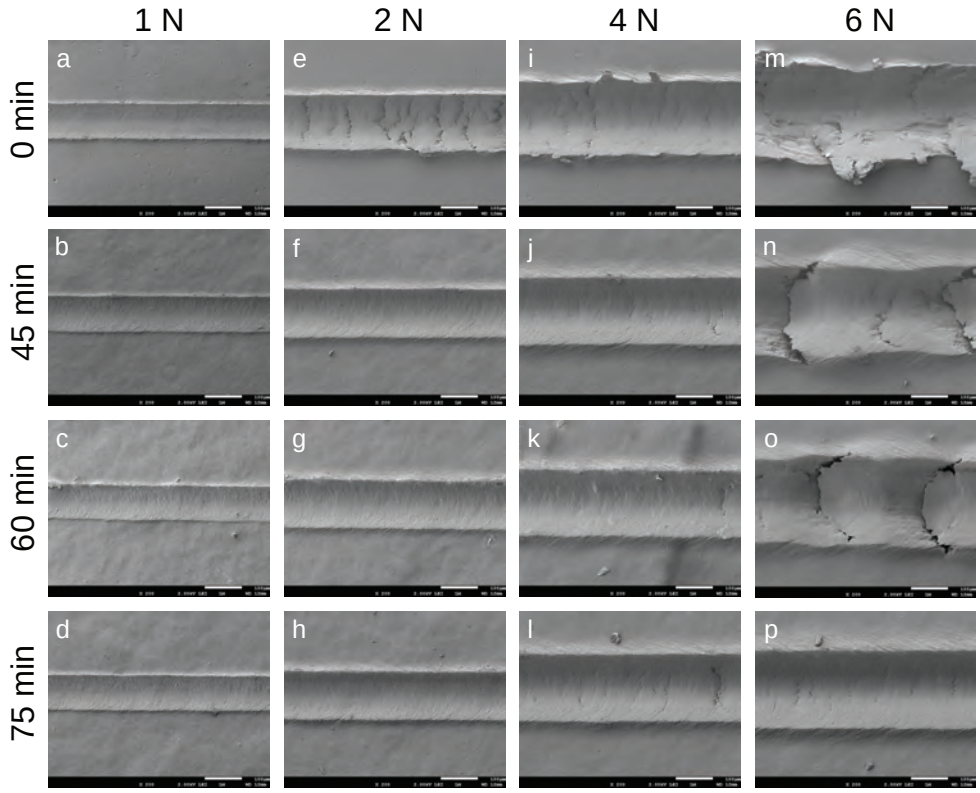

Figure 4.8 – SEM images of scratch grooves for a 5000 $\frac{g}{mol}$ LCT as a function of curing time at 370 °C at constant scratching loads of 1, 2, 4, and 6 N

scale are produced by a "stick-slip" phenomenon [114, 127]. The stick-slip behavior starts when the scratch tip ploughs through the material ahead of it and pushes the material forward [112]. The surface friction between the surfaces of the scratch tip and the material accumulated ahead of the tip introduces resistance against the tip movement. The velocity of the tip relative to the material surface drops, and the sticking phenomenon occurs. The stored strain energy continues to build up due to the applied normal load. When the stress on the polymer is lower than the ultimate strength of the material, the scratch tip will drag the material along and slip over the ridge of the pile-up region (Fig. 4.9 a). Because of the decrease in resistance for the tip movement, the tip can push forward in full speed again (Fig. 4.9 b), but due to the normal force the tip will soon begin to compress the material (Fig. 4.9 c), and the stick stage occurs again. Under a scratching load of 1 N, there seem to be no further effect of curing time on the morphology of the scratched surfaces, and there is no correlation with the observed reduction in the ER.

When the reactive LCT is scratched with a load of 2 N, the penetration depth is about 30 % of the coating thickness, and the deformation of the polymer is more strongly restricted by the presence of the substrate. Tearing cracks perpendicular to the scratch direction appear (Fig. 4.8 e). This tearing can be caused by high tensile

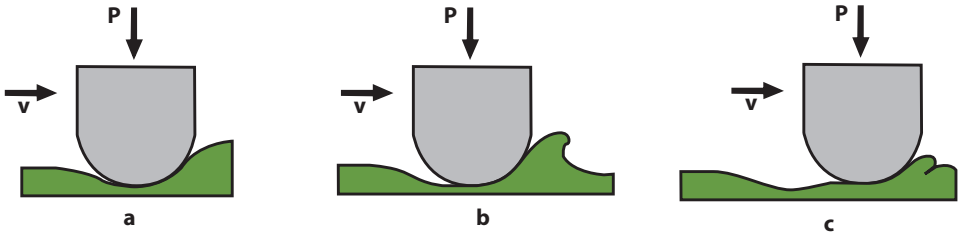

Figure 4.9 – Schematic illustration of the fish-scale formation originated by the stick-slip phenomenon. Adapted from [112].

stresses generated at the rear end of the indenter due to the frictional force between the indenter surface and the LCT (Fig. 4.10), and is dependent on the elastic modulus and fracture strength of the polymer. In brittle polymers like LCTs, a strain energy accumulation similar to the one produced in the "stick-slip" phenomenon occurs, but before the indenter slips over, as described above, the tensile stress magnitude in the region behind the scratch tip may have already reached its ultimate strength. Thus, brittle fracture takes place to release the accumulated strain energy (Fig. 4.11). This means that increasing the load from 1 N to 2 N, the reactive LCT no longer behaves purely ductile, but starts showing a degree of brittle response.

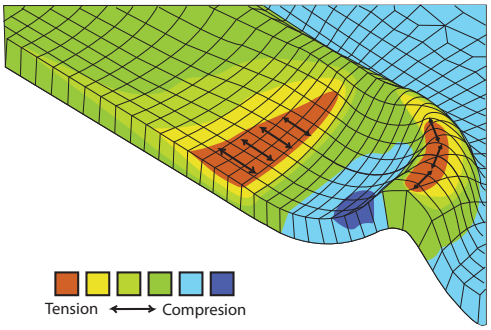

Figure 4.10 – Schematic representation of the principal stresses induced by the tip during a constant load micro-scratch test. Adapted from [112].

As soon as the polymer starts crosslinking, there is a very strong reduction in crack formation. Brittle fractures reduce to a microscale after approximately 30 min of curing, and seem to coexist with the pseudo fish-scale pattern and ductile ploughing described previously. After curing the polymer 45 min, the superficial microcracks are no longer formed under a load of 2 N (Fig. 4.8 f). These observations seem to reveal changes in deeper layers of the coating due to curing, while the surface of the coating still remains weak. No further change is observed on the surfaces scratched at a constant load of 2 N after curing 45 min. Therefore, no correlation was found also for this load, between the reductions in the ER, observed after curing more than 45 min, with the morphological changes in the scratch surface.

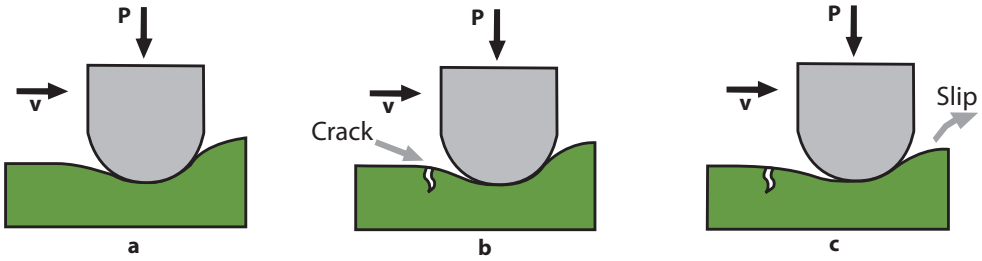

Figure 4.11 – Schematic illustration of tensile cracks formation originated by the stick-slip phenomenon. Adapted from [112].

Fig. 4.8 m to p show the progressive change in failure modes with increasing curing time, for a constant load of 6 N. Under this load, the scratch tip penetrates an average of 27 µm into the reactive oligomer coating and induces material removal (Fig. 4.8 m). After curing 45 min, the tensile stresses become radial at the rear edge of the tip [128], generating a periodic convex feature pointing opposite to the scratch direction (inverted-D), as showed in Fig. 4.8 n. They are also originated by the repetition of an energy-release process similar to microcracking. After approximatelly 60 min of curing, the mechanical properties increase and the material withstands the accumulation of a higher stress before failure, decreasing the frequency of crack formation [109]. Curing for 75 min, switches the failure mode to microcracking along the scratch path.

Under a load of 6 N, the effects of curing become more evident; and the behavior of scratch resistance with increasing curing time, as evaluated by the morphological changes observed at this load, do not correlate to that of the ER presented in Fig. 4.7.

4.4.5 Coating-metal interface properties

In order to further study the effects of curing on the scratch resistance and interface properties of the LCT coatings, progressive scratch tests were performed on the 5000 $\frac{g}{mol}$ LCT samples cured 0, 45, 60, and 75 min at 370 ^{o}C. Fig. 4.12 shows SEM micrographs of the scratch surfaces. During testing, a variety of failure modes were observed. Some of these failure modes depend on detachment at the coating-substrate interface, and are thus of direct relevance to the scratch test as a measure of adhesion. Failure modes which depend on plastic deformation and fracture within the coating, rather than at the coating-substrate interface, may be used to asses the coating quality for tribological applications [128]. In other words, the behavior at low loads can be used to analyze the wear and scratch behavior of the LCTs, while the behavior of the polymer under higher normal loads would provide information about the interface behavior.

The initial damage observed during the test of the reactive oligomer (i. e., the non-cured coatings) is a non-recoverable plastic deformation resulting from compressive

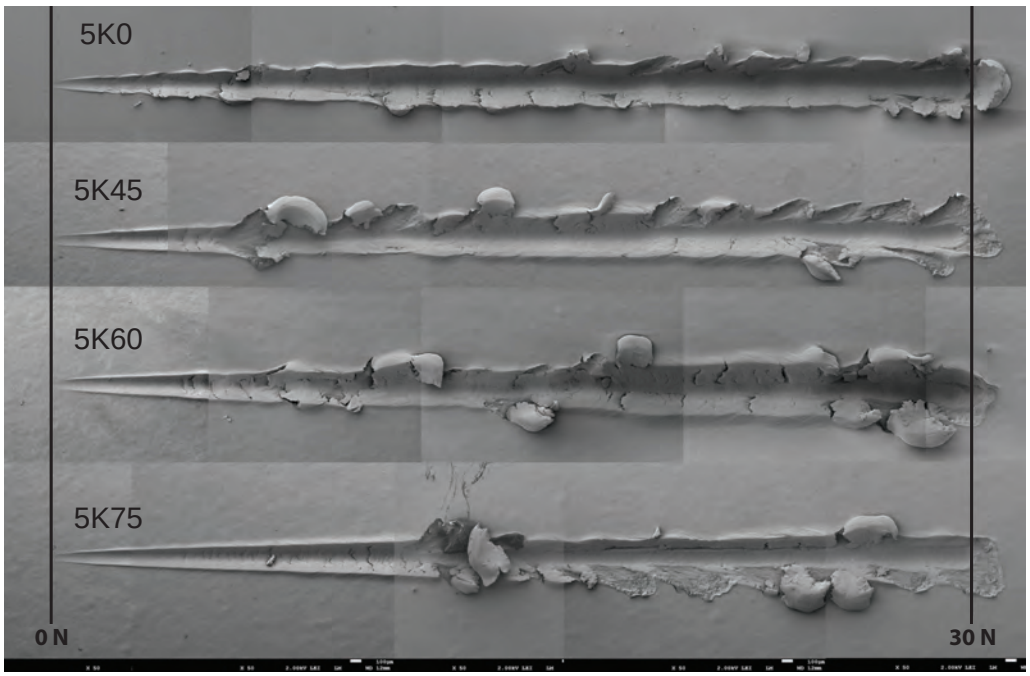

Figure 4.12 – SEM images of scratch grooves with a progressive load increase for a 5000 $\frac{g}{mol}$ LCT as a function of curing time at 370 ºC. The load was linearly increased from 0.04 to 30 N over a scratch length of 8 mm.

indentation (known as "mar"). Subsequently, the reactive oligomer shows an onset of tearing and material removal at a normal load of approximately 2 N, with the subsequent formation of debris (Fig. 4.13 a). As the load increases, there is a continuous perforation of the coating, with further material removal. When the tip reaches the substrate, it is visually exposed as showed in Fig. 4.13 b. The fracture surfaces show a ductile fracture with plastic deformation, and the lack of fibrillar structure (Fig. 4.13 c). At higher loads, a zone with interfacial spallation at the borders of the scratch track begins, where the substrate is also exposed. This lateral damage does not propagate, suggesting a low cohesive strength for the non-crosslinked polymer (Fig. 4.14 a).

After curing the reactive oligomer for 45 min at 370 ºC, the "mar" zone extends to slightly higher loads. After this zone, the onset of microcracking was observed. In a later stage, parabolic cracking becomes the dominant failure mode, as showed in Fig. 4.15 a. These parabolic cracks can easily propagate outside the scratch track, originating spallation prior to the tip reaching the substrate, and accelerating considerably the onset of this failure mode. This spallation is now cohesive; and it propagates further away from the scratch track borders (Fig. 4.14 b). There is no further shift in failure mode when the tip reaches the substrate; however, more polymer seems to remain in the scratch track compared to non-crosslinked samples, and the substrate is visible only in sporadic spots (Fig. 4.16). In addition, the fracture surfaces show a clear fibrillar structure (Fig. 4.17), typical of liquid crystalline

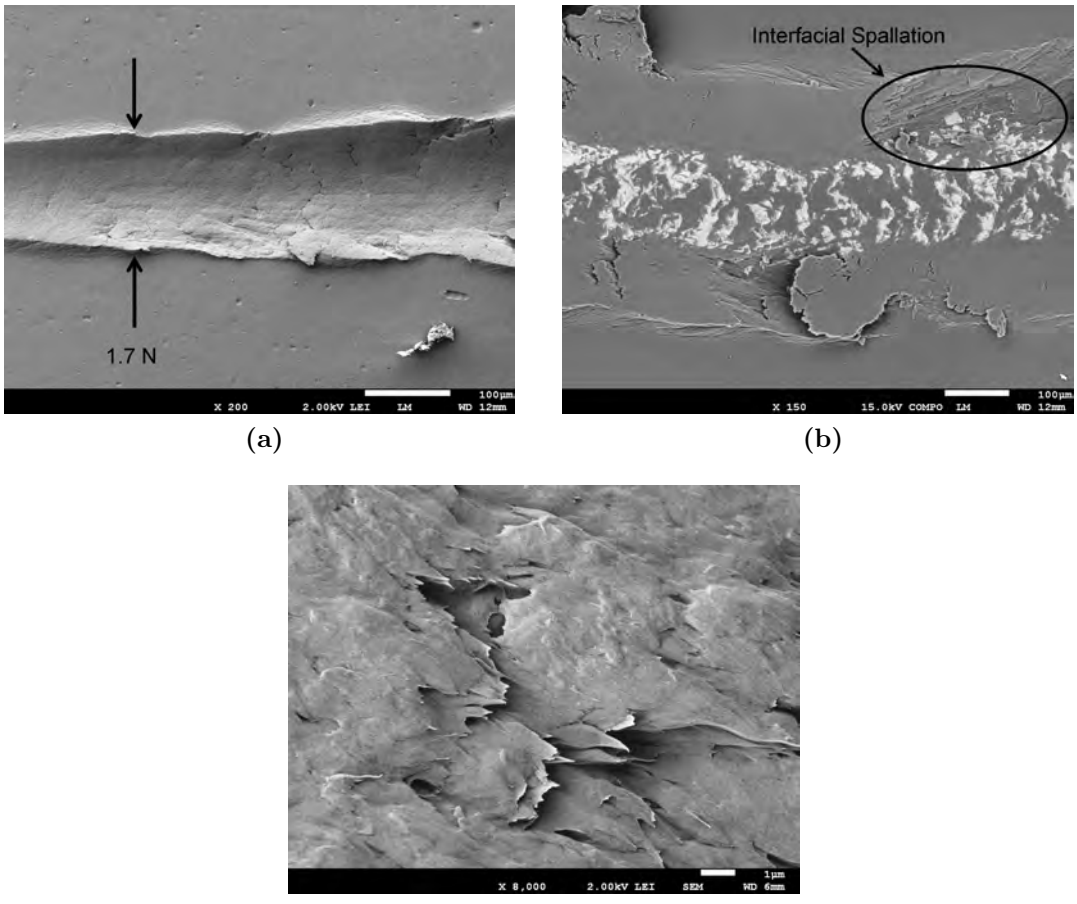

Figure 4.13 – SEM images of the reactive oligomer scratched under a linearly increased load showing (a) initiation of the material removal zone, (b) interfacial spallation of the coating, and (c) detail of the surface fracture of the coating

polymers.

Jiang et. al. [112] explained that a higher strength and elastic recovery may extend the "mar" zone, delaying the onset of failures. Curing the LCT resins 60 min, in fact, appears to delay the onset of microcracking approximately 46 %, compared to the coatings cured 45 min (Fig. 4.15 b). This improvement, however, can not be attributed to an improvement in the elastic properties (see Fig. 4.7); therefore, this improvement might be due to higher polymer strength.

Further on, the scratch path is equivalent to that of LCTs cured 45 min. Parabolic cracks (inverted-D shape) begin to form at the same load as in the previous case (approximately 4 N) and become the dominant damage mode. The surface of the scratch tracks also show the same behavior as in the case of coatings cured 45 min. The first exposure occurs at approximately the same normal load; and the fracture surfaces show equivalent fibrillar structure to that already seen after curing 45 min.

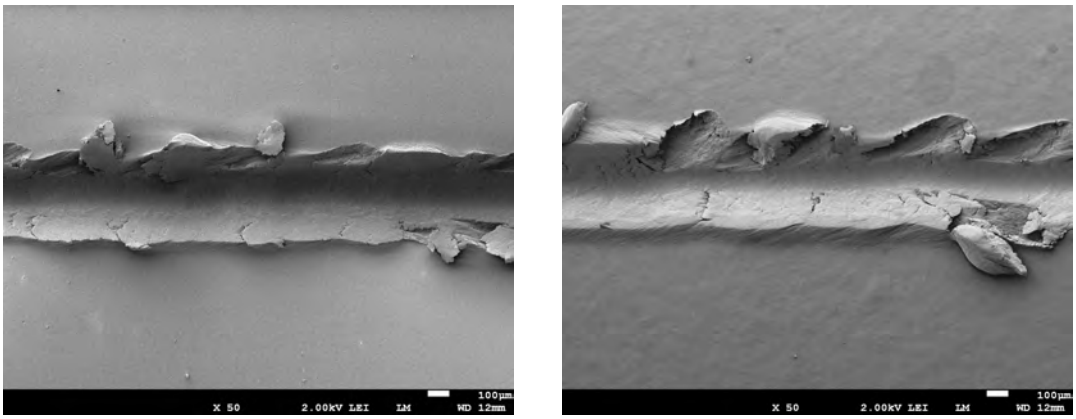

(a) **(b)**

Figure 4.14 – SEM images of the spallation originated during the scratch test on the reactive LCT coating (a) and on an LCT coating cured 45 min at 370 ^{o}C

An increase in the curing time to 75 min, does not delay further the onset of microcracking; however, instead of shifting rapidly into parabolic cracking, the microcracks grow (tensile cracking) and the zone extends until the tip reaches the substrate, at a load of about 12 N (Fig. 4.18 a). This means that the scratch behavior at low loads improved, an indication of higher cohesion. On the other hand, the spallation along the scratch track switches back into interfacial (Fig. 4.18 b). Interfacial failure along the scratch track also increases. This shift towards interfacial failure may be a result of the increase in polymer cohesion. It could be also potentially favored by a weakening of the interfacial properties due to localized residual stresses originated by polymer agglomeration during the crosslinking process. Fracture surfaces also show a fine fibrillar structure (Fig. 4.18 c).

The evolution of the scratch damages for the various curing times discussed in this section are summarized in the scratch map presented in Fig. 4.19. The failure mechanisms observed when the tip reaches a load of approximately 6 N, correlate with those observed during the tests at this constant load. The overall scratch behavior was also observed to improve with increasing curing time.

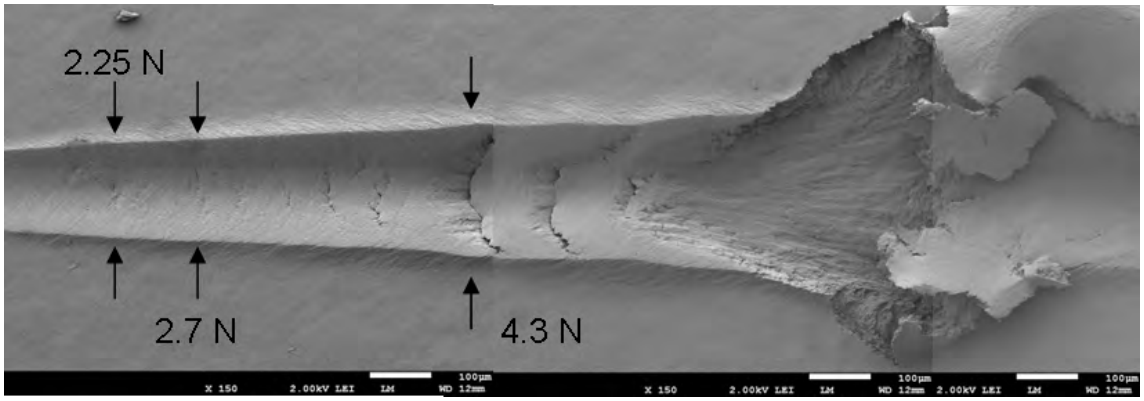

(a)

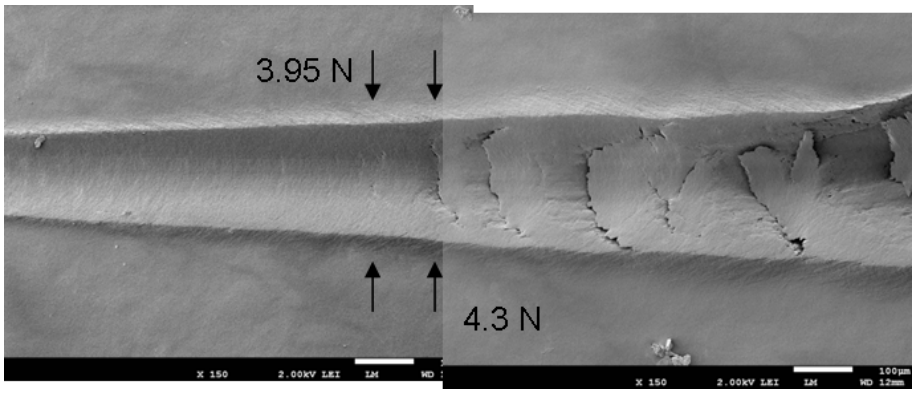

(b)

Figure 4.15 – SEM image of the scratch track of an LCT coating cured 45 min (a) and 60 min (b) at 370 ^{o}C, showing the microcracking and parabolic cracking zones. The normal loads that initiated the failure zones are indicated.

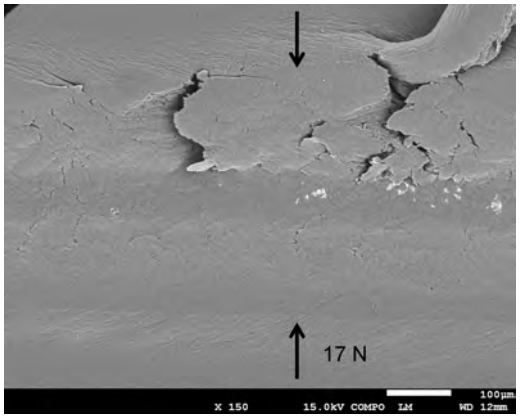

Figure 4.16 – SEM image of the scratch track of an LCT coating cured 45 min at 370 ^{o}C, showing the surface of the scratch path. The white spots indicate where the substrate is exposed. The normal load is indicated as a reference.

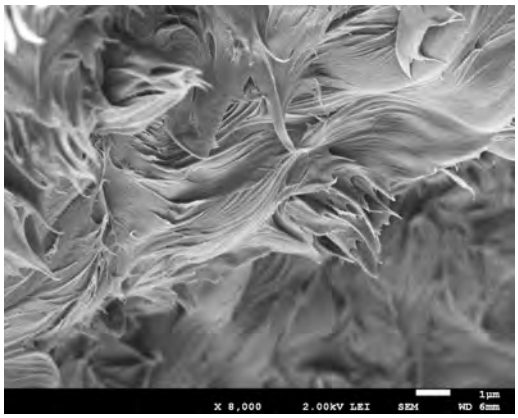

Figure 4.17 – SEM image of the spalled region of an LCT coating cured 45 min at 370 °C, showing the fibrillar structure characteristic of liquid crystalline polymers

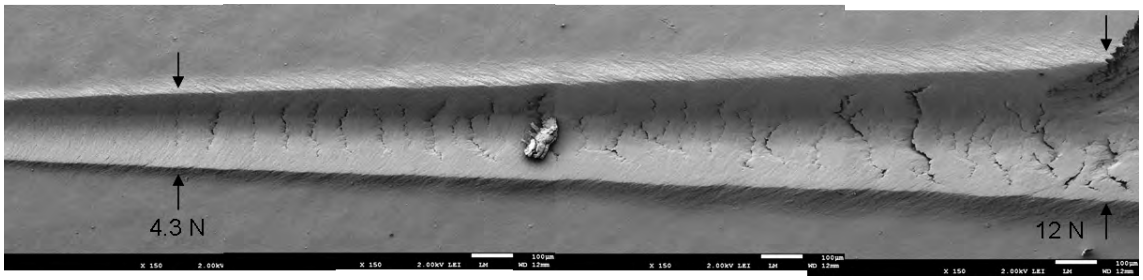

(a)

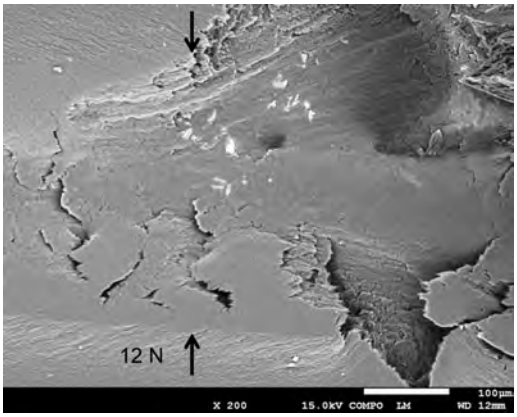

(b)

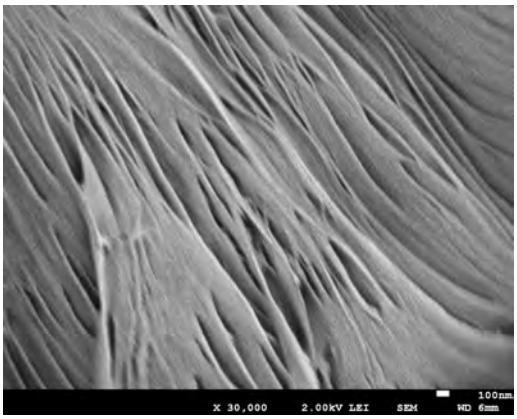

(c)

Figure 4.18 – SEM images of the scratch track of an LCT coating cured 75 min at 370 °C. The figure shows the microcracking zone (a), the initial interfacial spallation (b), and the fibrillar structure observed on the fractured surfaces (c). The normal loads that initiated the failure zones are indicated.

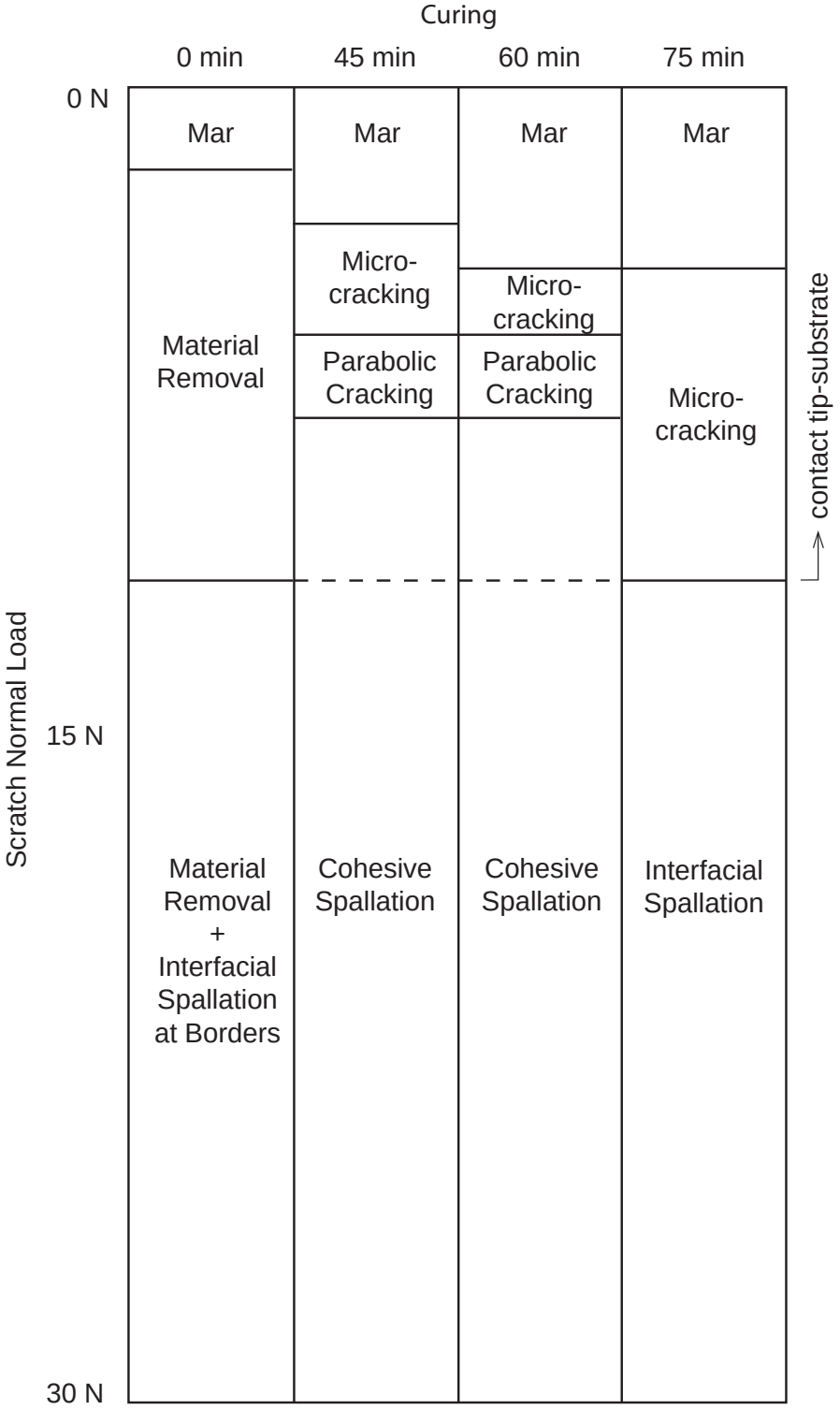

Figure 4.19 – Evolution map of polymer scratch damage

4.5 Conclusions

During the development of these phenylethynyl terminated LCTs, the nominal curing time was determined to be 60 min at 370 ^{o}C. On the other hand, LCT coatings on aluminum have a different thermal history, and are subjected to different curing conditions, in intimate contact with a metallic substrate. The curing behavior might, therefore, differ from previous studies on bulk samples. It is, therefore, critical to study the curing of LCTs as thin coatings applied on aluminum.

As a first step, a certain degree of crosslinking was confirmed by the increase in thermal stability and elimination of the melting endotherm, which indicates a reduction in the mobility of the molecules. It has been also observed that the different thermal treatment and curing conditions affected slightly the thermal behavior and characteristics of the LCT, with respect to previous analysis on bulk and film samples. During curing, the coatings develop a progressive increase in roughness that could be attributed to an aggregation of polymer chains. Such aggregation of molecules can be observed by the formation of fibrils, and would potentially induce internal stresses at the coating-substrate interface, degrading interfacial properties.

Curing shows a limited effect on the mechanical properties at a superficial level. It was also recognized that the effect of curing becomes more noticeable with increasing depths, as observed by the more evident change in scratch behavior as a function of curing time with increasing normal load. This could be attributed to a different curing behavior due to surface phenomena; but also to the curing process, were the heat is conducted to the LCT through the substrate material. This would induce a thermal gradient along the thickness of the coating, and reduce crosslinking kinetics.

Although results showed that the thermal and elastic properties did not improved considerably with curing times longer than 60 min, there is a further increase in cohesion with longer curing time. This, however, seems to shift the coating failure towards the interface, potentially aided by localized residual stresses developed during curing. As a consequence, the substrate is more exposed along the scratch path and interfacial failures begin to occur on the lateral spallation. At this point, we can conclude that the optimum curing time seems to be between 60 and 75 min, where the parabolic cracking is eliminated and the interfacial failure avoided.

5 Influence of Molecular Weight on the Properties of LCT Coatings

5.1 Summary

The present chapter explores how the molecular weight of the reactive oligomer affects the topography, mechanical properties, scratch resistance, and adhesion of LCT coatings to aluminum. Nanoindentation and microscratch testing were used to characterize a series of samples with increasing molecular weight (M_n). In addition, electron and confocal microscopy were used to analyze the surface morphology and fracture mechanisms of the coatings.

The results show an important influence of the M_n on the roughness; additionally, a reduction in adhesion with increasing Mw was also observed. Results indicate that the roughening is originated by a reorganization of the rigid-rods, and suggest that the new phenylethynyl polar groups contribute to the improvement of adhesion.

5.2 Introduction

The M_n of the reactive oligomer is one of the main parameters affecting the final properties of the LCT coatings. One of the reasons is that the starting M_n determines the mobility of the molecules. This affects the capability to reorganize, increase order and packing, and, ultimately, influences the occurrence of chain extension or crosslinking [27]. In addition, as explained in Chapter 3, the M_n of the oligomer is related to the concentration of end-groups, which may affect the interfacial properties and crosslinking of the coating.

Previous research on phenylethynyl terminated LCTs has focused on the influence of M_n on the liquid-crystalline phase formation, and its effect on thermal and mechanical properties of the bulk material [27, 38, 75, 118, 129, 130]. Currently, there is a lack of knowledge concerning the effect of M_n on the morphology, mechanical and interfacial properties, and scratch resistance of LCT coatings.

The purpose of the present chapter is to provide more understanding of the effect of the M_n (and, subsequently, end-group concentration) on the surface, mechanical,

and interface properties of the LCT coatings. A series of phenylethynyl terminated liquid crystalline thermosets with increasing M_n were studied and compared with a reference sample equivalent to the commercial thermoplastic Vectra® A950.

Firstly, the effects of M_n on the surface morphology are identified by confocal (CM) and electron (SEM) microscopy. Subsequently, nanoindentation is used to investigate the influence of M_n in the sub-surface, and constant-load microscratch testing is performed to determine the effects on mechanical properties and scratch resistance in the bulk of the coating layers. Finally, the possible effects of M_n on the adhesion and interface properties of the LCTs are studied using progressive-load microscratch testing.

5.3 Materials and characterization

A phenylethynyl terminated, Vectra-based liquid crystalline thermoset with a M_n of 5000 $\frac{g}{mol}$ was synthesized as described in Chapter 3. Additional LCTs with M_ns of 1000, 9000, and 13000 $\frac{g}{mol}$ and a non-end capped 30000 $\frac{g}{mol}$ LCP were also synthesized in our facilities at the Delft University of Technology by Knijnenberg et. al. [27], and kindly provided for the present research. The molecular structure of the LCP sample is equivalent to the commercial LCP Vectra® A950.

The liquid crystalline resins were first melt-pressed onto a grit-blasted (GB) AA5083-H111 aluminum alloy substrate, as described in Chapter 3. Due to the dependence of the melting temperature and viscosity with M_n, the melt-pressing parameters were adapted for each sample to obtain good quality coating layers. The samples were then cured for 60 min at 370 ^{o}C. The average thicknesses of the coatings are presented in Tab. 5.1.

The elastic modulus (E) and hardness (H) of the coatings were measured using a nanoindenter coupled with a constant stiffness measurement (CSM) module. Typically, 25 indents were obtained for individual specimens, and the average was calculated. The elastic recovery (ER) and scratch behavior was investigated using a microscratch tester equipped with a 100 µm radius Rockwell tip. Constant-load tests were performed at normal loads of 1, 2, 4, and 6 N; and progressive load tests consisted in a linearly increasing load from 0.04 to 30 N along a scratch length of 8 mm. Scratches were performed three times per coating system; and the acoustic emissions during the scratch tests were recorded. The morphological analysis of surface topography and failures was performed using scanning electron microscopy (SEM) and confocal microscopy (CM); CM was also used for roughness measurements.

It is important to remember here that the properties at the nanoscale are virtually unaffected by coating thickness [131], but are sensitive to local inhomogeneities and surface roughness [104, 108]. On the contrary, at the microscale, the local inhomogeneities and roughness have less impact, but the interaction with the substrate becomes more relevant [108].

5.4 Results and discussion

5.4.1 Surface roughness and morphology

For all M_n, melt-pressed coatings showed a smooth surface equivalent to that shown in Fig. 4.3 a. As described in the previous Chapter, curing induced roughening of the surfaces. The roughening was attributed to an agglomeration of polymer backbones during crosslinking. This is a diffusional process; and, therefore, it is affected by the mobility of the molecules. Chung [132], for instance, based on studies on 193 nm photo-resist polymer, found that lower M_n (due to chain scissioning in this case) increases the polymer surface roughness. As a consequence, the roughening is expected to depend on the M_n of the reactive oligomer [132, 133]. The effect of M_n on the roughening of the coating surface during curing is presented in Fig. 5.1.

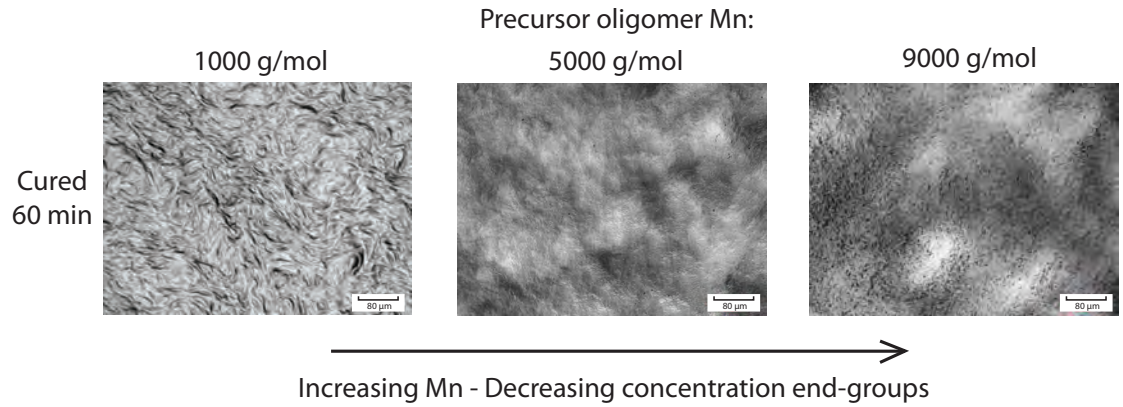

Figure 5.1 – Confocal microscopy images showing the surface morphology developed on 1000 (left), 5000 (center), and 9000 (right) $\frac{g}{mol}$ LCTs after curing 60 min at 370 ºC

As expected, the morphology of the coatings was found to depend on the M_n. Results show that a low M_n leads to a fine, regular roughness, while a high M_n induces a coarser and irregular morphology. This variation in the size of the polymer aggregates could be attributed to the variation in the mobility of the rigid-rods caused by the change in M_n. These results support the relation between the roughening and the M_n, or, equivalently, between roughening and chain mobility. This, in turn, reinforces the hypothesis that the roughening is induced by an agglomeration or aggregation of polymer chains.

Additionally, as discussed in Chapter 4, this morphology could be associated with the molecular orientation of the LCT layers. Therefore, these results show that there is no macroscopic orientation of the molecules in the melt-pressed coating, independently of the M_n.

5.4.2 Sub-surface properties

To analyze the effect of M_n on the sub-surface mechanical properties, the elastic modulus (E) and hardness (H) were studied using depth controlled nanoindentation. Coatings with a M_n of 1000, 5000, 9000, and 13000 $\frac{g}{mol}$ were studied before and after curing; and the E and H of a non-end-capped Vectra-type LCP with a M_n of 30000 $\frac{g}{mol}$ were also investigated. The results are presented in Fig. 5.2.

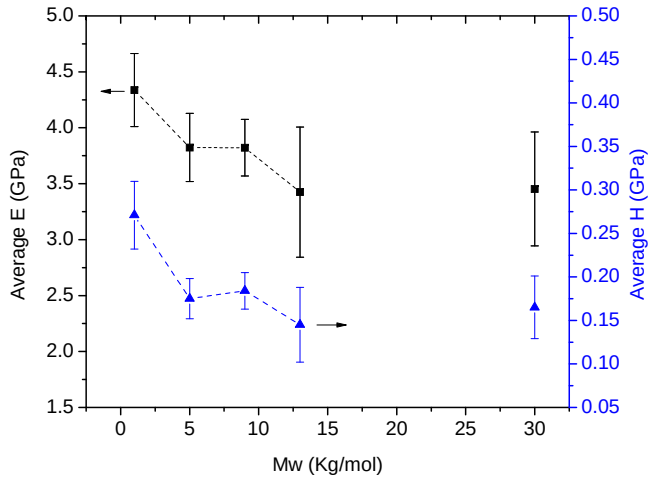

(a)

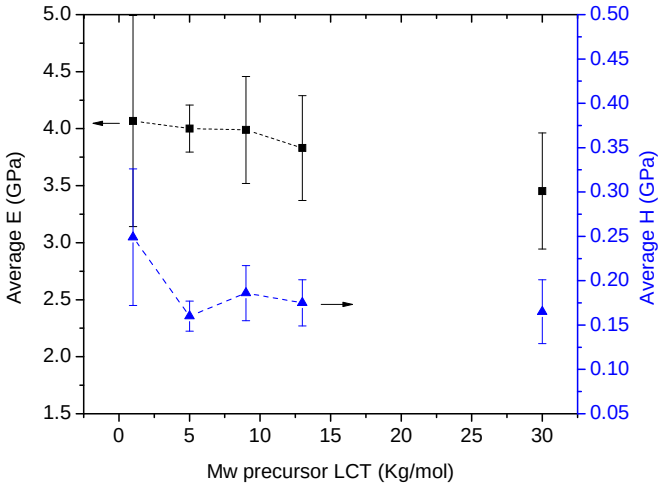

(b)

Figure 5.2 – Nanoindentation measured elastic modulus and hardness for 1000, 5000, 9000, and 13000 $\frac{g}{mol}$ LCTs before (a) and after (b) curing 60 min at 370 ºC. The results for a 30000 $\frac{g}{mol}$, non-end-capped Vectra-type LCP are also indicated.

As indicated in Fig. 5.2 a, the E and H of the reactive LCT decrease with increasing M_n. The results in this figure (i.e., for non-cured coating) are not affected by

variations in the roughness, since all melt-pressed oligomer coatings presented an equivalent smooth surface. The lowest M_n LCT presents the highest E and H, and the 13000 $\frac{g}{mol}$ LCT shows values equivalent to that of the non-end-capped thermoplastic. This behavior can be attributed to the microstructure of the low M_n polymers, since, at this scale, properties are dependent on localized changes in polymer density, degree of crystallinity, packing, voiding, etc. [104, 108]. As discussed in the next section, this behavior is opposed to the elastic recovery observed at a larger scale.

After curing, the 1000 $\frac{g}{mol}$ LCT shows an increase in the dispersion of the results (Fig. 5.2 b). This behavior suggests that the higher density of reactions, due to the higher concentration of end-groups, induces a loss of order and packing. As the M_n increases, however, no trend is observed in the reduction of the error bars, which could be attributed mainly to the polydispersity and the exponential decrease in end-groups concentration (Tab. 5.1).

No significant change in the properties of the higher M_n LCTs was observed, except for a slight increment in the 13000 $\frac{g}{mol}$ oligomer. As a result, although the dispersion hinders an unambiguous conclusion, the E of all the LCTs studied seem to converge to a value approximately 0.5 GPa higher than the LCP counterpart (Fig. 5.2b). This observation correlates with previous dynamic mechanical thermal analysis [27], which indicates that the M_n of the precursor oligomer seems to have little to no effect on the storage modulus (E') of the final cured film (see Tab. 5.1).

5.4.3 Bulk properties

In this section, constant-load scratch testing was used to investigate the bulk behavior of the LCT coatings, and compare it with that of the thermoplastic LCP. First, the elastic recovery (ER) was analyzed as a function of the M_n before and after curing the LCTs. Subsequently, the scratch grooves were investigated in attempt to correlate observations with previous results.

It is necessary to mention here that the melt viscosities of the LCTs varied widely with the M_n (Tab. 5.1). The melt-pressing process was optimized to obtain good quality coatings with each of the M_ns used in the present work; however, lower M_n tends to produce thinner melt-pressed coatings due to the lower viscosity of the melt. Therefore, the final thickness of the various melt-pressed coatings ranged from 30 to over 120 µm in some of the samples (see Tab. 5.1). Since the thickness of the coatings affects the scratch behavior and ER, this must be considered during the analysis.

5.4.3.1 Elastic recovery

The ER of LCT coatings with increasing M_n were measured as explained in sec. 3.4.3.2. The results obtained using a load of 1 N are shown in Fig. 5.3. Similar results were

Table 5.1 – LCT properties as a function of the M_n of the reactive oligomer

M_n ($\frac{g}{mol}$)	Complex Melt-Viscosities* [27] (Pa×s)	End-group/Backbone Concentration Ratio ($\frac{mol}{mol}$)	Storage Modulus of Cured LCTs at 24 °C [27] (GPa)	Average Coating Thickness (µm)
1000	1	0.250	5.2	35
5000	3	0.048	3.5	60
9000	68	0.026	3.2	90
13000	320	0.018	3.9	90
30000	446	–	4.3	120

*After a 30 min isothermal hold

obtained with a load of 2 N; however, at this load some of the reactive LCT coatings showed micro-cracking. Since the mechanical failure of the material affects the ER, only the measurements at 1 N were considered in this analysis. In addition, at a constant load of 1 N, measurements are less affected by the constrains imposed by the substrate and the effects of coating thickness on the visco-elasto-plastic behavior.

Microscratching the reactive oligomer at a normal load of 1 N showed an increase in ER with increasing M_n (Fig. 5.3 a). This behavior is opposed to the variation of E observed during the nanoindentation testing of oligomers (Fig. 5.2 a). To understand this behavior, we need to consider that when moving from a nano- to a microscale, measurements are affected by a different set of coating properties. For example, melt-pressed LCT coatings are locally oriented (liquid crystallinity); but macroscopically, they are not (domains are randomly oriented). In addition, nanoindentation measurements are affected by surface roughness variations (in the case of cured coatings), while microscratching is influenced by the constrains imposed by the substrate and the coating hardness. All in all, results at the microscale show that the higher M_n of the reactive oligomer implies higher cohesion and elastic properties.

After curing the oligomers 60 min at 370 °C (Fig. 5.3 b), there is a considerable increase in ER for the low M_n (1000 $\frac{g}{mol}$) LCT. This low M_n LCT posses higher mobility and higher concentration of reactive end-groups; therefore, one can expect a strong effect of the curing process.

As the M_n increases, however, the increment in ER is less evident or negligible. Comparing Fig. 5.3 a and Fig. 5.3 b, it can be observed that, using a load of 1 N, already at 5000 $\frac{g}{mol}$ there is no detectable change in the ER of the coatings after curing 60 min. The exponential decrease in end-groups concentration and the higher restriction in mobility due to larger backbones seem to be rapidly restricting the effects of curing. This was already presented in the previous chapter, where the ER was also found to have a maximum at curing times of approximately 45 min. Although more extensive experimental results are required to state if this behavior

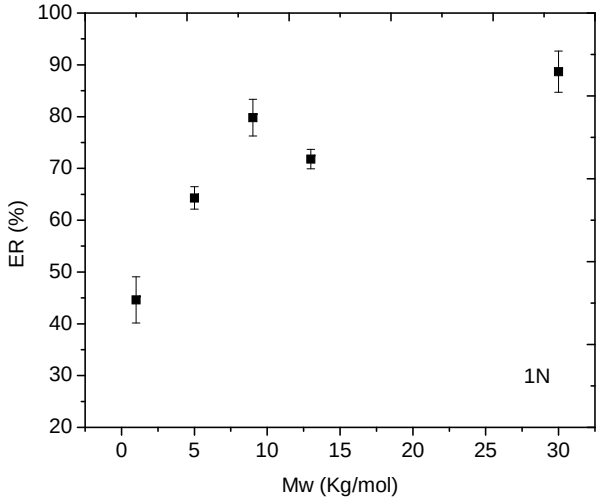

(a)

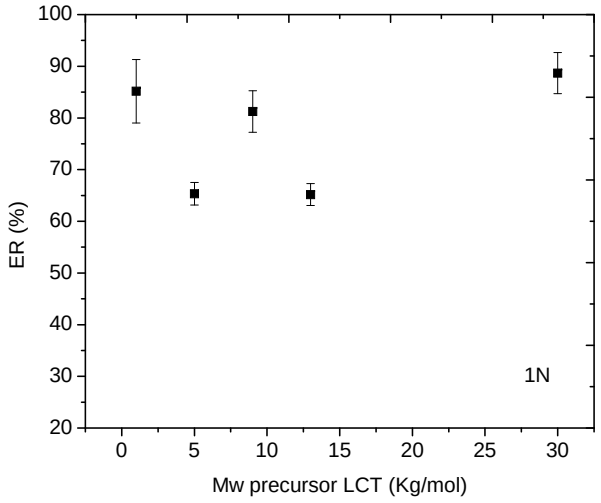

(b)

Figure 5.3 – Elastic recovery of the reactive LCT oligomers (a) and its cured products (b) measured after the application of a constant load of 1 N

can be further observed in all M_ns, preliminary results indicated such a tendency, suggesting a shorter optimum curing time for the optimization of the ER.

Finally, it will be important for the discussion in sec. 5.4.4, to note here that the properties of the reactive (non-cured) 13000 $\frac{g}{mol}$ LCT, as measured by nanoindentation and microscratch, are lower than those of the cured 9000 $\frac{g}{mol}$ products.

5.4.3.2 Scratch surface analysis

To gain more insight into the behavior of the bulk section of the coatings, the scratch paths produced during the constant-load tests were investigated using SEM. During the analysis of the ER, only the tests at a 1 N load were considered; in these tests, similar scratch grooves were produced and no failures where induced. To induce fractures and coating failures higher loads were required. Therefore, generalizations across all M_ns are now strongly limited by the variations in thickness. As an example, the 1000 $\frac{g}{mol}$ coatings have an average thickness of 35 µm, while the 9000 $\frac{g}{mol}$ are approximately 90 µm thick (see Tab. 5.1). At a normal load of 6 N, the tip penetrated through the 1000 $\frac{g}{mol}$ oligomer coating down to the substrate, while it plunges only about 35 % of the thickness of the 9000 $\frac{g}{mol}$ oligomer layer. Consequently, in this section, we will limit our analysis to the comparison of samples with equivalent thickness and percentage of penetration.

Fig. 5.4 a shows the scratched surface of two selected 1000 and 5000 $\frac{g}{mol}$ reactive LCTs samples with a similar thickness. We observed that at a constant load of 2 N, as the M_n increases, the failure mode switches from material removal to elasto-plastic deformation (mar) and tensile microcraking. Similarly, Fig. 5.4 b shows the scratch paths on 9000 and 13000 $\frac{g}{mol}$ coatings with similar thicknesses, scratched at a constant load of 6 N. In this case, there is a shift from microcracking and mar, to only mar or plastic deformation. This suggests that an increase in M_n improves the scratch resistance of the reactive oligomer (i. e., before curing), which is in agreement with the behavior of ER showed in Fig. 5.3 a.

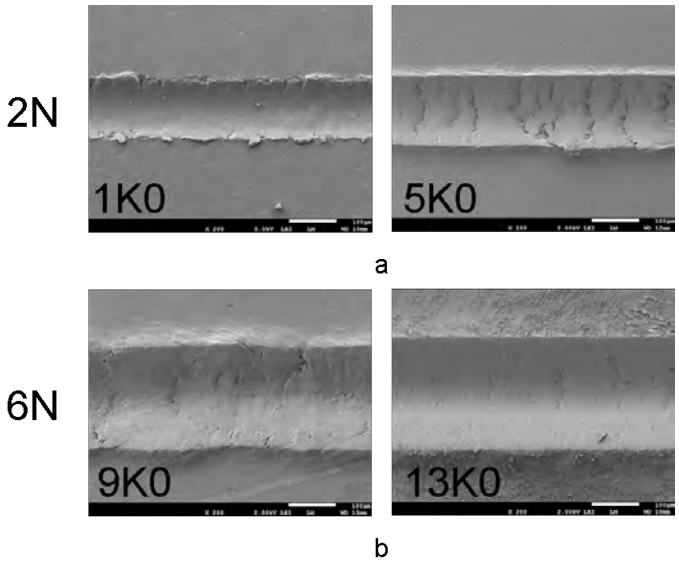

Figure 5.4 – Scratch tracks of (a) 1000 and 5000 $\frac{g}{mol}$ LCT coating with a thickness of approximately 45 µm under a constant load of 2 N, and (b) 9000 and 13000 $\frac{g}{mol}$ LCT coating with a thickness of approximately 90 µm under a constant load of 6 N (scale-bar = 100 µm).

The scratch behavior of these oligomer coatings after curing is presented in Fig. 5.5. Despite the limited effect of curing on the ER of the LCTs that was previously observed, samples show a noticeable improvement in scratch behavior compared to their respective reactive precursors. This improvement is especially significant for the lower M_ns, where the original properties were inferior; and can be attributed to a proportionately higher increase in cohesion during crosslinking.

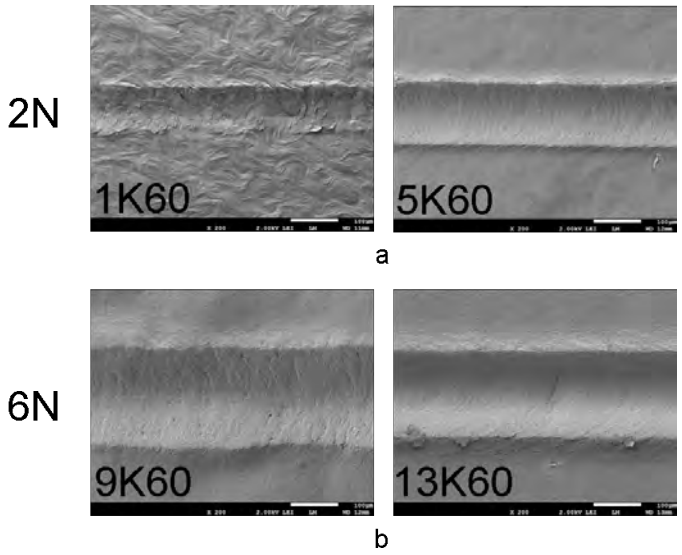

Figure 5.5 – Scratch tracks after curing of (a) 1000 and 5000 $\frac{g}{mol}$ LCT coating with a thickness of approximately 45 µm under a constant load of 2 N, and (b) 9000 and 13000 $\frac{g}{mol}$ LCT coating with a thickness of approximately 90 µm under a constant load of 6 N (scale-bar = 100 µm).

5.4.4 Scratch resistance and interface properties

Progressive scratch tests were performed to provide information about the effects of M_n on the overall scratch behavior and interface properties. Experiments were performed on 1000, 5000, 9000, and 13000 $\frac{g}{mol}$ LCT coatings before and after curing 1 h at 370 ^{o}C, and also on the non-end-capped reference sample. The tests consisted of an 8 mm long scratch, with a linearly increasing load from 0.04 to 30 N. As an example, Fig. 5.6 shows SEM images of the scratch paths on the 1000 and the 9000 $\frac{g}{mol}$ LCT coatings before and after curing.

5.4.4.1 Fractographic analysis

Fig. 5.6 shows that the M_n has an important effect on the fracture behavior under sliding conditions. In order to rationalize the scratch behavior and provide more understanding of the changes induced by the M_n of the oligomer, we will discuss the important features present in each sample.

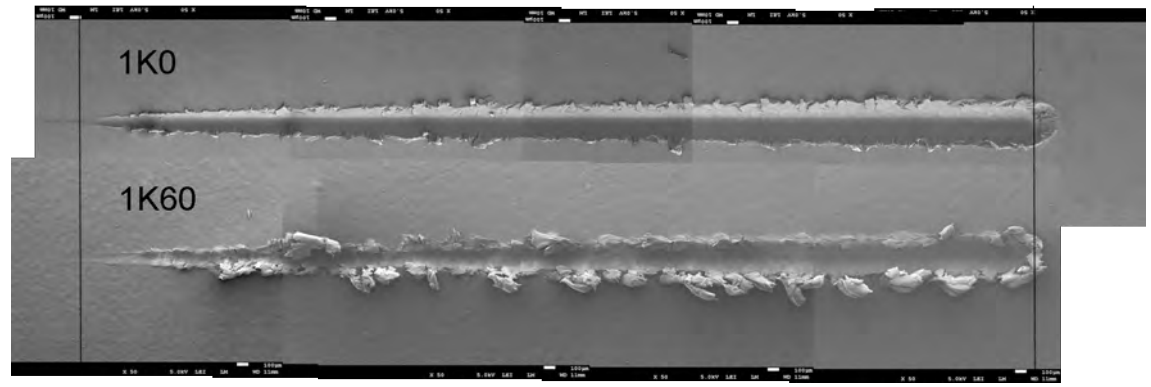

(a)

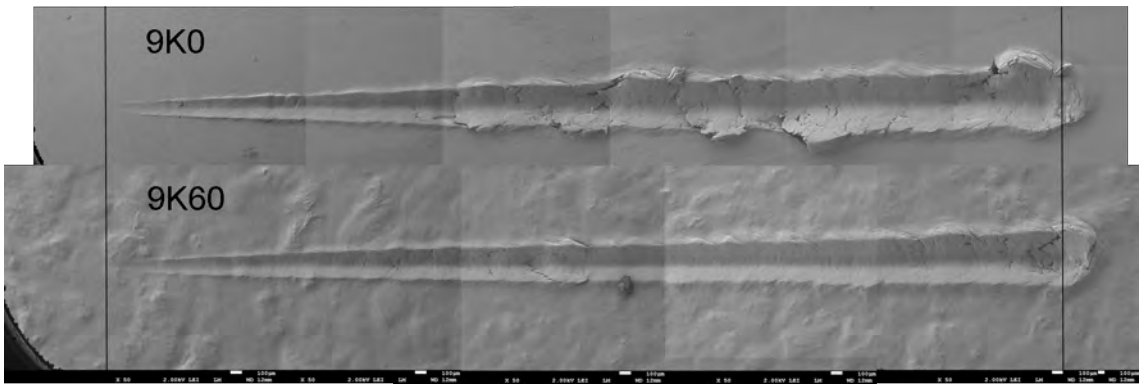

(b)

Figure 5.6 – SEM images of progressive load scratch paths on 1000 (a) and 9000 (b) $\frac{g}{mol}$ LCTs before and after curing. The load was linearly increased from 0.04 to 30 N over a scratch length of 8 mm.

The 1000 $\frac{g}{mol}$ reactive LCT coating showed a soft and weak behavior, and was removed by the indenter. The surface showed neither microcracks nor tensile cracking along the scratch path (Fig. 5.7). There are also, as in the 5000 $\frac{g}{mol}$ reactive LCT, no fibrils present on the fracture surfaces. This indicates an extremely low cohesive strength of the polymer, which is expected due to the poor properties of low M_n reactive oligomers.

After the 1000 $\frac{g}{mol}$ LCT is cured, the surface shows the formation of clusters or bundles (Fig. 5.8 a). It was observed that very early cracks formed along the interfaces of these "domains" during the scratch test. This observation seems to indicate that the domain interfaces are weak. As a result of the increased cohesion of the material, the failures at the domain interfaces can propagate through the thickness of the coating, and accelerate substrate exposure compared to the reactive oligomer.

On the other hand, it was also observed that, after curing, the substrate exposure along the scratch path is reduced (Fig. 5.8 b). In addition, fracture surfaces show a very fine, highly fibrillar structure (Fig. 5.8 c). Due to the developed fibrillar

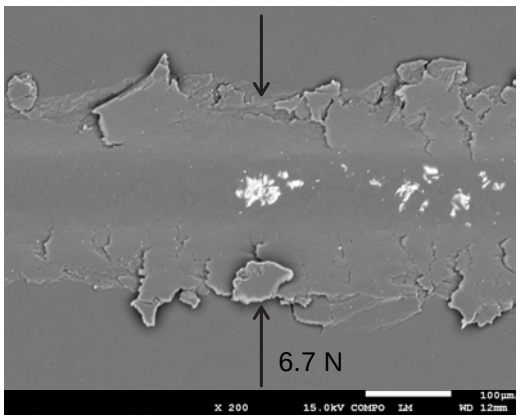

Figure 5.7 – Back-scatering SEM image of the a section of the progressive scratch on a 1000 $\frac{g}{mol}$ reactive oligomer. The arrows indicate the initial exposure of the aluminum substrate during testing.

structure, much more energy is required to induce the scratch, which translates into an improved scratch resistance.

The 5000 $\frac{g}{mol}$ LCT was extensively discussed in chapter 4; however, it is illustrative to indicate here how it performs compared to other M_ns. As in the lower M_n LCT, the reactive 5000 $\frac{g}{mol}$ oligomer showed also no fibrillar structure; however, in this case, microcracking appeared. An increase in molecular weight implies an increase in cohesion and elastic behavior (Fig. 5.3 a). Thus, the behavior shifts from plastic deformation and material removal, to a more elasto-plastic response. This increased cohesion and elastic behavior allow the development of tensile stresses behind the tip, which may cause the initiation and propagation of cracks (see Fig. 4.10).

The 9000 $\frac{g}{mol}$ reactive oligomer already shows a highly fibrillar structure prior to curing (Fig. 5.9). This molecular length provides, therefore, certain strength to the reactive oligomer. The scratch path shows an "amorphous" damage, with numerous cracks along the scratch and on the sides. There is, however, a complete absence of substrate exposure on the 9000 $\frac{g}{mol}$ reactive oligomer coating with the average thickness of 90 µm (Fig. 5.10). This observation will become more relevant later on, during the analysis of the 13000 $\frac{g}{mol}$ LCT coating with similar thickness.

After curing the 9000 $\frac{g}{mol}$ LCTs, the frequency of coating failures is greatly reduced. Moreover, although cracks might have reached the substrate, back-scattering images (Fig. 5.11) show again that there is no visible substrate exposure, even at a load of 30 N. In this case, curing has, in fact, improved scratch resistance and reduced cracks.

The 13000 $\frac{g}{mol}$ reactive oligomer shows a fibrillar fracture behavior, as the reactive 9000 $\frac{g}{mol}$ LCT; and microcracking onsets at a slightly higher normal load. Observations also indicate interfacial failures (Fig. 5.12). This increased failure at the interface could be induced either by increased mechanical properties (an increase in cohesive strength would shift the failure towards the interface) or by a weakening of the adhesion strength. Since the average thickness of the cured 9000 $\frac{g}{mol}$ and the re-

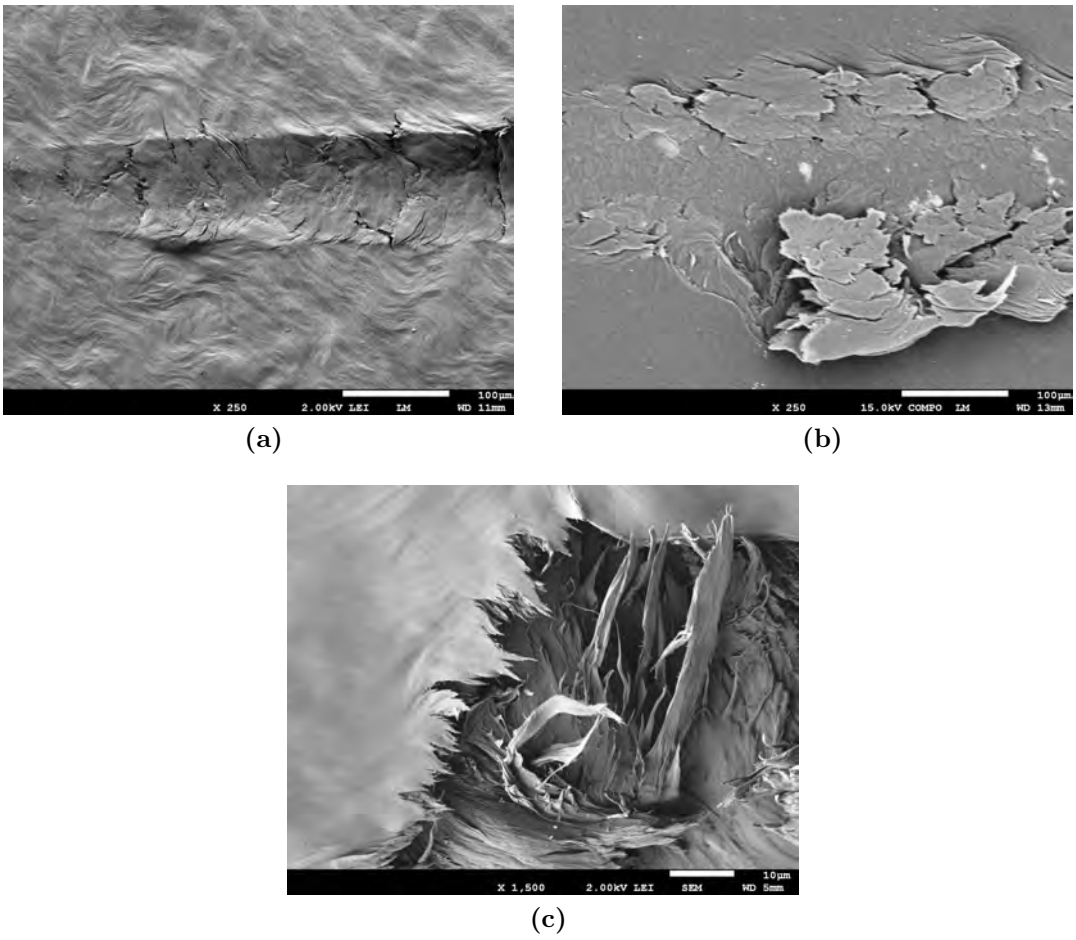

(a) **(b)**

(c)

Figure 5.8 – SEM images of (a) the initial scratch path originated on a cured 1000 $\frac{g}{mol}$ LCT under a progressive load scratch test; (b) back-scatering SEM image of the scratch path sowing the initiation of substrate exposure; and (c) detail of the fibrillar fracture surface of a cured 1000 $\frac{g}{mol}$ LCT

active 13000 $\frac{g}{mol}$ LCTs were equivalent, one can compare the E, H, ER and fracture surfaces of these two samples. As previously indicated, the mechanical behavior of the reactive 13000 $\frac{g}{mol}$ LCT appears to be lower than that of the cured 9000 $\frac{g}{mol}$; therefore, the interfacial failure could be attributed to a weakening of the adhesive strength compared to lower M_n LCTs.

Curing the 13000 $\frac{g}{mol}$ LCT oligomer had negligible effects on the fibrillar structure and initiation of microcracking. This lesser effect of curing can be explained by the lower mobility of the longer polymer backbones, and the lower concentration of reactive groups. On the other hand, the curing process accelerated and increased interfacial failure. Fig. 5.13 shows an interfacial failure of a cured 13000 $\frac{g}{mol}$ LCT on a grit-blasted aluminum substrate. After curing, the substrate is exposed at a considerably lower load, with clear adhesive failures. This further shift of failures towards the interface could be attributed to a slight increase in cohesive strength

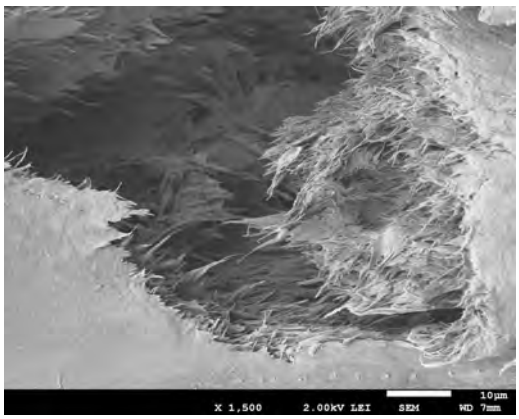

Figure 5.9 – Detail of the fibrillar structure developed on the fracture surface of a 9000 $\frac{g}{mol}$ reactive LCT during a progressive scratch test

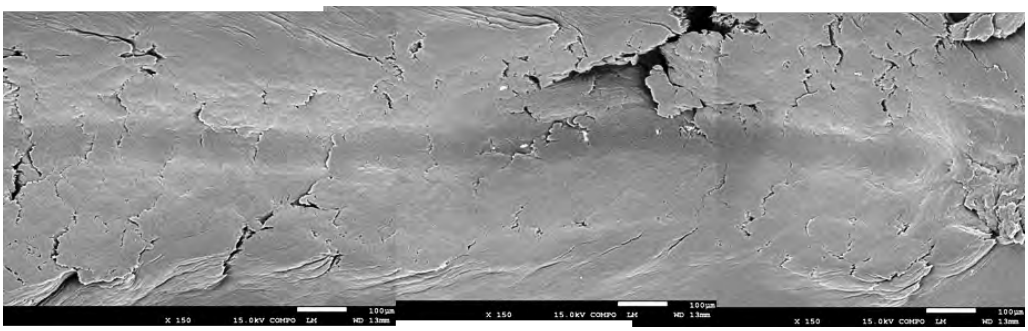

Figure 5.10 – Back-scatering SEM image of the scratch path showing the absence of visible substrate exposure on the reactive 9000 $\frac{g}{mol}$ LCT coating after a progressive scratching with a final load of 30 N

of the cured 13000 $\frac{g}{mol}$ LCTs. Another possibility is that the curing may have, as well, decreased the interfacial properties due to the occurrence of reactions or the development of residual stresses at the interface, as observed in other polymeric coating systems [134]. Further research would be necessary to identify the exact mechanism. Nevertheless, these results show a reduction in adhesion compared to the 9000 $\frac{g}{mol}$, were no interfacial failures where observed, and a subsequent reduction in scratch resistance. Furthermore, these observations support the relation between end-groups concentration and adhesion.

The non-end-capped reference sample posses a M_n of approximately 30000 $\frac{g}{mol}$, and is equivalent to the commercial LCP Vectra® A950. In these coatings, microcracking started at about the same normal load as in the cured 9000 $\frac{g}{mol}$ LCT; and the morphology of the fibrillar fractures (Fig. 5.14 a) were equivalent to those observed by several researchers on the commercial Vectra® [26].

These coatings also showed a particular failure mode, which consisted in cracks parallel to the scratch direction (Fig. 5.14 b). Some literature refer to this type of failure as median cracks [135], which are likely to form in front or under the

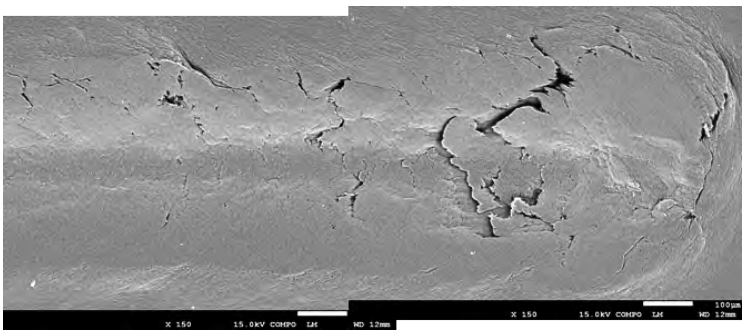

Figure 5.11 – Back-scatering SEM image of the scratch path sowing the absence of visible substrate exposure on the cured 9000 $\frac{g}{mol}$ LCT coating after a progressive scratching with a final load of 30 N

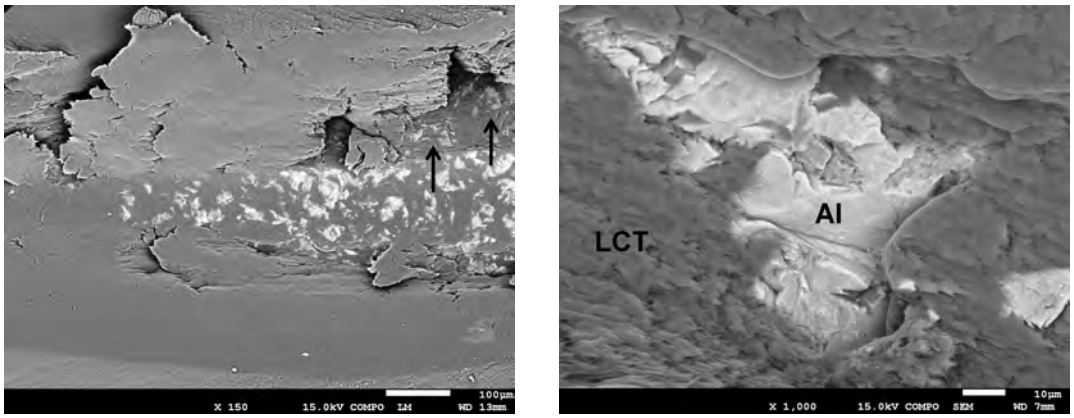

(a) **(b)**

Figure 5.12 – (a) Back-scatering SEM image of the scratch path sowing the initiation of substrate exposure on a 13000 $\frac{g}{mol}$ LCT oligomer (i. e., non-cured) during a progressive scratch test (the lateral interfacial spallation is indicated); and (b) detail of the interfacial spallation

moving indenter, and not due to stresses behind the tip, like tensile cracking. As the load increases, these cracks develop into a cohesive failure that leads to loss of material. Since these cracks propagate along the scratch direction, the material loss is contained within the scratch track. The substrate was not visibly exposed during the scratch test, probably due to the 25 % larger thickness of these coatings (compared to the 9000 and 13000 $\frac{g}{mol}$ LCTs) and the particular failure mode that it developed.

In summary, the scratch analysis showed that as the molecular weight of the oligomer increased, low-load failures (which are less dependent on coating thickness) onset at higher loads and showed a more fibrillar structure. This indicates an increase in cohesion. Since the thickness of the coating affects the scratch behavior [136], further analysis of the scratch behavior was limited to groups of samples with equivalent

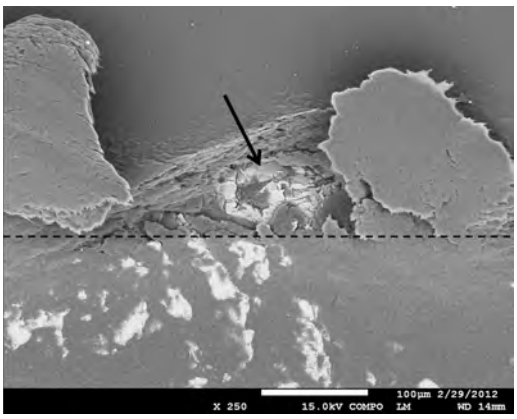

Figure 5.13 – SEM image of an interfacial failure in a 13000 $\frac{g}{mol}$ LCT coating cured 1 h at 370 °C. The arrow indicates an interfacial lateral spallation.

thickness. One of the main observations during these analyses was that as the M_n increased, the coating-substrate interface properties decreased, and failures shifted towards the interface. Further results related the lower concentration of polar end-groups to this decrease in adhesion.

5.4.4.2 Acoustic emissions

During the progressive load scratch tests, the acoustic emissions (AE) were also recorded. The analysis of individual coatings with similar thicknesses indicated that an increase in the M_n of the oligomer increases the AE. At the same time, curing increases the intensity of the acoustic emissions, and accelerates its onset, especially at low M_n (Fig. 5.15). These results show a direct correlation between the polymer strength and the AE.

All in all, it was observed that an increase in cohesion or strength accelerates the onset of both, the polymer failures and the AE. Therefore, the occurrence of AE is related to adhesive and cohesive failures of the coating. A further correlation across all M_ns between the AE and fracture modes using the current set of samples was limited by rough grit-blasted surface and coating thickness variations.

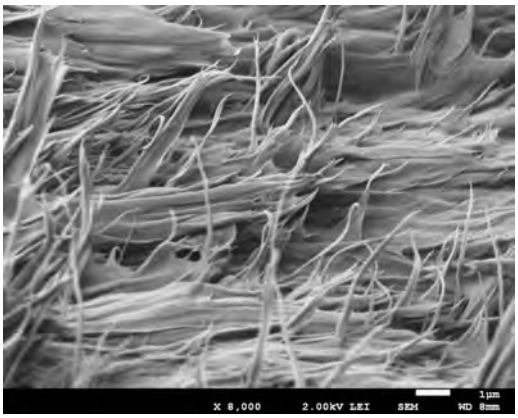

(a)

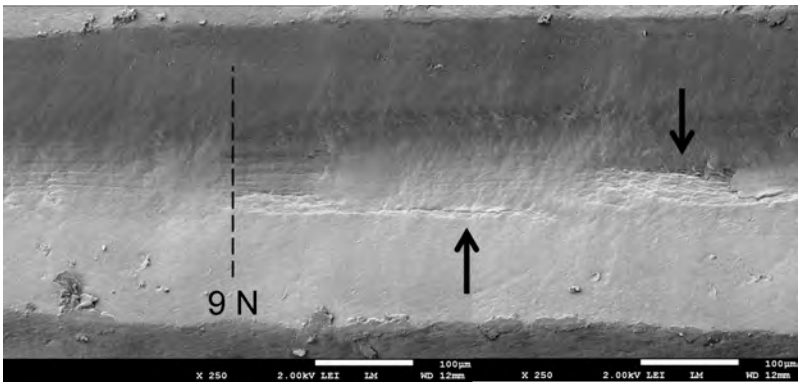

(b)

Figure 5.14 – Fibrillar fracture (a) and median cracks (b) (indicated by the arrows) in a non-end-capped LCP developed during the progressive scratch test

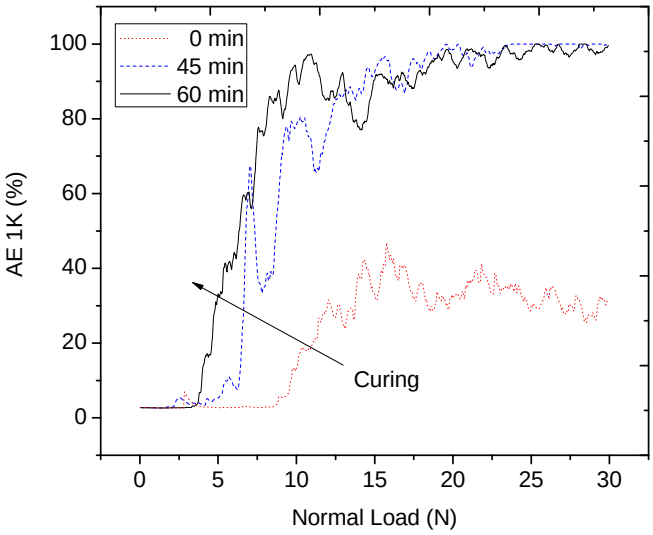

(a)

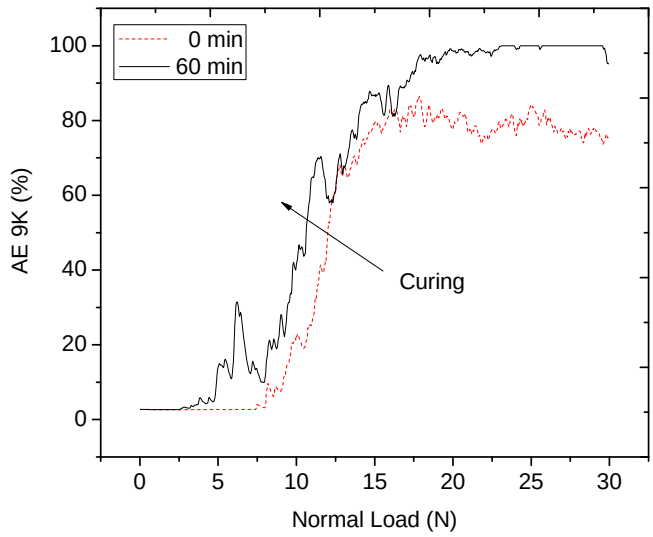

(b)

Figure 5.15 – Acoustic emissions recorded during the progressive scratch testing of a 1000 (a) and 9000 (b) $\frac{g}{mol}$ LCT before and after curing 1 h at 370 °C

5.5 Conclusions

The molecular weight (M_n) of the precursor liquid crystalline thermoset (LCT) has a major effect on the final properties of the coatings. In this Chapter, the effect of the M_n of the reactive oligomers on the surface, mechanical, and adhesion properties of the LCT coatings was analyzed.

It was observed that an increase in M_n induces a coarser and more irregular roughening of the coating surfaces. This phenomenon may be related to the mobility of the molecules, which, together with the observed formation of fibrillar microstructures, supports the explanation of the roughening as an agglomeration or aggregation of the rigid rods. This behavior implies that higher M_ns posses less aggregate-aggregate interfaces, which has consequences on the scratch behavior.

Low M_n allows higher chain packing, and the initial properties at the nanoscale are higher; however, the liquid crystalline networks distort more during crosslinking and properties decrease. High M_n oligomers have lower initial nanomechanical properties. Although these properties increase with curing, the increase is very limited by the lower chain mobility and concentration of end-groups. As a result, the properties of all cured products tend to converge to a specific value slightly higher than that of the thermoplastic.

At the microscale, the cohesive strength and elasticity of the reactive material increase with the M_n. Consequently, the mechanical properties are initially very low for the lowest M_n LCT; but they increase during curing to match the values of the high-M_n counterparts. As the M_n increases, however, the effect of curing is highly restricted, and the changes in mechanical properties appeared to be very limited.

The scratch resistance also increases with the M_n of the oligomer, and a higher M_n delays the onset of failures. On the other hand, as the M_n increases, adhesion decreases. This decrement in adhesion with the M_n was related to a reduction in surface activity due to a lower concentration of the phenylethynyl end-groups.

6 Effect of Temperature and Molecular Orientation

6.1 Summary

This chapter investigated the effects of temperature and macroscopic molecular alignment on the mechanical properties of the coating. The elastic modulus and hardness of an LCT coating were measured at various temperatures ranging from -35 to 160 ºC; and the scratch behavior of uniaxially oriented coatings was analyzed.

The reactive LCT showed a mechanical behavior with increasing temperature equivalent to that of the thermoplastic Vectra®. In addition, the crosslinkable chemistry appears to improve the LCT performance at high temperatures, with respect to the thermoplastic. The mechanical response and scratch behavior of macroscopically oriented coatings was found to be highly anisotropic, with superior elastic recovery and scratch resistance in a direction perpendicular to the molecules.

6.2 Introduction

In aircraft applications, coatings are exposed to a wide range of temperatures. For instance, it was mentioned in Chapter 2 that subsonic aircraft are usually designed to operate from -55 to +80 ºC [28]. Therefore, not only the mechanical, but also the thermal properties of the coatings are critical. In previous studies, the storage modulus of a cured 5000 $\frac{g}{mol}$ LCT was reported to decrease by one order of magnitude (from approximately 5 to 0.5 GPa), when the temperature increases from 0 to 160 ºC [27]. This was, however, determined using dynamic mechanical thermal analysis (DMTA) of free standing films. These films were cured under different conditions compared to those of melt-pressed coatings; and the final results can be expected to differ. It is, therefore, relevant to investigate the mechanical behavior of these coatings within a wide temperature range.

LCP domains can also be aligned with respect to each other. This macroscopic alignment of LCT offers the possibility to tune mechanical properties and expand the potential applications of the coating. Several methods could be used to align the domain directors, such as magnetic fields [137–139] and shear stresses (which usually

occur during processing) [140–144]. The resulting properties along the alignment direction are considerably higher; however, the product becomes highly anisotropic. Typical examples of oriented LCPs are extruded Vectra® films, and spun Kevlar® fibers. Despite the extensive research on oriented LCP films and fibers, the literature on oriented LCP coatings is, to the best of our knowledge, inexistent.

The purpose of the present chapter is, first, to investigate the mechanical behavior of the coatings within the wide temperature range of potential operating conditions, by in-situ evaluation of the properties. And second, to investigate the effects of macroscopic alignment of the LCT coatings on the mechanical behavior.

This chapter is divided into two parts. In the first section, the nanomechanical behavior of the LCT coatings is studied by in-situ measurement of properties at various temperatures. The performance of the LCTs is then compared to that of the thermoplastic Vectra®. The second section analyzes the scratch behavior and failure of oriented coatings in a direction parallel and perpendicular to aligned molecules, in order to investigate the anisotropic response.

6.3 Materials and characterization

For the present work, a 5000 $\frac{g}{mol}$ LCT was synthesized and melt-pressed onto a grit-blasted (GB) AA5083-H111 aluminum substrate, as described in Chapter 3. The samples were subsequently cured for 60 min at 350 ºC or 370 ºC. Coatings with the commercial LCP Vectra® A950 (Ticona GmbH, Kelsterbach, Germany) were also prepared. Additionally, a uniaxially oriented 9000 $\frac{g}{mol}$ LCT coating was prepared as described in Chapter 3 sec. 3.3.2, and cured for 60 min at 370 ºC. The oriented coating was approximately 35 µm thick.

For in-situ measurement of the elastic modulus (E) and hardness (H) at various temperatures ranging from -35 to +160 ºC, a temperature-controlled stage holder was coupled to the nanoindentation system. Typically, 10 indents were obtained for individual specimens. Oliver and Pharr's method [107] was used to analyze the unloading section of the load-displacement curves, and average values were calculated. The elastic recovery (ER) and scratch behavior was investigated using a microscratch tester equipped with a 100 µm radius Rockwell tip. The oriented LCT coating was scratched with constant normal loads of 1 and 2 N, and a load linearly increasing from 0.04 to 30 N. The tests consisted of 10 mm long scratch paths, both parallel and perpendicular to the molecular orientation. The analysis of surface failures was performed by post facto observation of the scratch tracks using scanning electron microscopy (SEM).

6.4 Results and discussion

6.4.1 Effect of temperature on the mechanical behavior of the coatings

The E and H of a 5000 $\frac{g}{mol}$ LCT coating were measured in-situ, before and after curing, at various temperatures ranging from -35 to 160 ºC. The results are presented in Fig. 6.1 and Fig. 6.2. The average values obtained for the thermoplastic Vectra® A950 coating are also indicated.

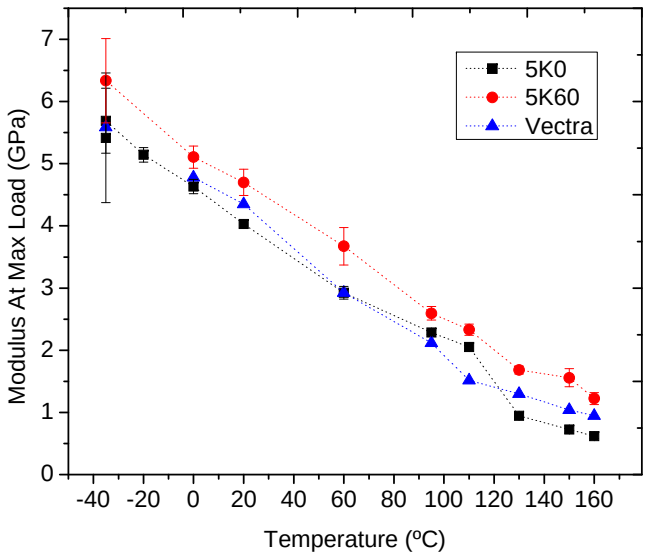

Figure 6.1 – Nanoindentation-measured elastic modulus of the coating at various temperatures from -35 to 160 ºC

At -35 ºC, there is a high dispersion of E and H (Fig. 6.1 and Fig. 6.2) possibly due to ice formation or operation close to the limit temperature of the equipment. Despite this high dispersion, the calculated average values are in line with measurements at higher temperatures.

The E of the reactive oligomer (5K0) was found to decrease linearly as the temperature increases (Fig. 6.1). At a temperature above 110 ºC, a sudden drop of the property occurs. This drop can be understood as a softening of the reactive oligomer at temperatures above the T_g, in agreement with previous dynamic mechanical analysis measurements (DMTA) [27, 70, 118]. The delay in the onset of the drop, with respect to the T_g of the coatings (which is approximately 100 ºC, as determined by DSC, see Fig. 4.1) can be attributed to both the dependence of T_g on the measurement technique and the thermal gradient along the sample and the adhesive (Fig. 3.13).

Curing (sample 5K60) increased the measured E with respect to the reactive oligomer, while the rate of the decrease with increasing temperature was not affected. On the

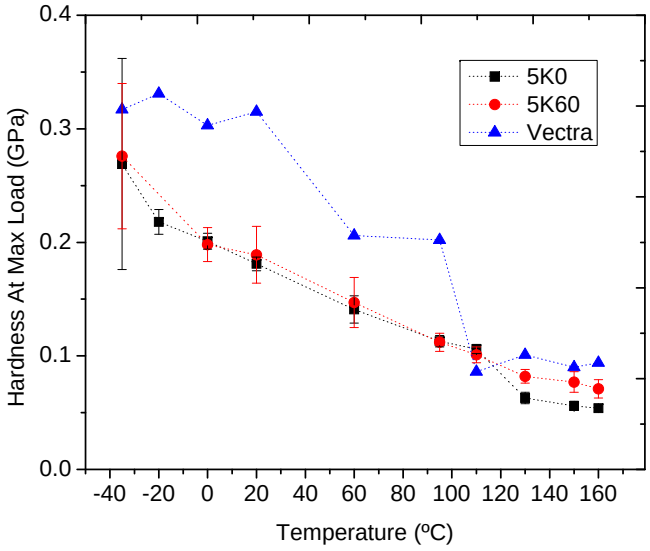

Figure 6.2 – Nanoindentation-measured hardness of the coating at various temperatures from -35 to 160 ºC

other hand, the drop in E at temperatures above the T_g is negligible. This was expected since curing increases the T_g of the polymer, and reduces the softening of the material above this temperature.

The nanoindentation measured E of the thermoplastic Vectra® A950 coatings shows an equivalent rate of decrease with increasing temperature (Fig. 6.1). This linear decrease is in agreement with the previously reported behavior for the tensile modulus of injection-molded Vectra® [24]. The drop in the curve at the T_g (which ranges from 90 to 110 ºC, depending on the characterization technique used [145, 146]) was also observed [24]. The decrease in E is, however, slightly less pronounced than for the reactive oligomer. In addition, as shown in previous chapters, the E of Vectra® coatings at room temperature are lower than that of cured LCTs. The results presented in Fig. 6.1 showed that this observation remains valid along the studied range of temperatures, since the decrease rate for Vectra® is equivalent to that of the LCTs.

The evolution of the H of the reactive oligomer with increasing temperature shows the same behavior as the E (Fig. 6.2). Curing, however, induces no further increase in this property, which is expected due to observations presented in Chapter 4. On the other hand, curing reduces the softening of the material, and the subsequent drop in the H. As a consequence, at temperatures above the T_g, the hardness of cured coatings is higher than that of the reactive oligomer.

The Fig. 6.2 also shows that the hardness of Vectra® A950 coatings, as measured by traditional load-controlled nanoindentation (i. e., not using the CSM method), is superior to that of LCTs within the range of temperatures studied. The reduction in H above the T_g is, however, larger for Vectra® than for the LCT counterparts.

As a result, the advantage of the thermoplastic Vectra®, with respect to hardness, appears to diminish considerably at high temperatures.

6.4.2 Effect of molecular orientation on the mechanical response of LCT coatings

The molecular alignment of uniaxially oriented melt-pressed samples (as described in sec. 3.3.2) was not quantified, and a small but measurable drop in the order parameter is expected during the curing process [118]. Nevertheless, experiments showed that the cured samples retained a certain degree of macroscopic alignment. In previous chapters, the surface morphology developed during the crosslinking was related to the molecular orientation. Therefore, the alignment of the polymer backbones should be detectable on the surface morphology. As expected, creases parallel to the shear direction revealed the local molecular orientation, which appears sinuous but generally along the flow path.

In order to investigate the anisotropic behavior, the oriented LCT coating was scratched in a direction longitudinal and perpendicular to the oriented molecules. Fig. 6.3 shows the elastic recovery (ER), calculated as described in Chapter 3, after scratching at a constant load of 1 N. It can be observed that during a scratch along the molecular direction, the ER is approximately 70 % of the total deformation. On the other hand, after a scratch across the direction of the molecules, the ER increases to 90 %. As a reference, Fig. 6.3 also includes the ER for a non-oriented 9000 $\frac{g}{mol}$ coating. It is interesting to remark that the ER for this sample was observed to be approximately 80 %, averaging of the values for the oriented sample.

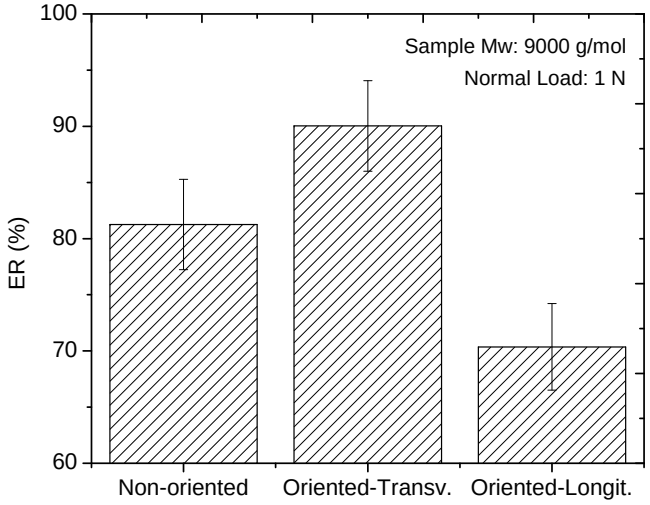

Figure 6.3 – Elastic recovery (ER) measured immediately after scratching a non-oriented 9000 $\frac{g}{mol}$ LCT, and a uniaxialy oriented coating scratched in a direction transversal and longitudinal respect to the molecular orientation

The fracture morphology developed during microscratching also presents important differences depending on the scratching direction. After scratching at a constant load of 2 N (Fig. 6.4), it can be observed that failures tend to occur along the molecular direction. During the scratching perpendicular to the main molecular orientation, the isolated stress concentration at the tip of the indenter can easily cause a puncture of the polymer surface and eventual entanglement of the indenter with the polymer molecules. As a consequence, the movement of the indenter pulls the molecules in the direction of motion, causing a tear of the material (Fig. 6.4 b).

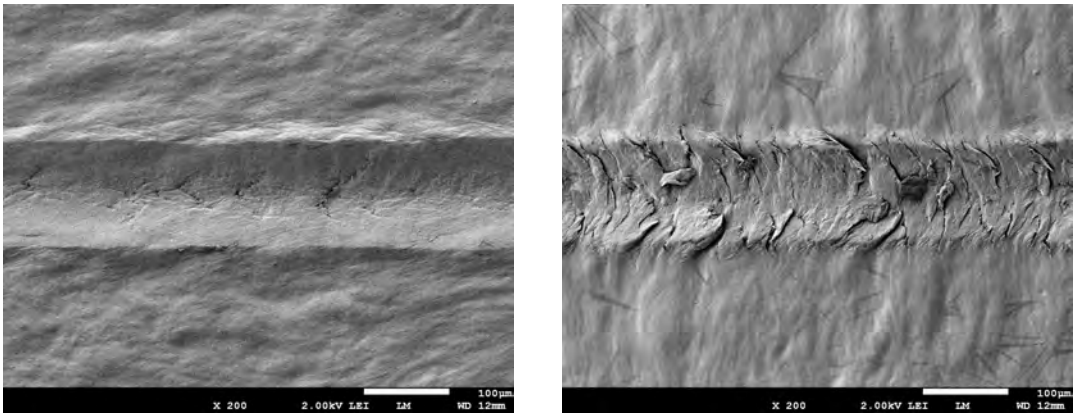

(a) **(b)**

Figure 6.4 – SEM images of surfaces scratched at a constant normal load of 2 N along a path longitudinal (a) and transversal (b) respect to the flow direction

The anisotropy in the scratch behavior is more pronounced as the normal load increases. During the progressive scratching parallel to the molecules, cracks can easily propagate along the scratch direction. As a consequence, the coating delaminates. Material piles-up in front of the indenter, and the delamination progressively extends outside the scratch path (Fig. 6.5 a). On the fracture surfaces, fibrils approximately 10 nm thick are revealed. Hudson [37] has confirmed using electron diffraction patterns that the molecular axis is along the polymer fibril and perpendicular to the lamellae.

On the contrary, when scratching perpendicular to the orientation of the molecules (Fig. 6.5 b), the scratch path forms through pulling and cutting of the back-bones. Although it was not possible to measure the stresses along the scratch direction during the progressive test, it is known that fracture parallel to the polymer chain direction is easier than perpendicular to it [26]. Scratching perpendicular to the molecules is, therefore, expected to require more energy, resulting in a superior scratch resistance along this direction.

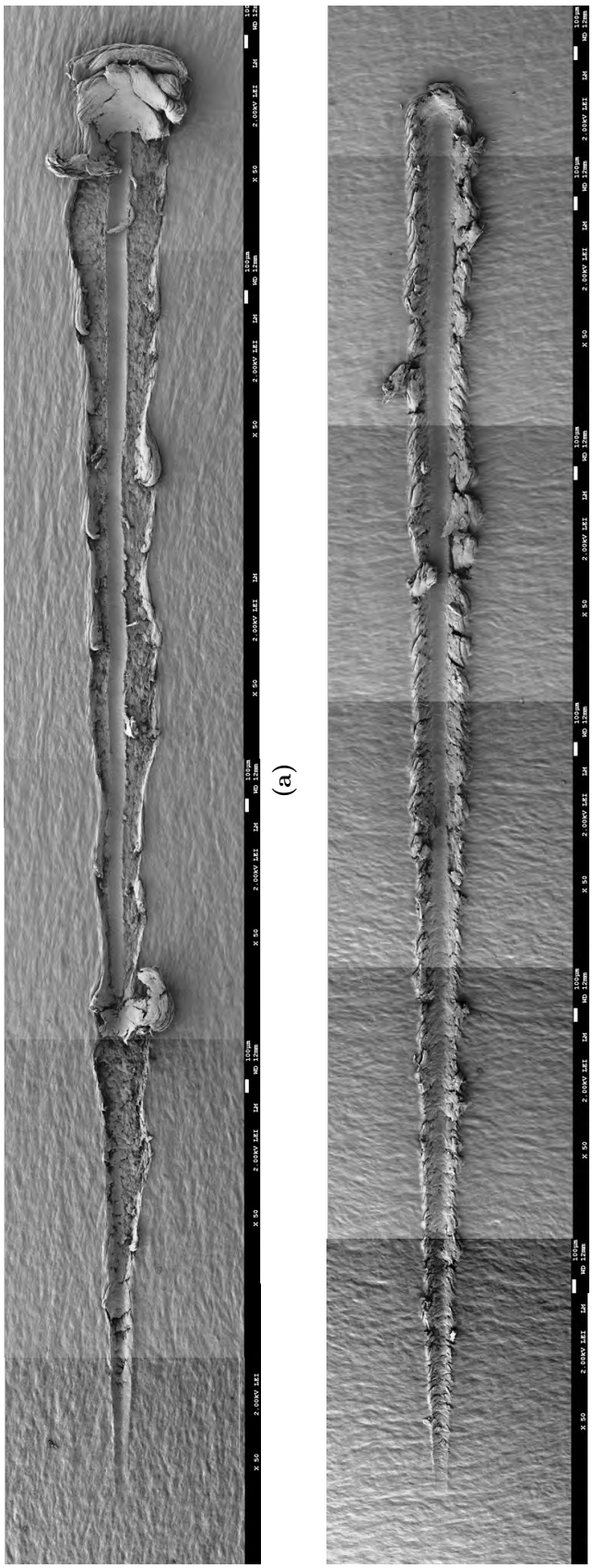

Figure 6.5 – SEM image of the progressive scratch test parallel (a) and perpendicular (b) to the molecular orientation of the polymer. The load was linearly increased from 0.04 to 30 N along a 10 mm long scratch path.

6.5 Conclusions

Both the LCT and Vectra® A950 coatings showed an equivalent linear decrease in the nanoindentation measured E and H with increasing temperature. A drop in the properties of Vectra® and the reactive LCT was observed above the T_g. Curing of the LCT, however, reduced or eliminated the drop in mechanical properties above the T_g, improving its performance at high temperatures with respect to the thermoplastic.

Oriented LCT coatings were found to be highly anisotropic. During scratching, non-oriented samples showed an elastic behavior intermediate between the response along and perpendicular to the molecular direction in oriented samples. The mechanical failures of the coatings tended to occur along the orientation direction, resulting in a decreased scratch resistance in that direction. All in all, the macroscopic orientation of the LCT coatings, which was previously related to the surface morphology of the coating, is retained after curing. Depending on the application, this anisotropy should be avoided. On the other hand, the capability of these polymers to retain a certain degree of macroscopic alignment during curing allows the tuning of properties, widening the range of potential applications of these coating systems.

7 Adhesion and Environmental Resistance of LCTs on Aluminum

7.1 Summary

The adhesion of the LCTs was evaluated and compared to that of their commercial LCP counterparts, using pull-off and microscratch testing. In addition, the resistance to different environments relevant for aircraft applications was studied using salt-fog spray, climatic-test cabinets, and full-immersion testing. Among the various pre-treatments investigated, only phosphoric-acid anodization (PAA) appeared to shift lateral spallation failure from adhesive to cohesive on both coating materials. In the case of LCT coatings on GB aluminum, samples failed cohesively, leaving a thick, remnant layer on the substrate. This suggests that GB is the most beneficial pretreatment to improve the adhesion of LCT coatings under sliding conditions. The LCT and Vectra® A950 coatings showed equivalent environmental resistance, with no swelling, peeling, or blistering after exposure to the selected environments. All in all, the reactive groups and their cured products did not appear to degrade the environmental resistance of the polymer. Results, however, suggest that exposed coating-substrate interfaces constitute paths for environmental attack.

7.2 Introduction

One of the most critical properties of a coating is its adhesion; and there is a wide variety of techniques and procedures to assess this property. The origin of such variety lays in the wide variation in coating properties such as flexibility, hardness, application process, substrate material, and adhesion.

One of the most widely known adhesion tests is the pull-off test. Basically, the pull-off test consists of bonding a stud on top of the coating and pulling it off, recording the load required to induce failure. A key requirement to perform this type of test is that the adhesion of the adhesive used to bond the stud to the coating has to be stronger than the adhesion between the substrate and the coating. This is a condition shared by most tests for the evaluation of adhesion of a soft coating on a hard substrate. This requirement becomes a problem when studying coatings with

very high adhesion strength, equivalent to that of the strongest structural adhesives used in aerospace, such as Araldite® 2014/5.

The potential of micro-scratch testing for adhesion assessment was identified since its early developments [136, 147]; and it is now a relatively well established method for the evaluation of adhesion [148, 149]. The main advantages of this method for adhesion evaluation are the minimal sample size and preparation requirements, and that no adhesive is required. In addition, these tests provide repeatability, versatility, and simplicity.

A second important property of a coating is its resistance to the working environment. The characteristic chemical resistance of LCPs is partially attributed to their highly inert surfaces [89, 150, 151] and packed aligned structure [33, 152, 153]. Previous results have demonstrated that the phenylethynyl-reactive groups do not interfere with the mesophase formation [27]. In addition, as discussed in Chapter 5, the adhesion seems to have been improved by the incorporation of the reactive groups in the polymer chemistry. The end-groups, however, affect the surface chemistry and thermal behavior, potentially reducing the chemical resistance. In addition, crosslinking affects the molecular packing of the final product [118, 154] and changes the polymer chemistry, all of which might decrease the permeability and the resistance to the environment.

The present chapter has two purposes. The first aim is to compare the adhesion of the new polymer chemistry with that of the commercial LCP, and determine the effects of various substrate pretreatments. In addition, the present chapter also aims at evaluating the environmental resistance of LCT coatings, from the perspective of the aerospace industry, and comparing it with that of Vectra® coatings.

In the first section, the topic of adhesion is approached, firstly, comparing the LCT and Vectra® coatings using pull-off testing, and addressing the limitations of this method. Then, the thermoset and thermoplastic coatings are compared, and the effects of various surface pretreatments on their adhesion are investigated, by means of scratch testing. The second part of this chapter focuses on the environmental resistance of LCTs applied on GB aluminum. The corrosion resistance of the coatings, the resistance to the combined effect of temperature and moisture, and the chemical resistance to various aviation fluids is investigated and compared with that of the non-end-capped thermoplastic LCP.

7.3 Materials and characterization

7.3.1 Materials and coatings preparation

For the present work, two coating materials were used; a 5000 $\frac{g}{mol}$ LCT, synthesized as described in Chapter 3, and the commercial thermoplastic LCP Vectra® A950. The polymers were melt-pressed on grit-blasted AA5053-H111 aluminum

alloy substrates. Additionally, for the study of adhesion, the coatings were applied on as-received, chromic acid anodized (CAA), and phosphoric acid anodized (PAA) AA5083-H111 aluminum. The various pretreatment methods are described in sec. 3.3. Grit-blasted AA2024-T3 and AA7075-T6 aluminum alloys were also used as substrates for salt-fog spray testing. The LCT coatings were cured 60 min at 370 ^{o}C; and the average thickness of the coatings was approximately 60 µm.

7.3.2 Characterization methods

The adhesion of LCT coatings was compared with that of non-end-capped LCPs using direct tensile testing to measure pull-off strengths, as described in Chapter 3. Five samples were prepared per coating system; and the average failure stress was calculated.

To investigate the adhesion and interface properties of the LCT to the various pretreated AA5083 aluminum substrates and compare it with that of the thermoplastic counterpart Vectra® A950, progressive load microscratch tests were used. The progressive microscratch testing consisted of a linearly increasing load from 0.04 to 30 N along an 8 mm scratch. Typically, three scratches were performed per coating system; and post-mortem fracture surfaces were analyzed by scanning-electron microscopy (SEM).

The environmental resistance of the coatings was evaluated using salt-fog spray, climatic-test cabinets, and full-immersion in various typical aviation fluids, as described in sec. 3.4.5. Five samples per coating system were exposed to the salt-fog spray and hot moisture, and two samples per coating system were used for the immersion tests. After exposure, samples were visually inspected for blistering, peeling, gloss change, and weight gain.

In addition, the lap-shear and pull-off strengths of partially cured coatings were tested before and after exposure to the saline-fog spray, as described in sec. 3.4.4. The press- and thermal- cycles used to prepare the samples for lap-shear testing were identical to those applied for coating manufacture. Five samples were prepared per coating system. The lap-shear and pull-off strengths were calculated by dividing the force (F) by the overlap/contact area, and average failure stresses were calculated. The effect of several of the environmental conditions on the elastic modulus (E) and hardness (H) of the coatings were further investigated using nanoindentation. For the present work, nanoindentations were performed with a scanning probe microscope (SPM, Hysitron, Minneapolis, USA), using a standard Berkovich indenter. A traditional load-controlled mode with a maximum load of 2 mN was selected based on Dub and Trunov [155] (Fig. 3.11). Typically, 9 indents were obtained for individual specimens. Oliver and Pharr's method [107] was used to analyze the unloading section of the nanoindentation load-displacement curves of the LCPs; and average values were calculated.

7.4 Results and discussion

7.4.1 Adhesion and interface behavior of LCT and Vectra® coatings

7.4.1.1 Study of Vectra® and LCT adhesion by pull-off testing

This section initiates the discussion on the topic of adhesion by attempting to compare the pull-off strengths of 5000 $\frac{g}{mol}$ LCT coatings with that of non-end-capped LCP Vectra® A950. Fig. 7.1 shows the pull-off behavior of Vectra® and of two LCT coatings cured at 350 ºC (5K60-350) and 370 ºC (5K60-370), respectively. Due to the higher coating-substrate than coating-adhesive strength, the pull-off test failed to assess the coating-substrate interface. A variety of adhesives and stud surface pretreatments were tested, and it was concluded that to study the coating-substrate interface independently, a different approach was necessary. Nevertheless, valuable observations could be made.

Vectra® coatings failed at the interface between the coating and the adhesive used to bond the stud, while the 5K60-350 samples (which are partially cured LCT coatings [156]) failed cohesively at higher load. Since the surface morphology of both coatings was observed to be equivalent, the higher pull-off strength of the 5K60-350 coatings can be attributed to physical or chemical interactions originated by the modified polymer chemistry. These observations suggest that the phenylethynyl end-groups increased the compatibility with other polymers [157].

The pull-off samples with a fully cured LCT (5K60-370) failed at higher load than the 5K60-350 samples. In this case, the adhesive used to bond the studs failed cohesively at an average stress of 28.7 MPa, in good agreement with the tensile strength of 30 MPa reported by the manufacturer (Huntsman International, LLC). This shows that fully cured LCTs possess, as expected, higher cohesive strength; and it also supports previous results showing the improved adhesion of LCTs compared to commercial LCPs. It is necessary to mention here, however, that the particular surface morphology developed by the 5K60-370 samples (see Fig. 4.3) might have also increased the adhesion at the interface between the coating and the adhesive via mechanical interlocking [158].

7.4.1.2 Study of Vectra® and LCT adhesion by microscratch testing

This section presents the results of using a micro-scratch system for the direct study of the coating-substrate interface behavior, in order to compare the adhesion of the LCT and Vectra® coatings. Additionally, the influence of various substrate pretreatments on their interface behavior and adhesion to aluminum was also investigated.

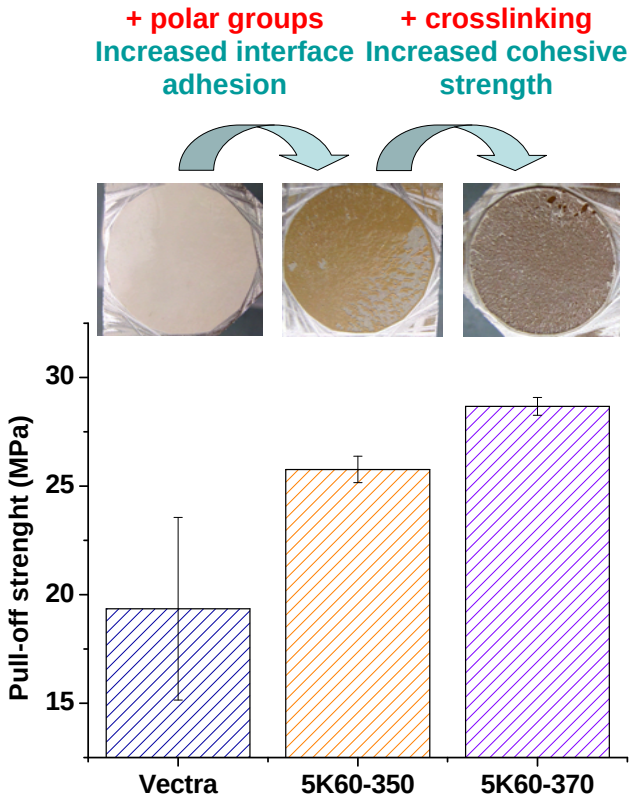

Figure 7.1 – Pull-off strength of 5K60-350, 5K60-370, and Vectra® coatings obtained by direct tensile testing and corresponding macrographs of fracture surfaces

Vectra® A950 adhesion

Vectra® coatings on non-pretreated and chromic-acid anodized aluminum failed adhesively during sample preparation, and scratch tests were not performed. The scratch paths produced during a progressive scratch test on Vectra® coatings applied on grit-blasted (GB) and phosphoric acid anodized (PAA) aluminum are presented in Fig. 7.2. Coatings applied on GB aluminum failed through interfacial spallation, in a similar fashion as cured 13000 $\frac{g}{mol}$ LCTs, although with larger spalled areas (Fig. 7.3 a). This could be understood as a direct consequence of the higher molecular weight and cohesion of Vectra®, which induces the coating peel-off through interfacial failure. The thin PAA layer seems to have increased the adhesion of Vectra®, and a layer of polymer, with large fibrils, was observed to remain attached (Fig. 7.3 b).

A PAA pretreatment on aluminum was also previously observed to provide higher adhesion than GB during lap-shear testing of liquid crystalline polymers. Dietsch [159] reported that in PAA treated samples cohesive failure was observed, while GB samples failed adhesively. The adhesion of polymer films to anodized aluminum is dependent upon whether and how far the polymer penetrates into the micropores of

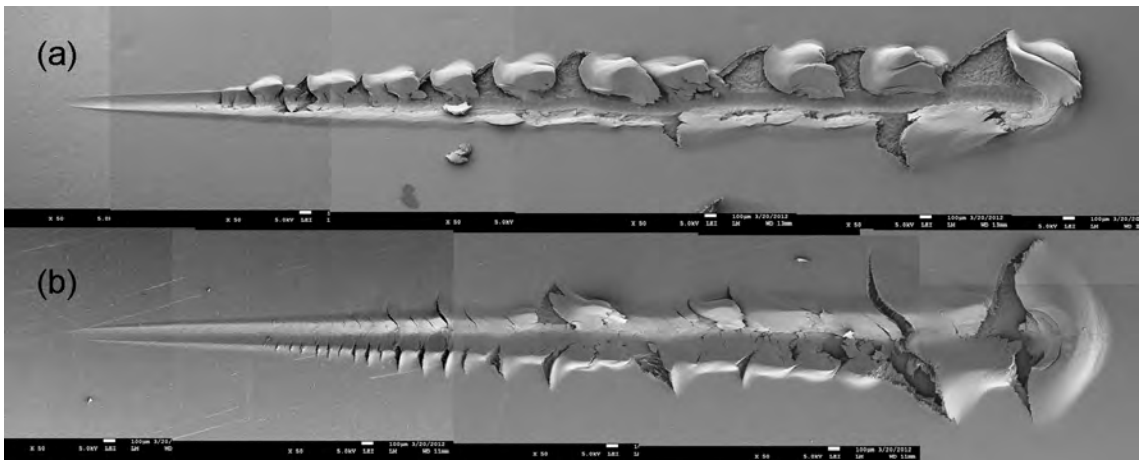

Figure 7.2 – SEM images of the scratch paths produced during the progressive scratch test of Vectra® coatings on GB (a) and PAA pretreated aluminum substrates

the surface and is anchored there [160]. In the case of oxide films produced by phosphoric acid anodizing, there is no obstacle to polymer penetration, which can potentially continue to the base of the pores.

Vectra-type LCT adhesion

Fig. 7.4 shows SEM images of the scratch tracks on cured LCT coatings applied on GB and PAA aluminum; additionally, the LCT was applied on non-pretreated (NP) and chromic acid anodized (CAA) aluminum substrates.

The non-pretreated substrates show low interface properties. Coatings tested before curing show lateral spallation with large interfacial failures (Fig. 7.4 a). Large lateral cracks propagate outside the scratch path, and induce delamination and chip formation. Fig. 7.4 a also shows that the end-of-scratch failure consists of cracks propagating in multiple directions and widespread delamination. These failures occur ahead of the indenter, and are associated with compressive stresses in front of the tip. SEM analysis revealed a remnant polymer layer of several nanometers partially covering the spalled areas (Fig. 7.5). This observation shows that the failure is partly cohesive and suggests that there is a degree of physical or chemical adhesion between the LCT and the aluminum.

On NP samples, curing largely reduced the lateral spallation (Fig. 7.6), indicating that curing the LCT has improved the coating-substrate interaction. The apparent benefit on the interface behavior induced by curing the LCT was previously observed during the analysis of curing time (Chapter 4); however, the precise mechanism was not yet determined.

Despite this apparent improvement in adhesion, extensive interfacial failure occurs; and there is a clear need for a surface pretreatment. The parabolic cracking observed

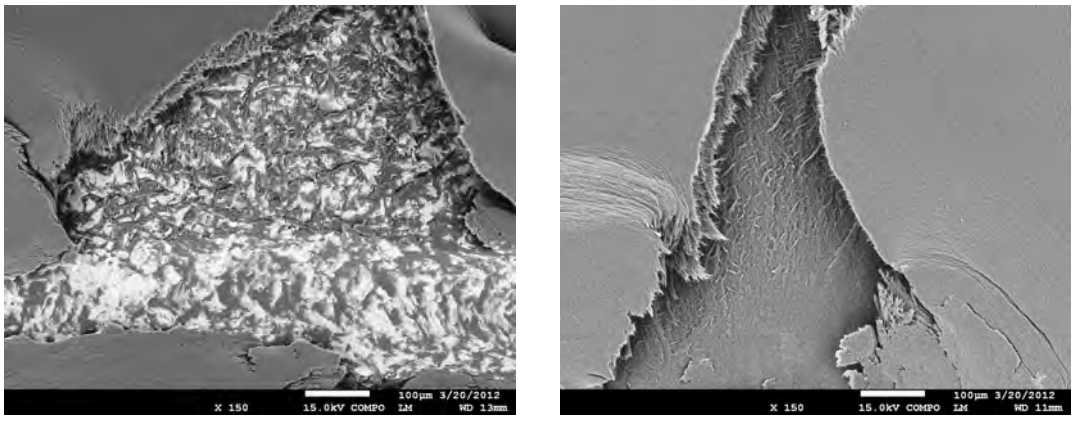

(a) **(b)**

Figure 7.3 – Back-scattering SEM images of interface failures of Vectra® coatings on (a) GB and (b) PAA pretreated aluminum substrates

on NP samples differs from the one previously observed on GB aluminum (Chapter 5 and Chapter 6), which was initiated by the contact stresses with the tip. The low load failures observed on NP samples visibly exposed the substrate at low penetration depths (Fig. 7.7). These failure mechanism can be related to that observed by Borrero-Lopez on brittle coatings [161]. He explains that in brittle coatings on hard substrates under sliding conditions, the lateral cracks seem to initiate at the coating-substrate interface, ahead of the indenter (Fig. 7.8 a), where high stresses are also present. As sliding progresses, he explains, the region under tensile stress behind the tip moves forward, towards a previously originated crack, effectively "sucking" it towards the surface of the film (Fig. 7.8 b). This process results in the crack pattern observed in Fig. 7.7.

The phosphoric acid anodization (PAA) delays the occurrence of the initial failures on cured coatings, and the pretreated substrate is not visibly exposed before the tip reaches the oxide layer. The lateral spallation (outside the scratch path) shifted from adhesive to cohesive failure, indicating an improvement in coating-substrate adhesion (Fig. 7.9). In addition, the morphology at the bottom surfaces of the spalled areas outside the scratch track seems to indicate that the failure in these regions was induced by shear stresses (Fig. 7.9).

Back-scattering SEM of the scratch track of these samples shows that the PAA layer seems to deform under the tip, and remain attached (Fig. 7.10). The light spots along the scratch track in Fig. 7.10 correspond to areas where the PAA oxide layer was removed. Fig. 7.10 also shows that the scratch tip induced delamination of the coating along the borders of the scratch.

The lateral cracking starts at a low angle with respect to the scratch direction, and induces failures with a triangular or trapezoidal shape (Fig. 7.11). Similar failures have been observed, for example, on Pt films on NiO substrates [162–166], and are

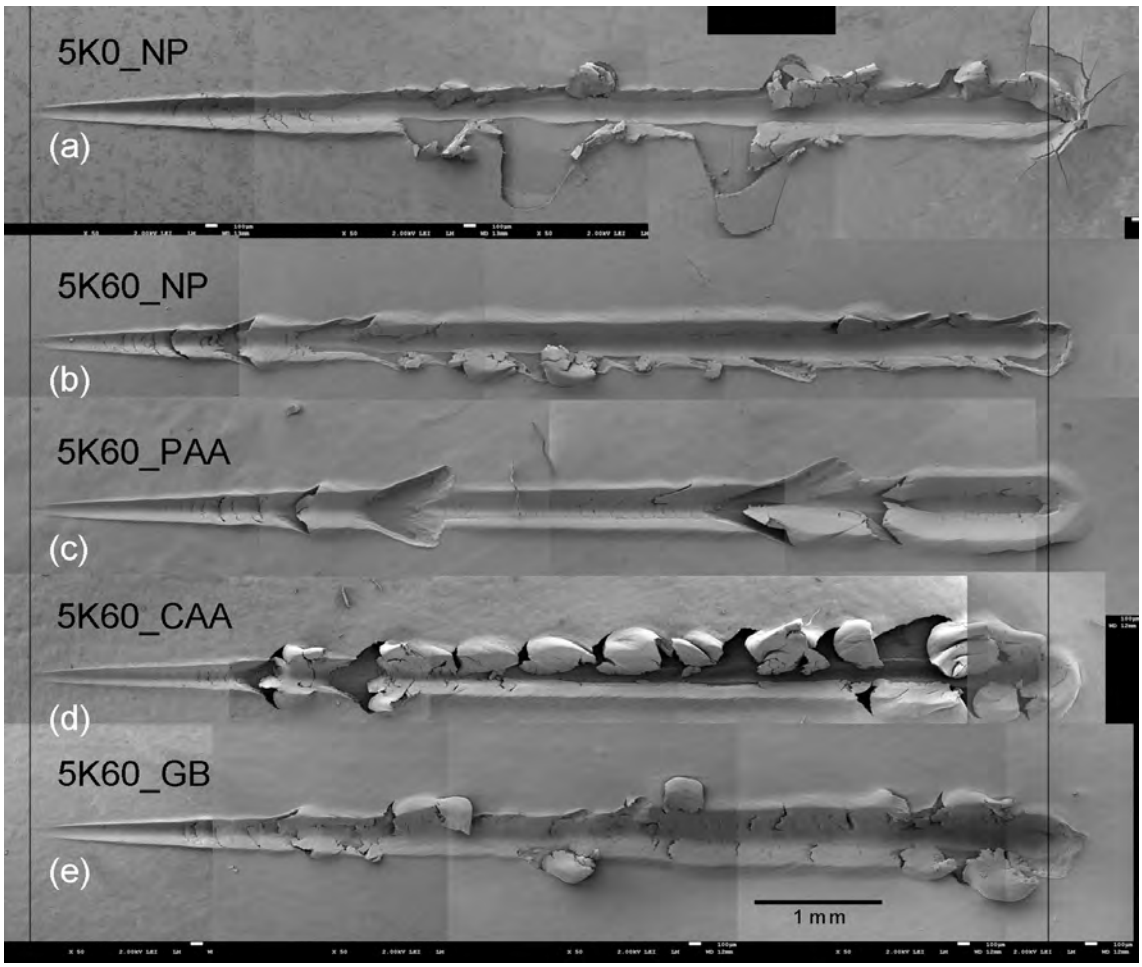

Figure 7.4 – SEM images of the scratch track produced on the LCT applied on aluminum with various pretreatments. The load was linearly increased from 0.04 N to 30 N along an 8 mm scratch path. (5K0 = non-cured LCT; 5K60 = cured LCT; NP = not pretreated; CAA = chromic acid anodization; PAA = phosphoric acid anodization; GB = grit-blasted)

known as trapezoidal delamination (Fig. 7.12). These types of failures are believed to occur ahead of the tip, due to compressive stresses. Therefore, despite the improved adhesion provided by the PAA layer, with respect to NP samples, failure still occurs ahead of the tip, and further improvement is required.

On CAA pretreated samples, cohesive failures started at approximately the same load as in PAA specimens; however, failures that involved the interface with the substrate display a different behavior (Fig. 7.4 d). One can clearly observe a shift from a trapezoidal delamination to a curved fracture propagation, which starts at a higher angle with respect to the scratch direction.

Observations on the CAA samples suggest that, at high loads, there is a delamination of the coating, induced by sub-surface lateral cracking (see Fig. 7.15 a). Sub-surface

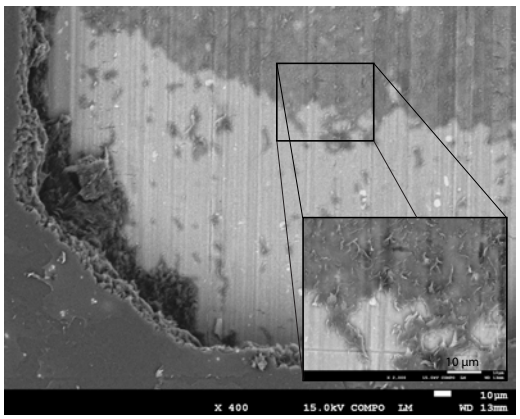

Figure 7.5 – Section of a large lateral spallation induced on the reactive LCT coating on a non-pretreated aluminum substrate. The inset shows a detail of the remnant polymer layer.

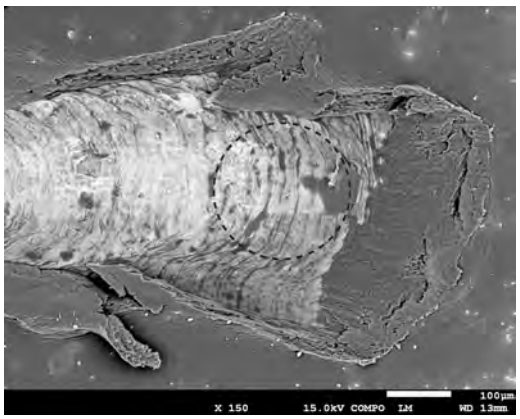

Figure 7.6 – Back-scattering SEM image showing the final failure of a cured LCT coating on a non-pretreated aluminum. The through-coating fracture surfaces are no longer perpendicular to the substrate. The dashed line indicates the ending position of the tip, at the final load of 30 N

lateral cracking (parallel to the surface) is considered to be one of the main cracking types induced by scratching of brittle materials [167–171]. It is believed to occur behind the indenter [168]; and, in the case of brittle coatings, is likely to coincide with the coating-substrate interface [171].

Back-scattering SEM shows that on CAA pretreated samples the failures observed under the tip and in the spalled areas are interfacial, at the coating-CAA interface. The CAA layer remains attached to the aluminum substrate; however, it presents a severe cracking at high scratching loads, and the substrate is visibly exposed (Fig. 7.13). This cracking could be a result of the higher thickness of the CAA oxide layer with respect to the PAA.

When switching from the PAA to the CAA pre-treatment, the failures tend to occur behind the tip. This seems to indicate a further improvement in adhesion with

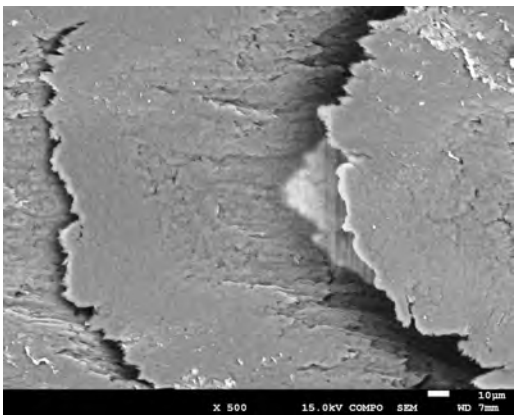

Figure 7.7 – SEM image showing substrate exposure under sliding contact, initiated before the tip reaches the substrate by interfacial failures ahead of the indenter

the CAA pre-treatment; however, failures are interfacial and the substrate is easily exposed.

Finally, the cured LCT coatings on GB aluminum were analyzed. These samples are equivalent to those studied in the two previous chapters; although here, we will focus on its adhesion performance in relation to the NP, CAA, and PAA samples.

We observed that for GB substrates, the initial cohesive failures appear at about the same load as for coatings applied on PAA and CAA pretreated samples. One of the main differences of GB samples with respect to the three previous pretreatments is the shift, at high loads, from interfacial to cohesive failure along the borders of the scratch (Fig. 7.14). This improvement could be mainly attributed to the very rough GB surfaces, which provide mechanical interlocking for the coating layer, improving the adhesion.

On GB samples, instead of delamination of the coating, sub-surface cracks parallel to the substrate propagate through the coating layer (Fig. 7.14). In addition, the absence of cracks or delamination propagating ahead of the tip (Fig. 7.4 e), seems to indicate that the failure tend to occur behind the indenter, as in the case of the CAA samples.

Finally, the formation of wear particles and debris at high loads on GB pretreated coatings was analyzed to gain more insight into the interfacial properties. This formation of the scratch track starts through ductile ploughing in the front of the tip, where the material may experience very high local tensile strains (Fig. 4.10). The tip advances and cuts the material, separating it into the sides. Lateral cracks, parallel to the substrate initiate and propagate (Fig. 7.15 a), which are believed to occur behind the tip [168].

Subsequently, tensile cracks form on the walls of the scratch, either on the sides or behind the tip, as represented in Fig. 7.15 b. As we have previously indicated, this cracking seems to be induced by the tensile stresses originated by the friction between

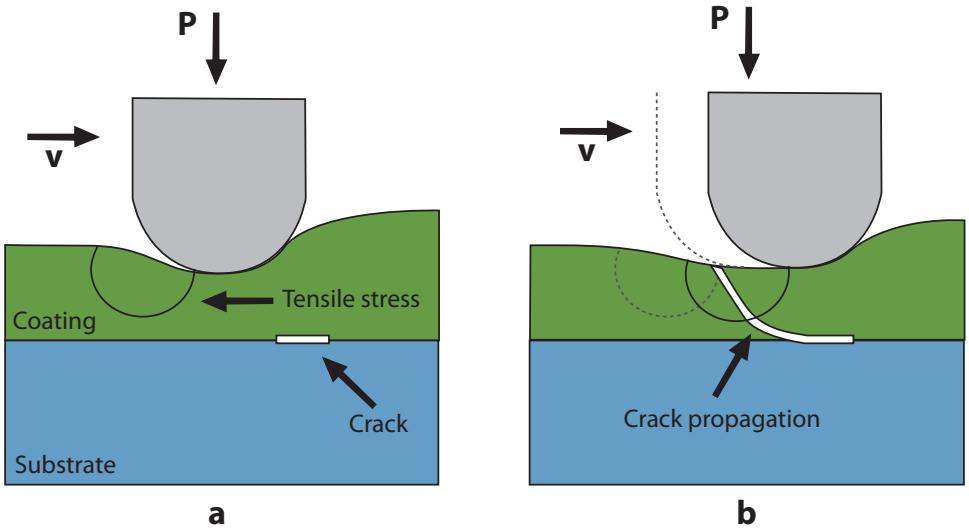

Figure 7.8 – Schematic showing the crack initiation and propagation process at the coating substrate interface. Adapted from [161].

the polymer and the indenter. As the indenter advances, the friction between the tip and the coating drags the material, inducing tensile stresses on the crack; as a consequence, the crack initially propagates perpendicular to the scratch direction.

Since at a certain distance from the scratch path, the coating remains attached, the friction between the indenter and the coating is actually inducing shear stresses on the LCT layer (Fig. 7.15 c). Consequently, as the crack starts propagating, the stress field seen by the crack shifts from tensile to shear, changing the scratch direction. It is expected that this crack propagation would continue until debris is formed, which may or may not remain attached. The repetition of this process produces the damage observed on CAA (Fig. 7.4 d) and GB (Fig. 7.4 e) pretreated samples. The main difference between these two pre-treatments is that in the case of CAA the lateral propagation is through delamination at the oxide-coating interface, while in the GB samples it is through cohesive spallation.

The analysis of SEM micrographs of fracture surfaces seems to indicate that for cured LCTs, the tensile cracks on the scratch-path walls are initiated at the interface between the coating and the substrate, and propagate upwards, towards the upper surface of the coating (Fig. 7.16 a). Once the crack reaches the top surface, it propagates away from the scratch path with a certain angle with respect to the scratch direction (Fig. 7.16 b). The eventual failure of the molecules will lead to the formation of abrasion particles which either remain attached very loosely to the bulk of the material (Fig. 7.16 c) or may detach completely as wear debris.

Fig. 7.17 summarizes the lateral spallation behavior for the various coatings studied here. Both the LCT and Vectra® coatings show cohesive failure on PAA aluminum. In the case of the LCTs, however, this spallation occurs ahead of the tip, probably

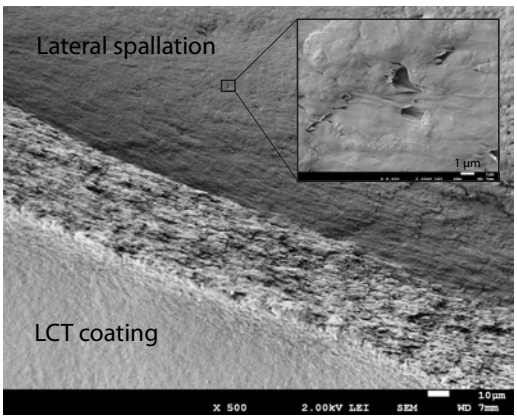

Figure 7.9 – SEM image of a lateral spallation induced during the scratching of the 5000 $\frac{g}{mol}$ LCT coating on a PAA pre-treated substrate. The inset presents a detail of the spalled area, showing the fracture morphology of the remnant polymer layer.

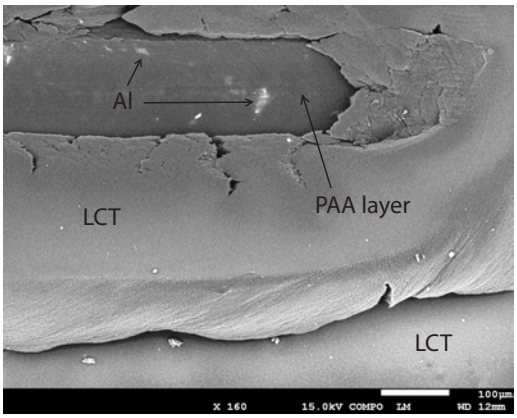

Figure 7.10 – Back-scattering SEM image of the final contact between the indenter and the substrate. Some of the areas where the oxide layer was removed, exposing the substrate, are indicated.

due to the presence of aggregate interfaces parallel to the substrate. These weak aggregate interfaces originated during LCT curing, as discussed in previous chapters, constitute paths for crack propagation.

In the case of GB substrates, the lateral spallation in LCT coatings was cohesive, occurred behind the tip, and the substrate remained protected by a thicker layer of polymer compared to the PAA pre-treatments. Vectra® coating on GB aluminum, on the other hand, failed adhesively. These results appear to support previous statements regarding the positive effect of the phenylethynyl reactive end-groups on adhesion (Chapter 5). In the present tests, however, this shift to interfacial failure on Vectra® samples could be induced by their higher cohesive strength (due to the absence of agglomerate interfaces). Therefore, these results are not conclusive regarding the improved addition of the LCTs.

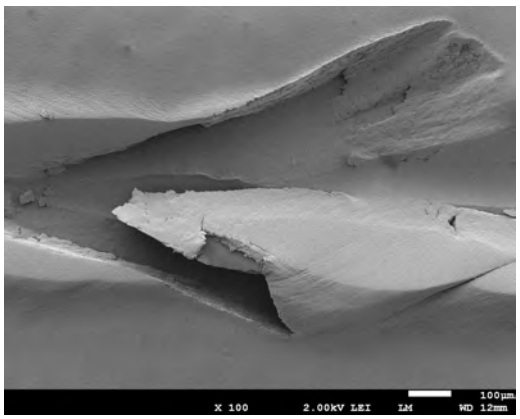

Figure 7.11 – Detail of the spallation failure induced on PAA pretreated samples during the microscratch test. The spallation on both sides of the scratch forms a triangular shape.

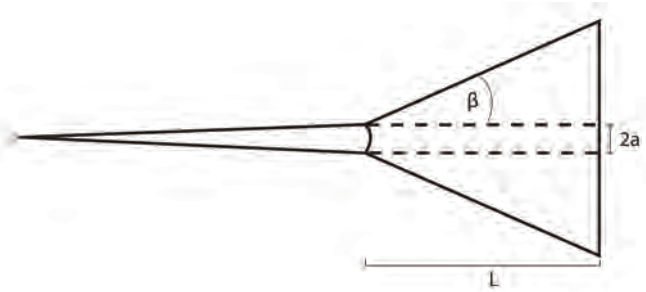

Figure 7.12 – Schematic representation of a typical trapezoidal delamination produced ahead of a scratch of width *2a*. The failure is said to have a length L, with sides prescribed by radial cracks at an angle β respect to the scratch direction. Adapted from [162].

7.4.2 Environmental resistance

The resistance to the fluids listed in Tab. 3.2 was tested by full immersion during 500 h. The Visual inspection of LCT and Vectra® coatings showed no blistering, gloss change or delamination from the grit-blasted AA5083 aluminum substrate. In an attempt to evaluate the absorption of fluids during the immersion, samples were also weighed before and after exposure. All coupons showed no detectable weight increase; although this measurement was limited by the minimum resolution of the precision balance (i. e. 0.1 mg). During the present experiments, the minimum resolution of the balance was approximately 1 ‰ of the weight of coating material per sample, while the moisture absorption at saturation of Vectra® A950 is 0.3 ‰ [172]. The resistance of the coatings to the combined effect of temperature and moisture was also investigated. Coated coupons were exposed to hot moisture for 1000 h, and neither failure of the coating (such as blistering or peeling), nor detectable weight increase were observed.

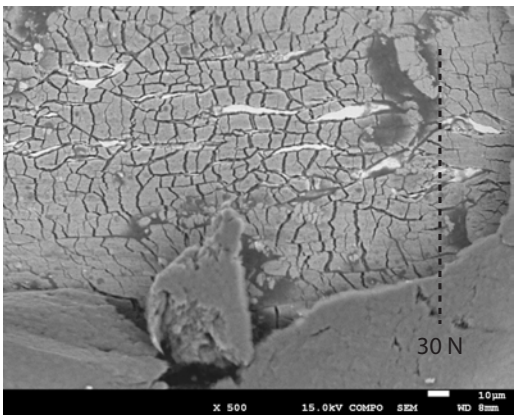

Figure 7.13 – Back-scattering SEM images of the scratch track produced on LCT coatings on CAA pre-treated aluminum during the progressive scratch test

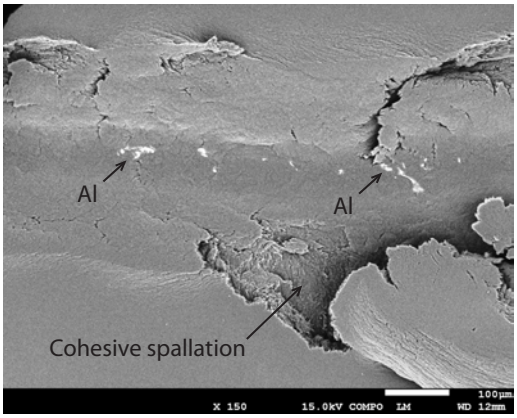

Figure 7.14 – Back-scattering SEM image showing the scratch behavior of the cured LCT on GB aluminum. The lateral spallation is fully cohesive. The light spots indicated by the arrows are exposed aluminum substrate along the scratch path.

In the salt fog spray tests, both LCT and Vectra® coatings showed degradation neither at the scribe nor at the polymer after 1000 h of exposure. On the other hand, the same coatings applied on highly corrosion susceptible AA2024-T3 and AA7075-T6 presented corrosion products at the scribe and blisters in areas adjacent to the cross-cut and coating edges; the rest of the coating did not present visible damage. The extreme variation in corrosion behavior with respect to the AA5083, can be understood by the intrinsic superior corrosion resistance of the magnesium alloy (AA5083) to the saline environment [95]. In addition, it should be considered as well, that the 2000 and the 7000 series aluminum alloys are heat treatable, and their maximum processing temperatures are 120 °C and 180 °C, respectively. Therefore, after melt pressing and curing, the original microstructure obtained by the solution-heat treatment was lost, potentially decreasing even further the resistance of these substrates.

To further investigate the effects of the accelerated corrosion on the LCT coatings,

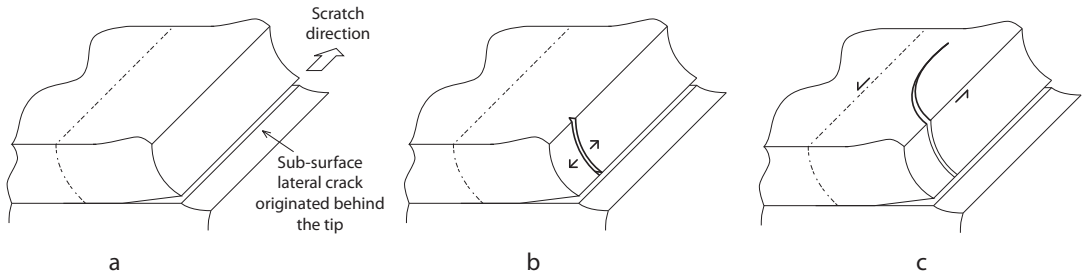

Figure 7.15 – Proposed mechanism for the formation of lateral spallation observed on LCT coatings on CAA pretreated samples. (a) Coating delaminates due to propagation of lateral crack at the interface LCT/CAA layer, (b) A crack initiates at the sides of the scratch due to tensile stresses behind the tip, and (c) the crack propagates due to shear stresses on the LCT layers.

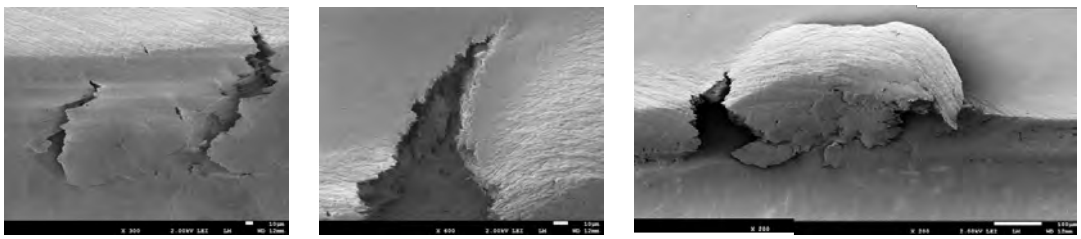

Figure 7.16 – SEM micrograph of a scratch-track wall showing the initiation and propagation of tensile cracks behind the tip on a cured LCT coating applied on GB aluminum

adhesion tests were performed before and after the salt-spray tests. Fig. 7.18 shows the pull-off and lap-shear strengths of LCT coatings cured 1 h at 350 ^{o}C, on AA5083-H111 aluminum substrates. The pull-off strength decreased approximately 13 %, while the lap-shear strength decreased by 63 %. To understand this behavior, one has to consider that for the pull-off test, the stud was bonded at several millimeters from the coating edges, after exposure to the corrosive fog. On the other hand, lap-shear samples were bonded and cut before being exposed, implying that coating edges were directly exposed to the corrosive environment.

These results indicate the influence of coating-edge effects. Degradation at the coating-substrate interfaces could be attributed to corrosion advancing form the interface (such as crevice corrosion). On the other hand, diffusion of water and/or chlorides (Cl^-) from the environment could occur through the interface, weakening the physical and/or chemical bonding of the coating. Although further analysis would be required to establish the precise mechanism, results show that there seems to be a relatively slow degradation process advancing from the exposed coating-substrate edges.

The environment can also degrade the polymer properties without visible damage.

Figure 7.17 – Schematic summary of the lateral delamination observed for LCT and Vectra® coatings on PAA and GB aluminum.

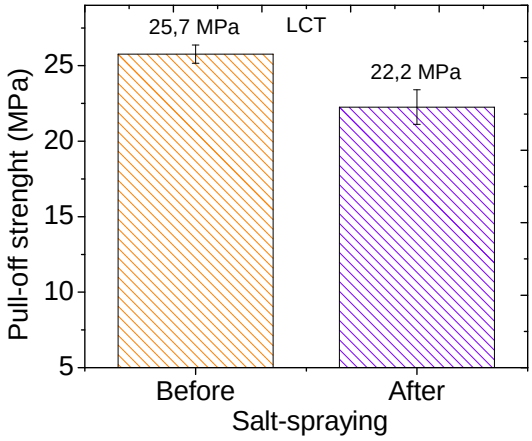

(a)

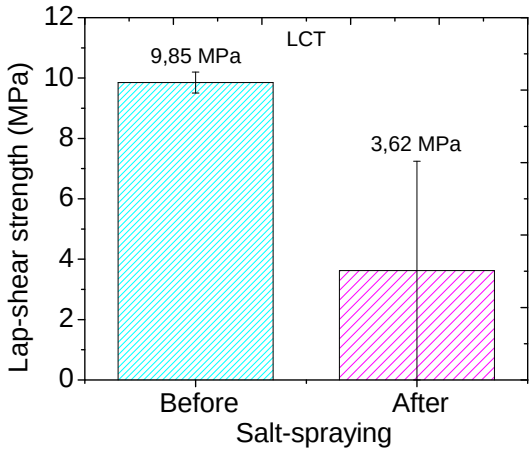

(b)

Figure 7.18 – Pull-off (a) and lap-shear (b) strength of LCT coatings before and after standardized salt-spray testing

For instance, solvent absorption lowers the Young's modulus of polymers such as PEEK [173]. Nanomechanical studies of exposed samples could reveal environmental effects on visually unaffected coatings, constituting a main tool in assessing durability. Fig. 7.19 shows the elastic modulus and hardness of LCT and Vectra® coatings before and after salt-spray testing and immersion in Skydrol®, one of the most aggressive aviation hydraulic fluids. All coating surfaces retained their mechanical properties, indicating excellent resistance.

All in all, the liquid crystalline thermosets showed chemical resistance comparable to that of traditional thermotropic liquid crystalline polymers. Results indicate that the end-groups and curing products, which do not interfere with the mesophase formation [27], have also little or no effect on the chemical resistance to the different media.

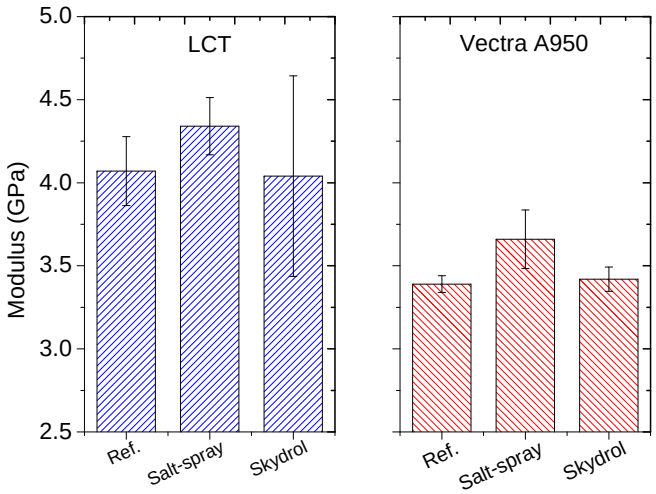

(a)

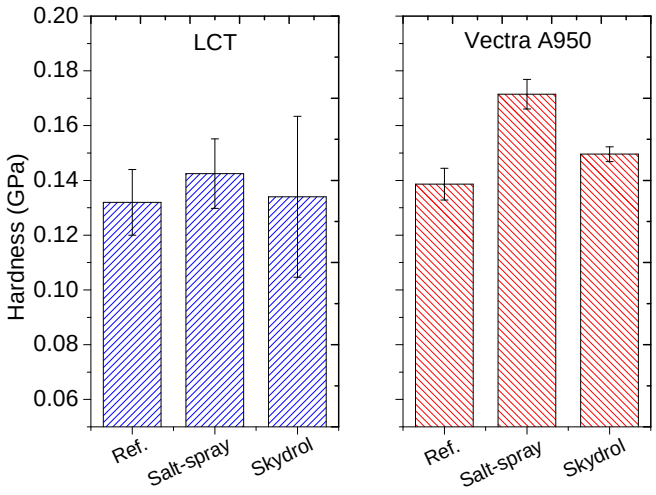

(b)

Figure 7.19 – Modulus (a) and hardness (b) of the LCT and Vectra® coatings before (Ref.) and after a standardized salt-spray testing and a 500 h full-immersion test in Skydrol®.

7.5 Conclusions

This chapter addressed two fundamental properties of coatings: adhesion and environmental resistance. The coating-substrate interface of LCT and Vectra® coatings was investigated using progressive-load microscratch testing. Non-pretreated (NP) and chromic-acid anodized (CAA) samples failed adhesively. In addition, during scratching, the CAA oxide layer failed, exposing the substrate. On the other hand, phosphoric-acid anodization (PAA) appeared to improve the adhesion of both polymers. The lateral spallation is cohesive for both coatings, presenting a thin remnant polymer layer at the failures. In the case of the LCT, however, these failures occur ahead of the indenter and further improvement in adhesion is required.

LCT coatings on GB samples failed cohesively, behind the tip, and leaving a thick, remnant layer on the substrate. This leads to the conclusion that, among the various pretreatments studied here, GB is the most beneficial to improve the adhesion of LCT coating under sliding conditions. On the other hand, in the case of Vectra® coatings on a GB sample, the spallation failure was at the coating-substrate interface. This difference, however, might be caused by the presence of aggregate interfaces parallel to the substrate in the LCTs, which constitute paths for crack propagation.

The environmental resistance of the LCTs was found to be comparable to that of the original thermoplastic chemistry. No visible failures or detectable weight increase was observed after exposure to hot-moisture, corrosive fog, or aviation fluids. In addition, coatings were also observed to retain their surface mechanical properties after exposure. This indicates that the end-groups and curing products do not interfere with the environmental resistance of the coating, which could be attributed mainly to the liquid crystalline behavior.

On the other hand, results also showed that the interface between the coating and the aluminum substrate is sensitive to environmental attack. There is a clear edge effect, where interfaces directly exposed to the environment allow for the penetration and diffusion of surrounding elements, weakening the interfacial bonding. Further research is required to determine the exact mechanism, and improve the coating-substrate interface, in order to reduce its environmental degradation and increase durability.

8 Thermal Spraying of Liquid Crystalline Thermosets: Feasibility Study

8.1 Summary

Thermal-spraying would increase the range of potential applications of the LCT coatings, since it allows deposition in-field, on large surfaces of a wide range of substrate materials, and without the use of solvents. Therefore, the applicability of the phenylethynyl terminated LCTs using atmospheric plasma spraying (APS) was investigated. In particular, a 5000 $\frac{g}{mol}$ LCT was plasma-sprayed on aluminum and composite substrates.

Good wetting and flow of the sprayed LCT was observed on the studied substrate materials, including degraded pre-deposited LCT splats. In addition, despite the incomplete crosslinking, deposits show good inter-splat coalescence. On the other hand, APS has an intrinsic degree of defects, such as porosity and polymer degradation. As a result, process optimization is required; for which, the main parameter appeared to be the particle sizes of the feedstock. In the case of composite substrates, however, the process optimization window is more restricted due to the low degradation temperatures and thermal conductivity of both the substrate and the sprayed material.

8.2 Introduction

In the initial chapters of this thesis, it was mentioned that the use of LCPs for coating applications has been limited not only due to poor adhesion properties, but also due to their difficult processability into coatings. On one hand, thermotropic LCPs such as Vectra® only dissolve in expensive and hazardous solvents, such as pentafluorophenol (PFP) at 60 ºC [23, 27], limiting their application from solution. On the other hand, the grinding of thermoplastic LCPs like Vectra® is extremely high energy-consuming. In addition, the resulting powder morphology (Fig. 2.6) is

not suitable for most powder coating techniques, due to its hierarchical fracture (Fig. 2.14) [26].

The oligomer approach has the potential to overcome these deficiencies. As discussed in previous chapters, the LCTs seem to have improved adhesion due to the incorporated polar end-groups. In addition, while it is still processable as a thermoplastic (within the processing window), the reactive oligomer has a lower molecular weight and (as discussed below) can easily be ground for powder coating applications.

Powder coatings are applied as a dry, free-flowing thermoplastic or thermosetting powder. One of the main advantages of the use of powder coating techniques is the emission of zero or near zero volatile organic compounds (VOC), [174, 175]. In addition, powder coating production lines produce less hazardous waste than conventional liquid coatings; and the overspray can be recycled. On the other hand, it is not easy to apply smooth thin films ($<50\,\mu m$). Uniformity of coating thickness is sometimes difficult to maintain, it is complex to coat sharp corners, and very small particle sizes are required.

The powder is typically applied electrostatically, and the particles are slightly attached to the substrate. Subsequent substrate heating allows the static particles to flow and form a "skin" (and crosslink in the case of thermosets). The most widely known powder coating technique is electrostatic spraying, using a corona or a tribo-gun. Other methods include the so called fluidized bed dipping, electrostatic magnetic brush, powder slurry, where the powder is used in an aqueous dispersion, and electophoretic deposition [174–176]. Due to the rheological behavior of LCPs, however, the static mesophase does not flow during heating to form a uniform, continuous coating.

Other powder-coating methods have been developed, such as thermal-spraying, which do not require electrostatic charging of the powder. Thermal spraying is a continuous, directed, melt-spray process. During thermal spraying, particles of virtually any material are melted and accelerated to high velocities, through either a combustion or a thermal-plasma flame [177]. The molten or semi-molten droplets impinge on a substrate and rapidly solidify to form a thin "splat" [93]; thus, the deposit is built-up by successive impingement and inter-bonding among the splats (Fig. 8.1).

Among the powder coating methods, thermal spraying is particularly interesting for the application of LCPs, because the particles are melted and forced to shear against the substrate, reducing their viscosity and facilitating flow [178, 179]. In addition, thermal spraying offers high versatility in feedstock materials (metals, ceramics, and polymers) and shapes (powder, wires, rods) [180]. Moreover, large and free standing structures of a wide variety of materials can be coated with this process. Disadvantages of thermal spraying include lower quality surface-finish and high levels of noise emission [93].

The main thermal spraying methods can be divided into two groups: combustion and electrical methods. Combustion methods include flame spraying and high-velocity

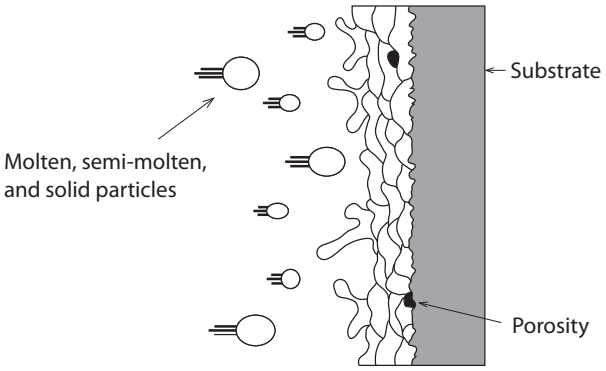

Figure 8.1 – Schematic representation of coating build-up during thermal-spraying

oxy-fuel (HVOF), and are based on the use of fuel and oxygen. Electrical methods, which include electric-arc wire and plasma spraying, use electricity and gas (if applicable) as their energy source [93]. Non-traditional thermal spraying processes include radio-frequency-induction plasma and cold-spraying. The main difference between all these methods is the amount of thermal and kinetic energy they impart on the feedstock material (Fig. 8.2).

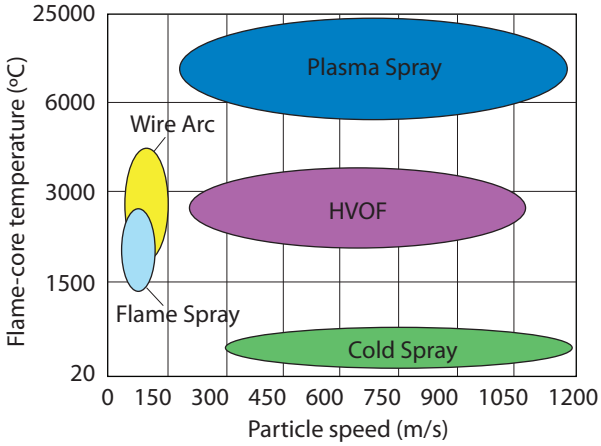

Figure 8.2 – Estimated gas temperatures and particle speed regimes for common thermal spray processes. Adapted from [181].

Thermal spraying had been traditionally used to spray metals and ceramics. The spraying of polymers is more recent, and it is still maturing. Initial studies on thermal spraying of polymers focused on flame spraying, due to the lower melting and decomposition temperature of these materials [93]. It was later suggested, however, that high particle velocities are required for better splatting, coating adhesion and cohesion, and reduced porosity, even if the polymer is still relatively viscous [79, 93, 177, 182].

A wide variety of polymers such as Nylon, PMMA, PEEK and PPS have been thermal sprayed using HVOF and plasma spraying, on a wide variety of substrates

including an AA5052 aluminum alloy [183–185]. Some of the main applications of thermal sprayed polymers include anti-corrosion at high temperatures in the chemical industry [183] and wear protection [186]. Very few researchers have reported thermal spraying of LCPs [81, 184], and they provide limited information about the processing and characterization performed. For this work, plasma-spraying (Fig. 8.3) was selected due to its inert heat source, and higher accuracy and range in the control of processing parameters such as feed-rate and flame temperature. During spraying, the process atmosphere was air, a variant known as atmospheric plasma spraying (APS).

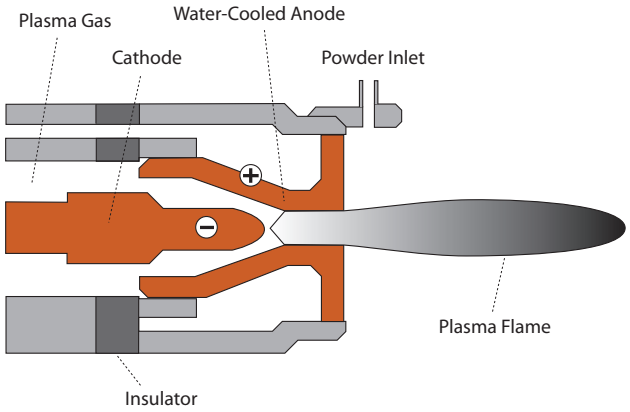

Figure 8.3 – Schematic representation of a plasma-spray gun. Adapted from [177].

The aim of the present research is to study the feasibility of thermal spraying, particularly APS, as an alternative to melt-pressing for the deposition of liquid crystalline thermosets. This chapter is divided into three parts. In the first section, the suitability of APS for the deposition of LCTs was evaluated in relation to the grinding and process characteristics, and some preliminary spraying tests are presented. In the second part of this chapter APS deposits are characterized. It starts by relating process parameters to the behavior of single splats, which are the building blocks of the coating. Subsequently, the actual coating build-up was analyzed, and the inter-splat adhesion and curing of the deposits was discussed. In the final section, the plasma-spraying of LCTs is taken a step further by exploring the applicability of LCTs on composite structures. In this section, the behavior of particles deposited on composites was investigated, and the thermal effects on the composite substrate analyzed.

8.3 Materials and characterization

8.3.1 Materials

A 5000 $\frac{g}{mol}$ LCT was synthesized according to the procedure previously reported by Knijnenberg et. al. [27]; and the thermoplastic counterpart LCP, Vectra® A950,

was obtained from Ticona GmbH (Kelsterbach, Germany). The polymers were applied on three types of substrates. First, the non-heat treatable aluminum alloy AA5053-H111 was used; then, the LCT was also deposited on glass-fiber (GF) and carbon-fiber (CF) reinforced polyetherimide (PEI) composite substrates (see sec. 3.2.2). Unless otherwise stated, all substrates were grit-blasted with 90-150 µm glass beads right before thermal-spraying.

8.3.2 Powder preparation

Grinding of Vectra® A950 pellets led to the hairy or "bird-nest" like shapes reported by the manufacturer (Ticona GmbH). In order to reduce the degree of alignment induced during manufacture of the LCP pellets, the as-received granules were melt-pressed into films and pre-grinded in a cutting-mill. This improved grinding and reduced agglomeration in various cryogenic-mills systems. These processes, however, required working in small batch sizes (3 to 5 g), increasing processing costs and time. In addition, the particle-size distributions were centered around 200 µm (far above the recommended values) and the powder possessed poor flow properties (see Fig. 2.6).

The 5000 $\frac{g}{mol}$ LCT was ground in a planetary ball mill (PM 100, Retsch GmbH, Haan, Germany), using a 250 ml zirconium-oxide jar equipped with 20 and 30 mm diameter zirconium grinding-balls.

8.3.3 Coating deposition and characterization

Coating deposition was performed using an atmospheric plasma-spray (APS) system F4MB-XL (Sulzer Metco Europe GmbH, Kelsterbach, Germany), in collaboration with the Surface Engineering Institute at the Faculty of Mechanical Engineering, RWTH Aachen University, Germany. During a typical APS deposition, the plasma flame was used to pre-heat the substrate with a variable number of passes, prior to the injection of the feedstock.

To characterize the sprayed coatings, a number of tests were performed. Constant and progressive load micro-scratch tests were performed as described in sec. 3.4.3.2, using a computer controlled microindenter equipped with a 100 µm radius Rockwell tip. The morphology of the deposits and the failures associated with the scratch test were identified using scanning electron microscopy (SEM), and optical microscopy (OM). Thermal analyses were performed using differential scanning calorimeter (DSC). For these analyses, sample material was collected by gently removing coating material deposited on a polished metallic substrate.

8.4 Results and discussion

8.4.1 Coating process

8.4.1.1 Grinding of the LCTs

Some of the critical parameters for the successful deposition of polymeric materials using thermal-spray are the morphology, size, and size distribution of the powder [187]. Grinding during 10 min in a planetary ball-mill produced particles with a rounded, non-fibrillar morphology (Fig. 8.4 a), which is required for a good flowability of the dry powder into the plasma-flame. The particle size distribution of the LCT after grinding is presented in Fig. 8.4 b. Due to the low density and electrostatic behavior of the polymer particles, particle separation using standard dry sieving was limited. The recommended size distribution for the plasma-spraying of the LCTs indicated in Fig. 8.4 b is based on observations of the degree of melting and flow of the particles during the present study.

8.4.1.2 Process parameters and preliminary spraying tests

The process parameters evaluated during this feasibility study can be divided into three groups: feedstock properties (particle size, size-distribution, and shape), substrate characteristics (pre-treatment, temperature, roughness), and APS system parameters (plasma gasses flow and composition, plasma-torch current, standoff distance, transversal torch speed, and powder-carrier gas flow). Since all the process parameters are interrelated, it is important to notice here that, in these experiments, the carrier-gas flow was set at low rates to minimize the use of feedstock material. As a consequence, a lower current could be used to reduce energy input into the in-flight particles and deposit, due to the lesser amount of polymer in the flame to take up the heat.

In order to obtain a first estimation of the optimum process parameters, a series of preliminary spraying tests on aluminum were performed; the main process parameters selected are presented in the Tab. A.1 of the Appendix. During the preliminary spray trials, deposits with a variety of morphologies, colorations, and decomposition were obtained (Fig. 8.5, Fig. 8.6, and Fig. 8.7). These preliminary results also show an excellent level of contact between the splat and the substrate, with good wetting of the LCT on the aluminum, and a good flow into the rough grit-blasted surface.

8.4.2 Coating characterization

8.4.2.1 Splat formation and process parameters

The quality of a thermal sprayed coating is defined by the behavior of single particles upon impact, i. e., the splat behavior. The individual splat formation depends on

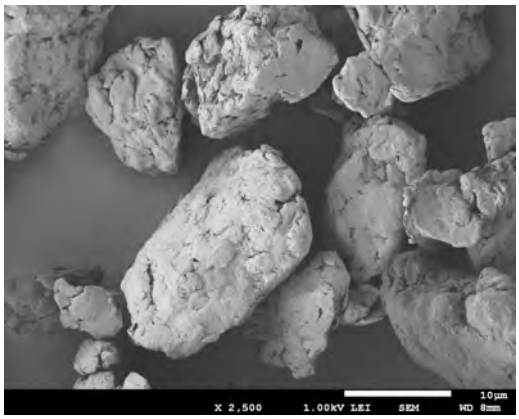

(a)

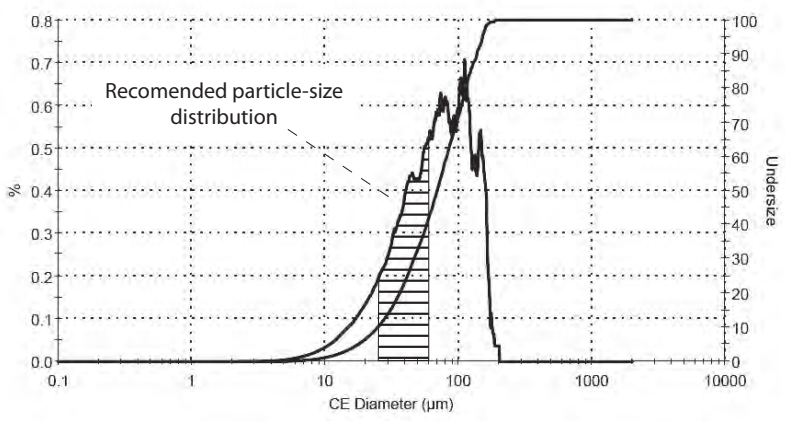

(b)

Figure 8.4 – (a) Morphology of the LCT powder grinded 10 minutes in a planetary ball mill. (b) Particle size distribution of the LCT powder. The recommended particles sizes for plasma-spraying are indicated.

parameters such as the temperature of the substrate, and the velocity, molten state, and angle of impact of the droplets onto the surface [188]. These variables are determined by the particular combination of process parameters.

Based on the preliminary results, the parameters presented in Tab. 8.1 were selected (i.e., *S15* in the Tab. A.2 of the Appendix). Using these parameters, very low degradation of the deposits was induced; however, insufficient melting and spread was observed. This set of parameters was selected as the baseline to investigate the effect of the flame temperature, standoff distance, roughness, substrate preheating, and transversal gun speed on the morphology and degradation of the deposits, and achieve further optimization.

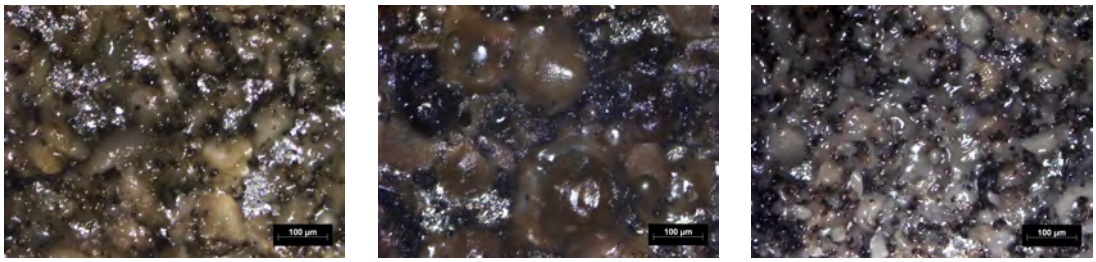

(a) (b) (c)

Figure 8.5 – Optical micrographs of the top-view of deposited particles using the parameters *S10* (left), *S11* (center), and *S12* (right). The images show a variety of splat morphologies and colorations.

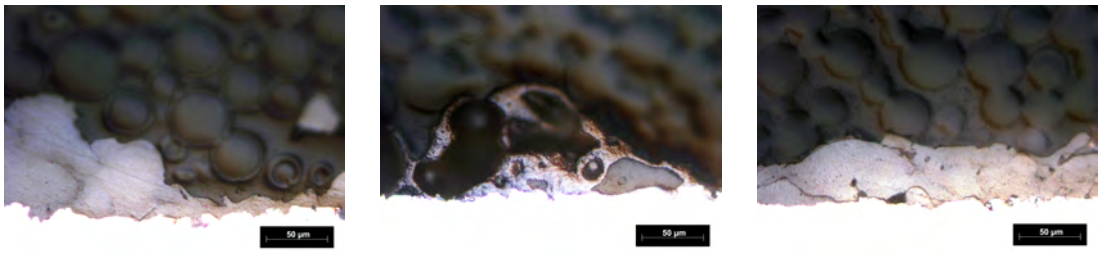

(a) (b) (c)

Figure 8.6 – Optical micrographs of cross-sections of particles deposited using the parameters *S10* (left), *S11* (center), and *S12* (right). The images show a variety of splat degradation, microstructures, and particles coalescence.

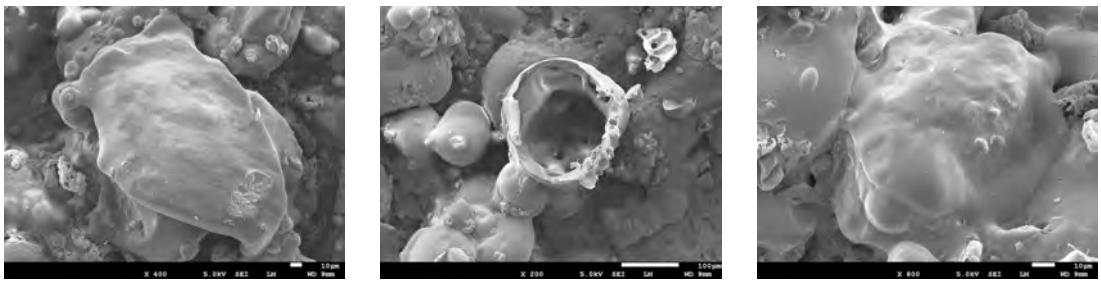

(a) (b) (c)

Figure 8.7 – SEM micrographs of the top-view of particles deposited using the parameters *S10* (left), *S11* (center), and *S12* (right). The images show a variety of splat behaviors (flow on impact) and degradation.

Flame temperature

An increase in flame temperature increases particle kinetic and thermal energy. Experimental studies have shown that increasing particle velocity and temperature increases flow at impact and reduces particle bounce-off [182, 188]. On the other

Table 8.1 – Initial process parameters for the plasma spraying test

Current (A)	**Fisrt gas** (SLPM)	**Second gas** (SLPM)	**Standoff distance** (mm)	**Torch speed** ($\frac{mm}{s}$)
250	50 (Ar)	0	120	50

hand, large temperature gradients develop below the surface of in-flight polymer particles [189], primarily due to the low rate of internal heat conduction of polymers. Therefore, a balance needs to be achieved between surface decomposition and core melting.

In order to increase the thermal energy of the plasma flame and increase droplet flow, hydrogen (H_2(g)) was introduced as a secondary gas, while increasing the transversal speed of the torch to reduce degradation of the deposit. It was observed that the increase in the thermal energy of the flame improved the melting and flow of the splat. At the same time, there is an important increase in the number of unmelted or partially melted small-size particles present in the deposit (Fig. 8.8). This could be attributed to an increase in secondary splatting (discussed below); but it could also be originated by a higher adherence of small particles traveling in the periphery of the flame, induced by the increase in deposit/substrate temperature. There is also a noticeable increase in post-deposition degradation occurring during the successive spraying passes.

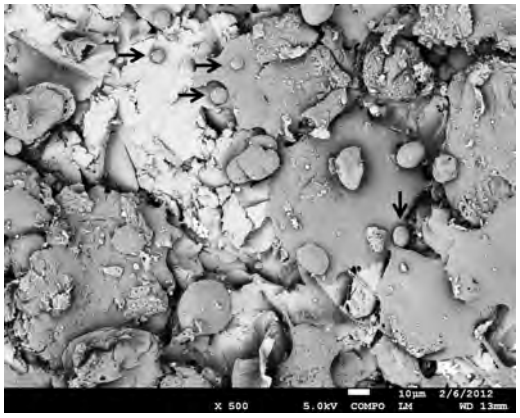

Figure 8.8 – Morphology of the deposits formed after increasing plasma-flame temperature. Some of the secondary splats are indicated with arrows.

Increasing the energy of the plasma flame by increasing the current and the flow of the main gas was also observed to improve melting and flow at impact of LCT particles (within a certain size distribution). Fewer secondary splats seemed to be formed; however, superficial, post-deposition degradation during successive gun passes was still observed.

Standoff distance

In order to reduce the thermal effects on the deposit, the standoff distance was increased from 120 to 150 mm. The superficial degradation of the deposits, however, was not sensibly reduced. On the other hand, the melting and spread of LCT particles declined, which also increased particle bouncing-back. Decreasing the standoff distance to 90 mm induced decomposition and out-gassing of the deposit, and intra-splat porosity developed.

Roughness

Single droplets on a polished steel substrate formed a smooth, highly deformed, disk-like splat (Fig. 8.9), which is indicative of good in-flight melting of particle (within a certain size distribution). Splat formation is also facilitated by the shear-thinning phenomenon [181]. Shear-thinning is particularly important in LCPs, due to their larger reduction in viscosity under shear stresses compared to other non-LCP polymers.

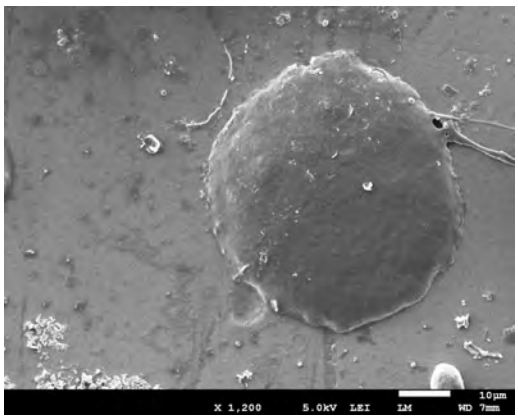

Figure 8.9 – SEM image showing a single splat of plasma-sprayed LCT on a polished steel substrate

Grit-blasting and coating build-up increases surface roughness. A fully conformed interface between the polymer and the rough surface improves the adhesion of the coating due to mechanical interlocking [190, 191]. This mechanical interlocking between the deposit and the substrate was observed at the center of the splat (see for example Fig. 8.6). The substrate roughness, however, promotes also splat instability, resulting in radial jetting ("fingers") and break-up ("satellites") [181, 192]. The high-speed radial jets spread over the substrate, solidifying and settling on top of rough substrate asperities (Fig. 8.10), without flowing into the irregularities of the substrate or underlying splats [192, 193]. This decreases coating-substrate interaction and increases inter-splat voiding. The morphologies resulting from jetting (Fig. 8.11) and break-up of the droplet (presented in Fig. 8.8) appeared to be important in LCPs due to their particular shear-thinning behavior [181].

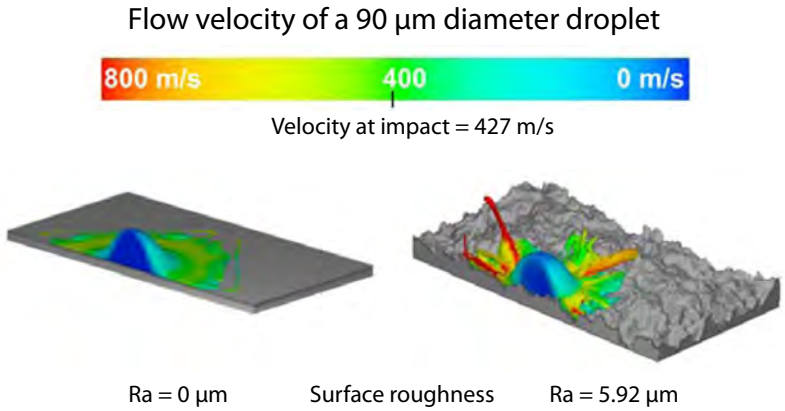

Figure 8.10 – Cross-section of predicted three-dimensional spreading splats for a 90 µm diameter Nylon-11 particle impacting on two different surface roughness. Adapted from [179].

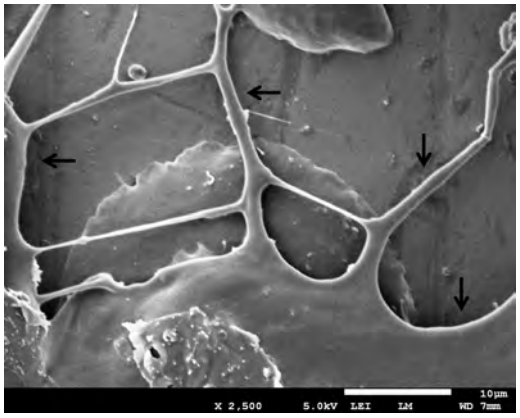

Figure 8.11 – Radial jetting ("fingers") of a melted LCT particle upon impact on a non-flat surface. The empty areas below the radial jets (indicated with arrows) are prone to originate inter-splat porosity.

Substrate pre-heating

One of the main parameters to be controlled during the thermal spraying of polymers is the substrate preheating. Previous studies have reported that preheating induces less splashing and more disk-shaped splats on smooth substrates [193]. In addition, it was reported that preheating also reduces porosity at the coating-substrate interface, and improves flow into the rough grit-blasted aluminum surface[181]. Furthermore, preheating is also expected to facilitate the release of internal stresses, since heat dissipation upon impact is slower.

During a typical APS deposition, the plasma flame was used to pre-heat the substrate prior to the injection of the feedstock to a temperature of approximately 180 ^{0}C. In order to improve the preheating, the 2 mm thick samples were placed on a steel block during plasma-spraying. The steel block is expected to retain more heat, maintaining

the substrate temperature more stable and homogeneous during the time interval between two passes of the gun over the same location. This was observed to be favorable for the splat formation and coating build-up, with improved splat flow and level of contact between polymer and substrate. Results showed, however, that inter-splat contact was barely improved. Post-deposition flow and coating consolidation was not observed to improve considerably, although this was expected due to the high viscosity of static LCT particles.

Transversal gun speed

The transversal speed of the gun can be reduced, in order to increase the volume of material deposited during each pass, and to reduce the final number of required scans. In addition, a lower transversal speed increases the residence time of the flame in each point, rising the pre-heating and average temperature of the substrate.

Reducing the transversal gun speed, superficial degradation of the deposit was observed after only one pass of the torch. As the number of passes was progressively increased, the degradation of the deposit did not intensify. In addition, new splats showed good wetting and spread on degraded particles (Fig. 8.12).

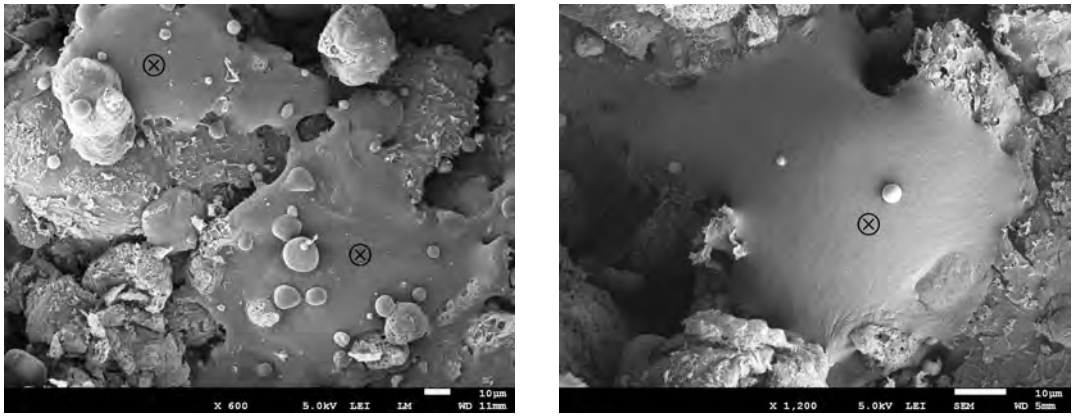

(a) **(b)**

Figure 8.12 – SEM images showing the behavior of new splats (indicated with "⊗") impacting on degraded particle surfaces

8.4.2.2 Coating build-up

The single-splat behavior determines the coating build-up and, in turn, the adhesion, strength, microstructure, porosity, and residual-stress state of the final coating [92]. To study the coating build-up, an approximately 500 µm thick LCT layer was deposited (*S29*). Good flow and spread of particles within the appropriate size distribution were observed (Fig. 8.13 a), even upon impact on un-melted LCT

particles, resulting in good inter-splat wetting (Fig. 8.13 b). Despite the observed spread and flow of droplet on colder, unmelted particles, a high degree of inter-splat porosity was observed (Fig. 8.14). This porosity can be attributed to the insufficient flow of unmelted particles above the optimum size distribution [78]. In addition, although the observed degradation of particle surfaces was much lower than expected based on previous tests with fewer gun passes, this degradation appears to originate considerable inter-splat voiding (see Fig. 8.14).

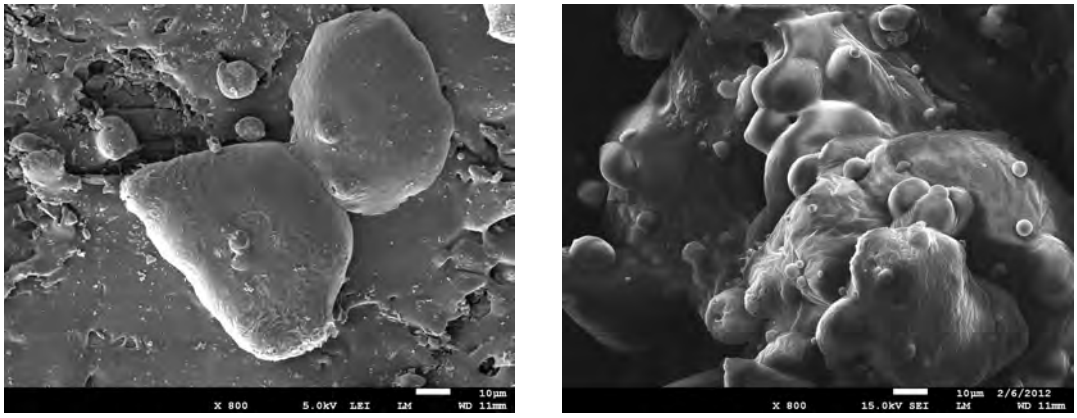

(a) **(b)**

Figure 8.13 – SEM images showing the initial build-up on aluminum (*S20*) and the splats pile-up after reducing transversal torch speed and increasing the number of coating passes (*S29*)

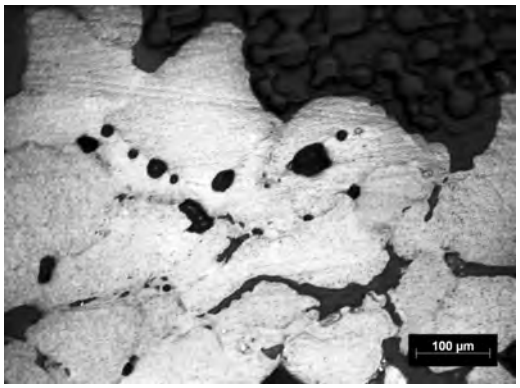

Figure 8.14 – Optical micrograph showing the cross-section of sample S29. The image shows insufficient in-flight melting of large particles and isolated and interconnected inter-splat porosity. The inter-splat porosity could be originated either by (a) poor flow of unmelted and partially melted particles or (b) degradation of particles surfaces.

All in all, the main parameter affecting coating build-up appears to be the particle size distribution of the feedstock. Splats with unmelted cores were observed during

this analysis, due to temperature gradients developed within the particle. This provides an indication of the critical maximum particle size required for an optimum in-flight melting, which is estimated to be from 50 to 60 µm. On the lower limit, particles should be larger than approximately 25 µm [93, 181], because light in-flight particles tend to fly away from the flame, burn, or vaporize. The resulting recommended particles-size distribution is indicated in Fig. 8.4 b.

Inter-splat coalescence during coating build-up

Inter-splat coalescence during build-up is critical to obtain a strong and tough coating. The physical processes responsible for coalescence are particle deformation, diffusion, and internal-stress relaxation [194], which depend on intrinsic (surface tension) and extrinsic (applied temperature and pressure) properties. In order to evaluate inter-splat adhesion, constant and progressive load micro-scratch tests were performed. Fig. 8.15 and Fig. 8.16 show the scratched surfaces of a thermal sprayed LCT layer with a thickness of approximately 500 µm.

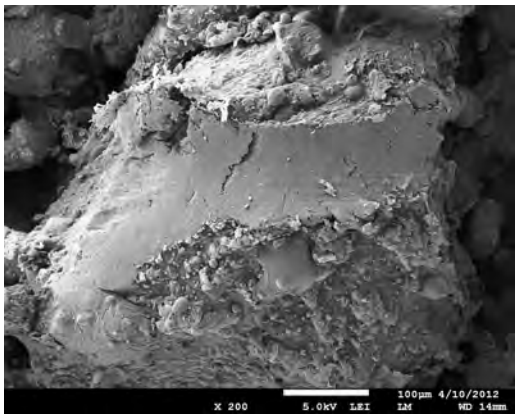

Figure 8.15 – Scratch path on a single particle at a constant load of 1 N

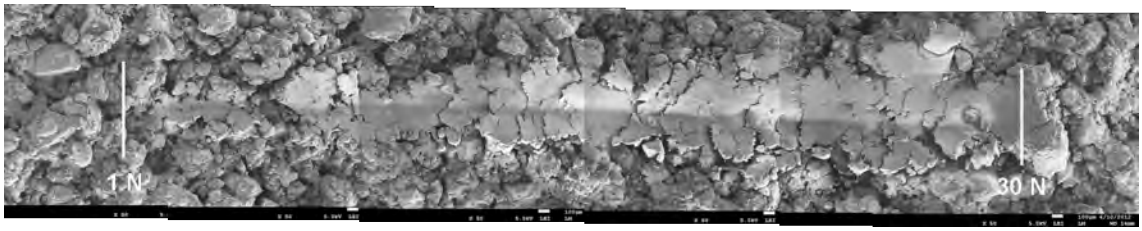

Figure 8.16 – SEM images showing the morphology of an 8 mm long scratch path produced during a progressive scratch test

During the progressive scratch-test, the penetration depth at the final load of 30 N ranged between 300 and 400 µm, mainly due to the highly irregular microstructure of the coating. Nevertheless, splats are scratched and deformed by the tip, instead

of detaching from the deposit. This lack of inter-splat failure, despite the inter-splat voiding, indicates good inter-particle coalescence.

Curing during coating build-up

Previous studies have suggested that the residence time of in-flight particles in the plasma flame is in the order of 1 ms (depending on particle size) [118], concluding that the reactive deposition of a thermoset is unlikely [176, 195]. On the other hand, the curing time of LCTs was previously observed to decrease exponentially with the temperature [196]. In addition, successive gun passes provide further heat input into previously deposited particles. As a result, a certain degree of curing could be expected. In order to investigate the curing of the deposit, thermal analysis was performed. Fig. 8.17 shows the DSC curve of a plasma-sprayed LCT coating. A melting endotherm can be clearly observed, indicating the incomplete reaction of the thermosetting polymer.

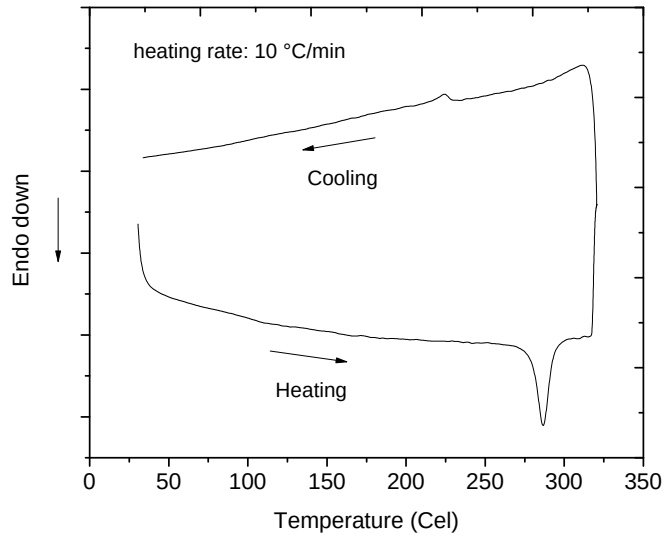

Figure 8.17 – Differential scanning calorimetry (DSC) of an LCT plasma-sprayed using parameters *S29* (see Tab. A.2 of the Appendix)

During APS, there is a distribution of particle sizes and a temperature gradient within the flame. Therefore, depending on its size and flight-path relative to the plasma-flame, each particle can have a variety of thermal histories; and, subsequently, a variety of thermal behaviors might be expected. Thus, the observed DSC curve might be the resulting thermal behavior of a series of particles with varying degrees of crosslink. This intrinsic dispersion in the curing degree of plasma-sprayed particles suggests that the phenylethynyl terminated LCT coatings can not fully crosslink during APS. Therefore, post-curing of the deposits would be required to ensure complete crosslinking of the end-groups.

The polymer chemistry and processing could be adapted to promote crosslinking during thermal spraying [195], saving time and reducing costs by eliminating the post-curing step. On the other hand, thermal sprayed LCT coatings are potentially applicable with no further post-curing, since, as suggested in previous chapters, partially cured particles are less brittle and posses an environmental resistance equivalent to that of fully crosslinked samples. Nevertheless, due to the porosity and possibly different microstructure of the polymer compared to melt-pressed coatings, further study is required.

8.4.3 Deposition on composite substrates

In this final section, the possibility of spraying LCTs on composite substrates is explored by investigating the flow and wetting of sprayed LCT on the substrate materials, and the thermal degradation of the laminate. As indicated in the previous sections, preheating of the substrate is critical for the flow and consolidation of thermal-sprayed polymer particles. Therefore, for the thermal spraying on composites, a substrate material with high characteristic temperatures is required. A thermoplastic PEI matrix was selected due to its T_g of 215 ^{o}C [197], well above that of other high-performance polymers such as PPS and PEEK. Glass-fiber (GF) and carbon fiber (CF) reinforced PEI composites are currently used in secondary aircraft structures and interior applications by Airbus, Fokker, Boeing, and Gulfstream [198]. Its use, however, is limited due to aspects such as the low chemical resistance and relatively high moisture absorption of PEI, and might, thus, benefit by a protective coating.

First, the splat behavior of the LCT on the components of the selected composite substrate was investigated. Single splats were deposited on GF and CF reinforced PEI; prior to the deposition, the substrates were grit-blasted, partially exposing the fibers. Plasma sprayed LCT droplets showed wetting and flow on the PEI matrix (Fig. 8.18 a), as well as on the GFs and CFs (Fig. 8.18 b and Fig. 8.18 c); and melted particles spread on the grit-blasted composite surfaces.

Additional spraying tests also showed that the effect of process parameters such as the standoff distance and flame temperature showed a similar effect on the morphology of the deposits to that observed on aluminum substrates. Furthermore, no significant differences where observed between the morphology of the splats deposited on CF and GF reinforced PEI. In addition, although the initial build-up develops as described for aluminum, further deposition and coating build-up might be affected by degradation of the substrate, due to heat accumulated during successive torch passes.

In order to evaluate the thermal effects of the plasma-flame on the composite substrate, the spray-gun was used to preheat 20 x 50 mm composite substrates, followed by spraying scans without the injection of powder. Fig. 8.19 shows the thermal effects of the spraying cycle *S28* (see Tab. A.2 in the Appendix) on the CF and GF

(a) **(b)** **(c)**

Figure 8.18 – SEM images of single splats on (a) PEI, (b) glass-fibers, and (c) carbon-fibers. The micrographs show a spread and wetting of melted LCT particles on the various selected components of the composite substrate.

reinforced PEI, respectively.

Degassing due to thermal effects was observed on both the CF and GF reinforced PEI (Fig. 8.19). This degassing could be attributed to the release of solvents incorporated during manufacture or absorbed moisture. In addition, it was found that due to excessive heating of the laminates without the application of pressure to consolidate the structure, de-consolidation and ply-separation occurred. The thermal energy and mobility could facilitate the release of residual internal stresses developed during laminate consolidation [199]. This phenomenon was more evident on the CF reinforced PEI, which heated up faster and to a higher temperature due to the higher thermal conductivity and capacity of the CFs, compared to the GFs.

All in all, melted particles flow on impact and spread on the substrate materials, indicating appropriate wetting of the LCT on the PEI matrix, the CFs and the GFs. This suggests that the plasma-spraying of the LCTs on composite structures is feasible; however, the challenge lies in limiting and balancing the degradation between coating and substrate.

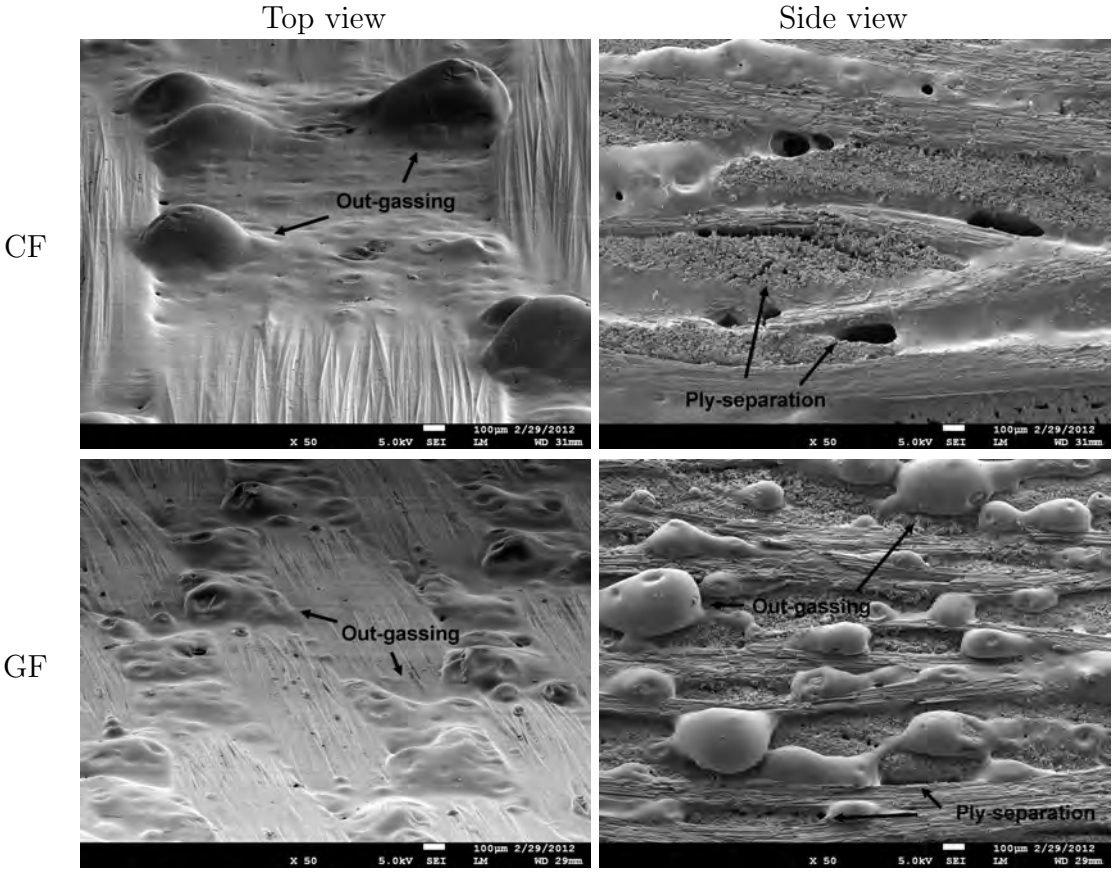

Figure 8.19 – SEM image showing the thermal damage on CF and GF reinforced PEI substrates during plasma-spraying

8.5 Conclusions

In this final chapter, the feasibility of using plasma-spraying as an alternative coating process for the deposition of liquid crystalline thermosets (LCTs) was investigated. It was observed that working in the oligomeric range of molecular weights improved the grindability of the LCT compared to the thermoplastic counterpart Vectra® A950, yielding particles within the recommended size-distribution and morphology.

Good wetting and flow of the sprayed LCT on aluminum and even on degraded pre-deposited LCT splats was observed, with good inter-splat coalescence. Therefore, it can be concluded that plasma-spaying of LCTs is feasible from a process point of view. On the other hand, the process has an intrinsic degree of defects, such as porosity and polymer degradation, together with a distribution of thermal histories for individual particles. As a result, optimization is required to minimize defects, and balance particle melting, flow, and degradation. It can be also concluded that, from a process perspective, plasma-spraying of LCTs on composite structures is feasible, since good wetting and flow on the PEI matrix and the carbon and glass

fibers was observed. In the case of composites, however, the process optimization window is more restricted due to the low degradation temperatures and thermal conductivity of both the substrate and the sprayed material.

The main parameter appeared to be the particle sizes of the feedstock, which should be limited to a distribution from approximately 25 to 60 µm. In addition, the production of feedstock should rely on optimizing the grinding process to avoid sieving, since the low density and high electrostatic behavior of the powder limits the extraction of a narrow particle size distribution through standard dry sieving. The selection and optimization of alternative particle size separation methods could be also considered.

Due to the incomplete crosslinking of the deposit, a less brittle coating was obtained, and the LCTs are potentially applicable without further post-curing. Nevertheless, re-melting of the LCTs in oven or by laser processes [200], for instance, can induce crosslinking, increase coating density, and reduce porosity, improving the overall coating properties.

General Conclusions

The properties of thermotropic liquid crystalline polymers (TLCPs) have been very attractive for the coating industry. Vectra® A950, for instance, one of the most studied TLCPs, posses high mechanical and chemical resistance, thermal and dimensional stability, very low permeability and moisture absorption, and inherent flame retardancy. The application of TLCPs as coatings, however, has been hindered by their low adhesion and difficult processability for this application. A new generation of crosslinkable Vectra-based TLCP oligomers end-capped with phenylethynyl reactive groups has the potential to overcome these disadvantages, retaining the intrinsic properties of TLCPs. The research presented in this thesis investigated the real potential of these liquid crystalline thermosets (LCTs) to overcome the aforementioned problems, and find applications as protective coatings in the aircraft/aerospace industry. A top-level question is then: *Can these phenylethynyl terminated LCTs find applications as coatings in aerospace?* The simple answer to this question is yes; however, to fully understand the scope of this answer, the question needs to be broken down and discussed in parts.

First, regarding the adhesion improvements offered by LCTs, a higher concentration of end-groups promotes the adhesion of the coating (Chapter 5), and increases compatibility with other polymers (Chapter 7). In addition, LCTs have good chemical compatibility to various typical substrate materials used in aerospace (Chapter 7 and Chapter 8); and, from the various pretreatments studied here, grit-blasting (GB) is the most beneficial for the LCTs. It was also found, however, that coating-substrate interfaces constitute paths for environmental attack (Chapter 7).

Second, concerning the processability improvements provided by LCTs, working in the oligomeric range allowed grinding into a powder with a particle-size distribution and morphology appropriate for powder coating techniques like atmospheric plasma spraying (APS). APS of LCTs, which do not require solvents and is suitable for industrialization, showed to be feasible from a process point of view (Chapter 8). On the other hand, the LCTs can not fully crosslink during APS, and require an additional curing step at elevated temperature, limiting applicability (Chapter 4 and Chapter 8). Based on the presented observations, it can be recommended to work with lower M_n oligomers, which can improve flow at impact (less energy required, thus less degradation), and reduce particle bounce-off [182]. In addition, powder production should rely on optimizing the grinding process to avoid sieving, since the low density and high electrostatic behavior of the powder limits the extraction of a narrow particle size distribution through standard dry sieving. The selection and

optimization of alternative particle size separation methods should be also considered. Finally, it is recommended to explore the use of electrostatic spraying, taking advantage of the highly electrostatic behavior of these polymers.

Third, based on the observed improvements in adhesion and processability, potential improvements in coating performance were investigated. Results showed that the end-group chemistry does not degrade the environmental resistance of the coating, and the LCTs can withstand the operating environments (Chapter 7). In addition, it was found that the macroscopic molecular orientation induced during processing of the oligomer is retained after curing (Chapter 6). The resulting oriented LCT coatings are highly anisotropic, allowing properties to be tuned.

During curing, however, several disadvantages in the performance of the coatings were observed. First, molecules form aggregates or "bundles" parallel to the substrate (which are not present in the thermoplastic coating), inducing a layered microstructure with a particular surface morphology (Chapter 4 and Chapter 6). These aggregates induce an anisotropic decrease in cohesive strength, since failures tend to occur at the aggregate-aggregate interfaces (Chapter 6 and Chapter 7); and they can also originate residual stresses and decrease adhesion if the coatings are over-cured (Chapter 4). The size of these aggregates is related to the M_n of the precursor oligomer, and affects the scratch behavior (Chapter 5). In addition, the effects of curing on the mechanical properties are highly restricted by an increasing M_n. Therefore, to improve the properties of cured coatings and reduce costs, it can be recommended to explore new liquid-crystalline backbone chemistries with higher characteristic temperatures and final mechanical properties, retaining the phenylethynyl end-group chemistry.

Finally, based on the above discussed points, potential applications for the coatings can now be proposed. These coatings constitute a passive protection, characterized mainly by a high chemical resistance, very low permeability, and good mechanical properties. They are potentially applicable as an intermediate or top coat in a system with multiple layers, which are required to extend coating durability (e. g., by active protection) and improve the environmental resistance of the coating-substrate interface. A typical application would be, therefore, the protection of light alloys or composites in structural and non-structural applications in contact with flowing liquids or gases. Examples include:

- Heat exchangers, air cooling units, gearbox housings, jet-engine air intakes, undercarriage components, shafts, and thrust nozzles.
- Parts exposed to the attack of aircraft fluids (e. g., Skydrol®, fuel, etc.), such as landing gear sections, flooring, doors, and hatches.
- Protection of polymeric-matrix composite parts, such as nose radome, fan blades, outlet guide vanes, bypass ducts, nose cone spinners, cowl doors, and composite control boxes and recorders.

There are also several non-aerospace-related potential applications, especially in the chemical industry: steam and jet turbines, pipelines and valves carrying particulate matter, and fluidized bed combustion systems (where there is mechanical contact and thermal, chemical, and physical reactions), pipelines carrying sand slurries, petroleum refining, and boiler tubes exposed to fly ash.

Appendix: Atmospheric Plasma Spraying (APS) Parameters

Table A.1 – Main APS parameters used for the preliminary spraying tests on grit-blasted aluminum substrates

Sample	**Current** (A)	**First gas** (SLPM)	**Second gas** (SLPM)	**Standoff distance** (mm)	**Torch speed** ($\frac{mm}{s}$)
S1	250	40 (Ar)	0	120	300
S2	250	40 (Ar)	0	120	300
S3	250	40 (Ar)	2 (N_2)	120	300
S4	250	50 (Ar)	4 (N_2)	120	300
S5	250	50 (Ar)	4 (N_2)	120	300
S6	250	45 (Ar)	0	120	100
S7	250	45 (Ar)	0	120	50
S8	250	45 (Ar)	0	120	50
S9	250	45 (Ar)	0	115	50
S10	250	50 (Ar)	2 (N_2)	115	50
S11	300	60 (Ar)	2 (H_2)	115	50
S12	300	60 (Ar)	1 (H_2)	115	50

SLPM = standard liters per minute

Table A.2 – Main APS process parameters used

Sample	**Current** (A)	**Fisrt gas** (SLPM)	**Second gas** (SLPM)	**Standoff distance** (mm)	**Torch speed** ($\frac{mm}{s}$)	**Coating passes**	**Carrier gas** (SLPM)
S15	250	50 (Ar)	0	120	50	2	5
S16	250	50 (Ar)	2 (H_2)	120	150	8	5
S17	300	60 (Ar)	1 (H_2)	120	150	4	5
S18	300	60 (Ar)	1 (H_2)	120	150	5	5
S19	300	60 (Ar)	1 (H_2)	120	150	3	4
S20	300	60 (Ar)	1 (H_2)	120	150	3	3
S21	300	60 (Ar)	1 (H_2)	150	150	3	3
S22	300	60 (Ar)	1 (H_2)	90	150	3	3
S23*	300	60 (Ar)	1 (H_2)	120	150	3	3
S24	300	60 (Ar)	1 (H_2)	120§	150	3	3
S25	300	60 (Ar)	1 (H_2)	120§	50	1	3
S26	300	60 (Ar)	1 (H_2)	120§	50	1	4
S27	300	60 (Ar)	1 (H_2)	150§	50	1	3
S28$^¤$	300	60 (Ar)	1 (H_2)	120§	50	2	N/A
S29	300	60 (Ar)	1 (H_2)	120§	50	5	3

SLPM = standard liters per minute

* = on polished steel substrate

¤ = on composite substrate§ = with steel plate

§ = with steel plate

Bibliography

[1] R. L. Twite and G. P. Bierwagen. Review of alternatives to chromate for corrosion protection of aluminum aerospace alloys. *Progress in Organic Coatings*, 33(2):91–100, 1998.

[2] M. Koudelkova, J. Augustynski, and H. Berthou. On the composition of the passivating films formed on aluminum in chromate solutions. *Journal of the Electrochemical Society*, 124(8):1165–1168, 1977.

[3] S. S. Wise, A. L. Holmes, Q. Qin, H. Xie, S. P. Katsifis, W. Douglas Thompson, and J. P. Wise Sr. Comparative genotoxicity and cytotoxicity of four hexavalent chromium compounds in human bronchial cells. *Chemical research in toxicology*, 23(2):365–372, 2010.

[4] J. Bauer. Complying with aircraft painting air emission regulations. Technical report, Burns & McDonnell, 2011.

[5] S. Uang, T. Shih, C. Chang, S. Chang, C. Tsai, and C. G. Deshpande. Exposure assessment of organic solvents for aircraft paint stripping and spraying workers. *Science of the Total Environment*, 356(1-3):38–44, 2006.

[6] G. Bierwagen, R. Brown, D. Battocchi, and S. Hayes. Active metal-based corrosion protective coating systems for aircraft requiring no-chromate pretreatment. *Progress in Organic Coatings*, 68(1-2):48–61, 2010.

[7] J. Hill, T. Markley, M. Forsyth, P. C. Howlett, and B. R. W. Hinton. Corrosion inhibition of 7000 series aluminium alloys with cerium diphenyl phosphate. *Journal of Alloys and Compounds*, 509(5):1683–1690, 2011.

[8] C. N. Panagopoulos, E. P. Georgiou, and A. G. Gavras. Corrosion and wear of 6082 aluminum alloy. *Tribology International*, 42(6):886–889, 2009.

[9] M. Iannuzzi and G. S. Frankel. Mechanisms of corrosion inhibition of aa2024-t3 by vanadates. *Corrosion Science*, 49(5):2371–2391, 2007.

[10] P. Wang, X. Dong, and D. W. Schaefer. Structure and water-barrier properties of vanadate-based corrosion inhibitor films. *Corrosion Science*, 52(3):943–949, 2010.

[11] M. Forsyth, T. Markley, D. Ho, G. B. Deacon, P. Junk, B. Hinton, and A. Hughes. Inhibition of corrosion on AA2024-T3 by new environmentally friendly rare earth organophosphate compounds. *Corrosion*, 64(3):191–197, 2008.

[12] J. W. Gooch. Compliant coatings for the aircraft industry. In *Proceedings of the Water-borne and Higher-solids Coatings Symposium*, pages 74–86, 1989.

[13] R. E. Wolf, C. J. Ray, G. McKay, and J. M. Butler. High solids coatings for exterior aircraft. *Prepr of Pap presented at a Jt Am Chem Soc/Chem Soc of Jpn Chem Congr Resins for Aerosp*, 40, 1979.

[14] D. F. Pulley. Compliant coatings for aerospace applications. In *Proceedings of the Water-borne and Higher-solids Coatings Symposium*, pages 67–73, 1989.

[15] http://www.americanchemistry.com. Last retrieved: June 2011.

[16] T. Wright. Aerospace coatings. *Coatings World*, August 2010. (Digital edition, available at: www.coatingsworld.com).

[17] S. Dixit, M. Chin, and R. Dixit. Coatings for polymer turbine blades. In *Proceedings of the International Thermal Spray Conference*, pages 1189–1194, 2009.

[18] K. Griffiths. Polyamides in aerospace industry. *Transactions of the Institute of Metal Finishing*, 85(5):235–236, 2007.

[19] K. J. Monaghan. Performance of rod sealing systems using chrome replacement coatings in landing gear shock absorbers, under conditions of short stroke reciprocating motion. In *BHR Group - 20th International Conference on Fluid Sealing*, pages 119–136, 2009.

[20] V. D. Athawale and R. S. Bailkeri. Liquid crystalline polymers and their coating properties. *European Coatings Journal*, (1), 2000.

[21] C. Carfagna, M. Giamberini, and E. Amendola. Can liquid crystalline polymers find application in the field of protective coatings? *Anti-Corrosion Methods and Materials*, 46(2):95–99, 1999.

[22] J. Gahde, R. Mix, H. Goering, G. Schulz, W. Funke, and U. Hermann. Increase in coating wet adhesion stability by highly-ordered polymers. *Journal of Adhesion Science and Technology*, 11(6):861–875, 1997.

[23] S. Okamoto. Newly developed LCP films fabricated by solvent-casting method. In *2005 Conference on High Density Microsystem Design and Packaging and Component Failure Analysis (HDP'05)*, art. no. 4017451, 2006.

[24] Ticona GmbH. Technical report B-241-E-10.2007: Vectra-TM, October 2007. (Available at: www.ticona.com).

[25] Y. Kurihara, H. Ohata, M. Kawaguchi, S. Yamazaki, and K. Kimura. Improvement of adhesion and long-term adhesive reliability of liquid crystalline polyester film by plasma treatment. *Journal of Applied Polymer Science*, 108(1):85–92, 2008.

[26] L. C. Sawyer and M. Jaffe. The structure of thermotropic copolyesters. *Journal of Materials Science*, 21(6):1897–1913, 1986.

[27] A. Knijnenberg, E. S. Weiser, T. L. StClair, E. Mendes, and T. J. Dingemans. Synthesis and characterization of aryl ethynyl terminated liquid crystalline oligomers and their cured polymers. *Macromolecules*, 39(20):6936–6943, 2006.

[28] A. Higgins. Adhesive bonding of aircraft structures. *International Journal of Adhesion and Adhesives*, 20(5):367–376, 2000.

[29] US Environmental Protection Agency (EPA). Technical report: Eliminating CFC-113 and methyl chloroform in aircraft maintenance procedures, July 2011. (Available at www.epa.gov/ozone/snap/icel/aircraft.html).

[30] J. G. Jr. Smith. Potential polymeric sphere construction materials for a spacecraft electrostatic shield. Technical report, NASA, Langley Research Center, Hampton, Virginia, 2006.

[31] M.S. Kiasat. *Curing shrinkage and residual stresses in viscoelastic thermosetting resins and composites.* Phd thesis, TU Delft, the Netherlands, 2000.

[32] G. Flodberg. *Barrier Properties of Liquid Crystalline Polymers and their Blends with PE and PETP.* PhD thesis, Royal Institute of Technology, Sweden, 2002.

[33] D. H. Weinkauf and D. R. Paul. Gas transport properties of thermotropic liquid-crystalline copolyesters. I. The effects of orientation and annealing. *Journal of Polymer Science, Part B: Polymer Physics*, 30(8):817–835, 1992.

[34] J. Y. Park, D. R. Paul, I. Haider, and M. Jaffe. Effect of thermal annealing on the gas permeability of HIQ-40 films. *Journal of Polymer Science, Part B: Polymer Physics*, 34(10):1741–1745, 1996.

[35] H. Ramathal and A. Lawal. Barrier properties of a thermotropic liquid crystalline polymer. *Journal of Applied Polymer Science*, 89(9):2457–2463, 2003.

[36] C. Lekakou, J. Cowley, and C. E. Dickinson. Injection moulding of self-reinforcing polymers and polymer blends. *Journal of Materials Science*, 32(5):1319–1324, 1997.

[37] S. D. Hudson and A. J. Lovinger. Transmission electron microscopic investigation of the morphology of a poly(hydroxybenzoate-co-hydroxynaphthoate) liquid crystal polymer. *Polymer*, 34(6):1123–1129, 1993.

[38] M. Iqbal. *All-aromatic liquid crystal thermosets and composites thereof.* PhD thesis, TU Delft, the Netherlands, 2010.

[39] W. D. Callister. *Materials Science and Engineering - An Introduction.* John Wiley & Sons, Inc., 2007.

[40] A. L. Tsykalo. *Thermophysical Properties of Liquid Crystals.* Gordon and Breach, 1991.

[41] F.C. Frank. Strength and stiffness of polymers. In *Proceedings of the Royal Society of London. Series A, Mathematical and Physical Sciences*, volume 319, pages 127–136, 1970.

[42] A. A. Collyer. Thermotropic liquid crystal polymers for engineering applications. *Materials Science and Technology*, 5(4):309–322, 1989.

[43] M. M. Giraud-Guille, G. Mosser, and E. Belamie. Liquid crystallinity in collagen systems in vitro and in vivo. *Current Opinion in Colloid and Interface Science*, 13(4):303–313, 2008.

[44] I. W. Hamley. Ordering in thin films of block copolymers: Fundamentals to potential applications. *Progress in Polymer Science (Oxford)*, 34(11):1161–1210, 2009.

[45] T. S. Chung. *Thermotropic Liquid Crystal Polymers; Thin-film polymerization, Characterization, Blends, and Applications.* Technomic, 2001.

[46] S. J. Picken, T. J. Dingemans, L. A. Madsen, O. Francescangeli, and E. T. Samulski. Uniaxial to biaxial nematic phase transition in a bent-core thermotropic liquid crystal by polarising microscopy. *Liquid Crystals*, 39(1):19–23, 2012.

[47] M. Born & E. Wolf. *Principles of Optics*. Cambridge University, 7th edition, 1999.

[48] J. R. Hobdell and A. H. Windle. Prediction of microstructure in liquid-crystalline polymers. *Journal of the Chemical Society, Faraday Transactions*, 91(16):2497–2505, 1995.

[49] G. Goldbeck-Wood, P. Coulter, J. R. Hobdell, M. S. Lavine, K. Yonetake, and A. H. Windle. Modelling of liquid crystal polymers at different length scales. *Molecular Simulation*, 21(2-3):143–160, 1998.

[50] G. D. Butzbach, J. H. Wendorff, and H. J. Zimmermann. Structure and structure formation of a main chain thermotropic polymer. *Polymer*, 27(9):1337–1344, 1986.

[51] J. Economy, D. Frich, and L. A. Schneggenburger. LCP polyesters vs. thermosetting polyesters: A paradigm for research in the 21st century. *Macromolecular Symposia*, 118:11–22, 1997.

[52] W. J. Jackson Jr. and H. F. Kuhfuss. Liquid crystal polymers - I. Preparation and properties of p-hydroxybenzoic acid copolyesters. *J Polym Sci Polym Chem Ed*, 14(8):2043–2058, 1976.

[53] C. A. Harper. *Modern Plastics Handbook*. Mc Graw-Hill, 1999.

[54] P. G. De Gennes. Possibilites offertes par la reticulation de polymeres en presence d'un cristal liquide. *Physics Letters A*, 28(11):725–726, 1969.

[55] G. G. Barclay and C. K. Ober. Liquid crystalline and rigid-rod networks. *Progress in Polymer Science (Oxford)*, 18(5):899–945, 1993.

[56] W. Meier. Structured polymer networks from o/w-microemulsions and liquid crystalline phases. *Langmuir*, 12(26):6341–6345, 1996.

[57] W. Meier. Polymer networks with lamellar structure. *Macromolecules*, 31(7):2212–2217, 1998.

[58] M. Warner and E. M. Terentjev. Nematic elastomers - A new state of matter? *Progress in Polymer Science (Oxford)*, 21(5):853–891, 1996.

[59] A. Shiota and C. K. Ober. Rigid rod and liquid crystalline thermosets. *Progress in Polymer Science (Oxford)*, 22(5):975–1000, 1997.

[60] C. Ortiz, R. Kim, E. Rodighiero, C. K. Ober, and E. J. Kramer. Deformation of a polydomain, liquid crystalline epoxy-based thermoset. *Macromolecules*, 31(13):4074–4088, 1998.

[61] J. S. Grebowicz. On the formation of liquid crystalline texture in epoxy resins. *Macromolecular Symposia*, 104:191–221, 1996.

[62] M. Giamberini, E. Amendola, and C. Carfagna. Epoxy-based liquid crystalline coatings. *Surface Coatings International Part B: Coatings International*, 81(1):14–18, 1998.

[63] C. Farren, M. Akatsuka, Y. Takezawa, and Y. Itoh. Thermal and mechanical properties of liquid crystalline epoxy resins as a function of mesogen concentration. *Polymer*, 42(4):1507–1514, 2001.

[64] A. E. Hoyt and B. C. Benicewicz. Rigid rod molecules as liquid crystal thermosets. I. Rigid rod amides. *Journal of Polymer Science, Part A: Polymer Chemistry*, 28(12):3403–3415, 1990.

[65] A. E. Hoyt and B. C. Benicewicz. Rigid rod molecules as liquid crystal thermosets. II. Rigid rod esters. *Journal of Polymer Science, Part A: Polymer Chemistry*, 28(12):3417–3427, 1990.

[66] C. M. Thompson and P. M. Hergenrother. Aryl ethynyl terminated imide oligomers and their cured polymers. *Macromolecules*, 35(15):5835–5839, 2002.

[67] A. J. Gavrin, C. L. Curts, and E. P. Douglas. High-temperature stability of a novel phenylethynyl liquid-crystalline thermoset. *Journal of Polymer Science, Part A: Polymer Chemistry*, 37(22):4184–4190, 1999.

[68] T. J. Dingemans, E. S. Weiser, and T. L. St. Clair. Liquid crystalline thermosets from ester, ester-imide, and ester-amide oligomers. United States Patent no. US6939940, 2005.

[69] M. Iqbal and T.J. Dingemans. High performance liquid crystal thermoset resins for structural composites and high themperature adhesives. In *Proceeding of the SAMPE*, 2008.

[70] M. Iqbal, A. Knijnenberg, H. Poulis, and T. J. Dingemans. All-aromatic liquid crystalline thermosets as high temperatures adhesives. *International Journal of Adhesion and Adhesives*, 30(8):682–688, 2010.

[71] T. J. Dingemans and M. Iqbal. Liquid crystal thermoset resins for high temperature composites and adhesives. *Plastics, Rubber and Composites*, 39(3-5):189–194, 2010.

[72] J. W. Connell, J. G. Smith Jr., and P. M. Hergenrother. Oligomers and polymers containing phenylethynyl groups. *Journal of Macromolecular Science - Reviews in Macromolecular Chemistry and Physics*, 40, 2000.

[73] P. M. Hergenrother. The use, design, synthesis, and properties of high performance/high temperature polymers: An overview. *High Performance Polymers*, 15(1):3–45, 2003.

[74] M. E. Wright, D. A. Schorzman, and L. E. Pence. Thermally curing aryl-ethynyl end-capped imide oligomers: Study of new aromatic end caps. *Macromolecules*, 33(23):8611–8617, 2000.

[75] C. C. Roberts, T. M. Apple, and G. E. Wnek. Curing chemistry of phenylethynyl-terminated imide oligomers: Synthesis of 13C-labeled oligomers and solid-state NMR studies. *Journal of Polymer Science, Part A: Polymer Chemistry*, 38(19):3486–3497, 2000.

[76] Y. Yang, L. Fan, X. Qu, M. Ji, and S. Yang. Fluorinated phenylethynyl-terminated imide oligomers with reduced melt viscosity and enhanced melt stability. *Polymer*, 52(1):138–148, 2011.

[77] E. P. Douglas. Structure-property relationships in liquid crystalline thermosets. *Polymer Reviews*, 46(2):127–141, 2006.

[78] J. A. Brogan. Thermal-spraying of polymers and polymer blends. *MRS Bulletin*, 25(7):48–53, 2000.

[79] L. S. Schadler, K. O. Laul, R. W. Smith, and E. Petrovicova. Microstructure and mechanical properties of thermally sprayed silica/nylon nanocomposites. *Journal of Thermal Spray Technology*, 6(4):475–485, 1997.

[80] V. D. Athawale, R. S. Bailkeri, and M. Athawale. Comb-like liquid crystalline polymers for coating applications. *Progress in Organic Coatings*, 42(3-4):132–141, 2001.

[81] D. Di Marzio, S. Chu, J. Klein, L. Poveromo, and J. Brogan. Liquid crystalline polymer (LCP) hybrid coating process development. In *Proceedings of the International SAMPE Symposium and Exhibition*, volume 47 I, pages 214–221, 2002.

[82] M. W. J. Van der Wielen, M. A. Cohen Stuart, G. J. Fleer, R. P. Nieuwhof, A. T. M. Marcelis, and E. J. R. Sudholter. A paint removal concept with side-chain liquid crystalline polymers as primer material. *Progress in Organic Coatings*, 41(1-3):157–165, 2001.

[83] K. Yoshida and T. Kakuchi. UV curable coatings with mesogenic side groups. *Progress in Organic Coatings*, 52(3):165–172, 2005.

[84] D. Frich and J. Economy. Aromatic liquid crystalline polymers: properties as adhesives and protective coatings. In *Proceedings of the ACS Division of Polymeric Materials Science and Engineering*, volume 69, pages 438–439, 1993.

[85] G. Henn, M. Stamm, H. Poths, M. Rucker, and J. P. Rabe. Influence of order in thin smectic polymer films on the structure at the surface. *Physica B: Condensed Matter*, 221(1-4):174–184, 1996.

[86] A. Muhlebach, J. Economy, R. D. Johnson, T. Karis, and J. Lyerla. Direct evidence for transesterification and randomization in a mixture of homopolyesters of poly-(HBA) and poly-(HNA) above 450°C. *Macromolecules*, 23(6):1803–1809, 1990.

[87] H. J. O'Donnell and D. G. Baird. In situ reinforcement of polypropylene with liquid-crystalline polymers: effect of maleic anhydride-grafted polypropylene. *Polymer*, 36(16):3113–3126, 1995.

[88] G. Flodberg, L. Axelson-Larsson, M.S. Hedenqvist, and U.W. Gedde. Liquid crystalline polymer pouches for local anaesthetic emulsion. *Packaging Technology and Science*, 14:159–170, 2001.

[89] C. Seidel, C. Damm, and H. Muenstedt. Surface modification of films of various high temperature resistant thermoplastics. *Journal of Adhesion Science and Technology*, 21(5-6):423–439, 2007.

[90] B. Wang, W. Eberhardt, and H. Kuck. Influence of argon plasma pretreatment on properties of liquid crystal polymer. *Journal of Materials Science*, 40(13):3535–3538, 2005.

[91] A. Jannesari, S. R. Ghaffarian, N. Mohammadi, F. A. Taromi, and A. Molaei. Liquid crystalline thermosets as binder for powder coatings - thermoanalytical study of the cure characteristics of a carboxylated main chain liquid crystalline oligoester. *Progress in Organic Coatings*, 50(4):213–223, 2004.

[92] Y. Bao and D. T. Gawne. Plasma spray deposition of Nylon 11 coatings. *Transactions of the Institute of Metal Finishing*, 69(3):80–85, 1991.

[93] E. Petrovicova and L. S. Schadler. Thermal spraying of polymers. *International Materials Reviews*, 47(4):169–190, 2002.

[94] R.J. Young and P.A. Lovell. *Introduction to Polymers*. CRC Press, 1991.

[95] H. Ezuber, A. El-Houd, and F. El-Shawesh. A study on the corrosion behavior of aluminum alloys in seawater. *Materials and Design*, 29(4):801–805, 2008.

[96] http://www.alfun.eu. Last retrieved: June 2011.

[97] http://www.corrosionist.com. Last retrieved: June 2011.

[98] L. D. Hefti. Commercial airplane applications of superplastically formed AA5083 aluminum sheet. *Journal of Materials Engineering and Performance*, 16(2):136–141, 2007.

[99] http://www.aluminiumleader.com. Last retrieved: June 2011.

[100] http://www.aerospacemetals.com. Last retrieved: June 2011.

[101] http://www.aviationmetals.net. Last retrieved: June 2011.

[102] F. Pitt. Developing a superplastic forming application using aluminum tube. *Journal of Materials Engineering and Performance*, 13(6):720–726, 2004.

[103] E. Hombergsmeier. Magnesium suitable for aeronautic applications? *Light Metal Age*, 67(3):34–39, 2009.

[104] X. Li and B. Bhushan. A review of nanoindentation continuous stiffness measurement technique and its applications. *Materials Characterization*, 48(1):11–36, 2002.

[105] B. Bhushan and X. Li. Nanomechanical characterisation of solid surfaces and thin films. *International Materials Reviews*, 48(3):125–164, 2003.

[106] S.K. Sinha and B.J. Briscoe, editors. *Polymer Tribology*. Imperial College Press, 2009.

[107] W. C. Oliver and G. M. Pharr. Improved technique for determining hardness and elastic modulus using load and displacement sensing indentation experiments. *Journal of Materials Research*, 7(6):1564–1580, 1992.

[108] R. Saha and W. D. Nix. Effects of the substrate on the determination of thin film mechanical properties by nanoindentation. *Acta Materialia*, 50(1):23–38, 2002.

[109] B. J. Briscoe and S. K. Sinha. Scratch resistance and localised damage characteristics of polymer surfaces -A review. *Materialwissenschaft und Werkstofftechnik*, 34(10-11):989–1002, 2003.

[110] R. L. Browning, G. Lim, A. Moyse, H. Sue, H. Chen, and J. D. Earls. Quantitative evaluation of scratch resistance of polymeric coatings based on a standardized progressive load scratch test. *Surface and Coatings Technology*, 201(6):2970–2976, 2006.

[111] C. Gauthier, S. Lafaye, and R. Schirrer. Elastic recovery of a scratch in a polymeric surface: Experiments and analysis. *Tribology International*, 34(7):469–479, 2001.

[112] H. Jiang, R. Browning, and H. . Sue. Understanding of scratch-induced damage mechanisms in polymers. *Polymer*, 50(16):4056–4065, 2009.

[113] C. Xiang, H. . Sue, J. Chu, and B. Coleman. Scratch behavior and material property relationship in polymers. *Journal of Polymer Science, Part B: Polymer Physics*, 39(1):47–59, 2001.

[114] S. L. Zhang and J. C. M. Li. Slip process of stick-slip motion in the scratching of a polymer. *Materials Science and Engineering A*, 344(1-2):182–189, 2003.

[115] ISO 4587:2003. Determination of tensile lap-shear strength of rigid to rigid bonded assemblies, 2003.

[116] S. J. García and J. Suay. Application of electrochemical techniques to study the effect on the anticorrosive properties of the addition of ytterbium and erbium triflates as catalysts on a powder epoxy network. *Progress in Organic Coatings*, 57(3):273–281, 2006.

[117] ASTM B117-11. Standard practice for operating salt-spray (fog) apparatus, 2011.

[118] M. Iqbal, B. Norder, E. Mendes, and T. J. Dingemans. All-aromatic liquid crystalline thermosets with high glass transition temperatures. *Journal of Polymer Science, Part A: Polymer Chemistry*, 47(5):1368–1380, 2009.

[119] A. Knijnenberg. New liquid crystalline thermoset resins for aerospace applications. Master's thesis, TU Delft, the Netherlands, 2004.

[120] S. Z. D. Cheng. Kinetics of mesophase transitions in thermotropic copolyesters. I. Calorimetric study. *Macromolecules*, 21(8):2475–2484, 1988.

[121] T. . Chung, M. Cheng, S. H. Goh, M. Jaffe, and G. W. Calundann. Revisit the crystallization mechanism of Vectra, a liquid crystal polymer. *Journal of Applied Polymer Science*, 72(9):1139–1150, 1999.

[122] Y. Ting, C. Liu, S. Park, H. Jiang, P. F. Nealey, and A. E. Wendt. Surface roughening of polystyrene and poly(methyl methacrylate) in Ar/O2 plasma etching. *Polymers*, 2(4):649–663, 2010.

[123] M. Sumiya, R. Bruce, S. Engelmann, F. Weilnboeck, and G. S. Oehrlein. Study of 193 nm photoresist degradation during short time fluorocarbon plasma exposure. I. Studies of modified layer formation. *Journal of Vacuum Science and Technology B: Microelectronics and Nanometer Structures*, 26(5):1637–1646, 2008.

[124] K. Kim, Y. Kim, N. R. Ko, and S. Choe. Effect of molecular weight on the surface morphology of crosslinked polymer particles in the RITP-dispersion polymerization. *Polymer*, 52(24):5439–5444, 2011.

[125] B. B. Sauer, W. G. Kampert, and R. S. McLean. Thermal and morphological properties of main chain liquid crystalline polymers. *Polymer*, 44(9):2721–2738, 2003.

[126] S. Dreher, H. G. Zachmann, C. Riekel, and P. Engstrøm. Determination of the chain orientation in liquid crystalline polymers by means of microfocus X-ray scattering measurements. *Macromolecules*, 28(21):7071–7074, 1995.

[127] K. Li, B. Y. Ni, and J. C. M. Li. Stick-slip in the scratching of styrene-acrylonitrile copolymer. *Journal of Materials Research*, 11(6):1574–1580, 1996.

[128] S. J. Bull. Failure modes in scratch adhesion testing. *Surface and Coatings Technology*, 50(1):25–32, 1991.

[129] W. Liu and C. Carfagna. Synthesis of liquid crystalline epoxy oligomers: Effect of molecular weight on the phase behavior. *Macromolecular Rapid Communications*, 22(13):1058–1062, 2001.

[130] X. Qu, L. Fan, M. Ji, and S. Yang. Fluorinated pmr polyimides with improved melt processability and impact toughness. *High Performance Polymers*, 23(2):151–159, 2011.

[131] S. J. Bull. Nanoindentation of coatings. *Journal of Physics D: Applied Physics*, 38(24):R393–R413, 2005.

[132] T. Chung, D. Nest, D. B. Graves, F. Weilnboeck, R. L. Bruce, G. S. Oehrlein, D. Wang, M. Li, and E. A. Hudson. Electron, ion, and vacuum ultraviolet photon effects in 193 nm photoresist surface roughening. *Journal of Physics D: Applied Physics*, 43(27), 2010.

[133] G. P. Patsis, E. Gogolides, and K. van Werden. Effects of photoresist polymer molecular weight and acid-diffusion on line-edge roughness. *Japanese Journal of Applied Physics, Part 1: Regular Papers and Short Notes and Review Papers*, 44(8):6341–6348, 2005.

[134] S. J. García, M. T. Rodríguez, R. Izquierdo, and J. Suay. Evaluation of cure temperature effects in cataphoretic automotive primers by electrochemical techniques. *Progress in Organic Coatings*, 60(4):303–311, 2007.

[135] J. Michler, R. Rabe, J. . Bucaille, B. Moser, P. Schwaller, and J. . Breguet. Investigation of wear mechanisms through in situ observation during microscratching inside the scanning electron microscope. *Wear*, 259(1-6):18–26, 2005.

[136] M. Cailler and G. H. Lee. Scratch adhesion test of magnetron-sputtered copper coatings on aluminium substrates: Effects of the surface preparation. *Thin Solid Films*, 168(2):193–205, 1989.

[137] A. Anwer and A. H. Windle. Orientation kinetics of thermotropic main-chain liquid-crystalline polymers in a magnetic field. *Polymer*, 32(1):103–108, 1991.

[138] A. Anwer and A. H. Windle. Magnetic orientation and microstructure of main-chain thermotropic copolyesters. *Polymer*, 34(16):3347–3357, 1993.

[139] R. V. Talroze, V. P. Shibayev, and N. A. Plate. Thermotropic liquid crystalline polymers in electric and magnetic fields. Review. *Polymer Science U.S.S.R.*, 25(12):2863–2888, 1983.

[140] A. Romo-Uribe and A. H. Windle. "log-rolling" alignment in main-chain thermotropic liquid crystalline polymer melts under shear: An in situ WAXS study. *Macromolecules*, 29(19):6246–6255, 1996.

[141] W. R. Burghardt, E. F. Brown, M. L. Auad, and J. A. Kornfield. Molecular orientation of a commercial thermotropic liquid crystalline polymer in simple shear and complex flow. *Rheologica Acta*, 44(5):446–456, 2005.

[142] S. Rendon, W. R. Burghardt, R. A. Bubeck, L. S. Thomas, and B. Hart. Mechanical and morphological anisotropy in injection molding of thermotropic liquid crystalline copolyesters. *Polymer*, 46(23):10202–10213, 2005.

[143] W. Zhou, J. A. Kornfield, and W. R. Burghardt. Shear aligning properties of a main-chain thermotropic liquid crystalline polymer. *Macromolecules*, 34(11):3654–3660, 2001.

[144] H. Tu, G. Goldbeck-Wood, and A. H. Windle. Simulation of texture evolution for nematic liquid crystalline polymers under shear flow. *Liquid Crystals*, 29(3):335–345, 2002.

[145] M. J. Troughton, G. R. Davies, and I. M. Ward. Dynamic mechanical properties of random copolyesters of 4-hydroxybenzoic acid and 2-hydroxy 6-naphthoic acid. *Polymer*, 30(1):58–62, 1989.

[146] K. F. Wissbrun and H. N. Yoon. Similarity of dynamic mechanical transitions of thermotropic polyesters in extension and torsion. *Polymer*, 30(12):2193–2197, 1989.

[147] T. W. Wu. Microscratch and load relaxation tests for ultra-thin films. *Journal of Materials Research*, 6(2):407–425, 1991.

[148] D. Barnes, S. Johnson, R. Snell, and S. Best. Using scratch testing to measure the adhesion strength of calcium phosphate coatings applied to poly(carbonate urethane) substrates. *Journal of the Mechanical Behavior of Biomedical Materials*, 6(2):128–138, 2011.

[149] A. Vencl, S. Arostegui, G. Favaro, F. Zivic, M. Mrdak, S. Mitrovi, and V. Popovic. Evaluation of adhesion/cohesion bond strength of the thick plasma spray coatings by scratch testing on coatings cross-sections. *Tribology International*, 44(11):1281–1288, 2011.

[150] F. Awaja, M. Gilbert, G. Kelly, B. Fox, and P. J. Pigram. Adhesion of polymers. *Progress in Polymer Science (Oxford)*, 34(9):948–968, 2009.

[151] A. Baldan. Adhesively-bonded joints and repairs in metallic alloys, polymers and composite materials: Adhesives, adhesion theories and surface pretreatment. *Journal of Materials Science*, 39(1):1–49, 2004.

[152] S. Römhild, G. Bergman, and M. S. Hedenqvist. Transport and adhesion properties of an unlined and a liquid-crystalline polymer-lined vinyl ester thermoset exposed to severe environments. *Journal of Applied Polymer Science*, 95(4):797–806, 2005.

[153] D. H. Weinkauf and D. R. Paul. Gas transport properties of thermotropic liquid-crystalline copolyesters. II. The effects of copolymer composition. *Journal of Polymer Science, Part B: Polymer Physics*, 30(8):837–849, 1992.

[154] B.C. Benicewicz. Magnetic field orientation of liquid crystalline epoxy thermosets. *Macromolecules*, 31:4730–4738, 1998.

[155] S. N. Dub and M. L. Trunov. Determination of viscoelastic material parameters by step-loading nanoindentation. *Journal of Physics D: Applied Physics*, 41(7), 2008.

[156] G. Guerriero, R. Alderliesten, T. Dingemans, and R. Benedictus. Thermotropic liquid crystalline polymers as protective coatings for aerospace. *Progress in Organic Coatings*, 70(4):245–251, 2011.

[157] S. Wu. *Polymer Interface and Adhesion*. Marcel Dekker, Inc., 1st edition, 1982.

[158] J. D. Venables. Adhesion and durability of metal-polymer bonds. *Journal of Materials Science*, 19(8):2431–2453, 1984.

[159] B. Dietsch, C. Theodore, D. Klosterman, T. Tong, R. Chartoff, and P. Hood. Surface preparation of aluminum for adhesive bonding of a liquid crystal thermoset. 46 I:145–157, 2001.

[160] K. Omata, K. Maeda, T. Oda, and Y. Otaka. Adhesion of paint films to anodic-oxide films on aluminium. *Aluminium Dusseldorf*, 57(12):811–813, 1981.

[161] O. Borrero-López, M. Hoffman, A. Bendavid, and P. J. Martin. Substrate effects on the mechanical properties and contact damage of diamond-like carbon thin films. *Diamond and Related Materials*, 19(10):1273–1280, 2010.

[162] M. D. Thouless. An analysis of spalling in the microscratch test. *Engineering Fracture Mechanics*, 61(1):75–81, 1998.

[163] A. J. Hsieh, J. C. Nelson, S. K. Venkatraman, D. L. Kohlstedt, and W. W. Gerberich. Continuous microscratch measurements of thin film adhesion strengths. *Journal of Adhesion Science and Technology*, 7(12 pt 2):1279–1292, 1993.

[164] S. Venkataraman, D. L. Kohlstedt, and W. W. Gerberich. Microscratch analysis of the work of adhesion for Pt thin films on NiO. *Journal of Materials Research*, 7(5):1126–1132, 1992.

[165] S. Venkataraman, D. L. Kohlstedt, and W. W. Gerberich. Continuous microscratch measurements of the practical and true works of adhesion for metal/ceramic systems. *Journal of Materials Research*, 11(12):3133–3145, 1996.

[166] S. K. Venkataraman, D. L. Kohlstedt, and W. W. Gerberich. Metal-ceramic interfacial fracture resistance using the continuous microscratch technique. *Thin Solid Films*, 223(2):269–275, 1993.

[167] W. Gu and Z. Yao. Evaluation of surface cracking in micron and sub-micron scale scratch tests for optical glass BK7. *Journal of Mechanical Science and Technology*, 25(5):1167–1174, 2011.

[168] O. Desa and S. Bahadur. Material removal and subsurface damage studies in dry and lubricated single-point scratch tests on alumina and silicon nitride. *Wear*, 225-229(PART II):1264–1275, 1999.

[169] M. Klecka and G. Subhash. Grain size dependence of scratch-induced damage in alumina ceramics. *Wear*, 265(5-6):612–619, 2008.

[170] V. Le Houérou, J. . Sangleboeuf, S. Dériano, T. Rouxel, and G. Duisit. Surface damage of soda-lime-silica glasses: Indentation scratch behavior. *Journal of Non-Crystalline Solids*, 316(1):54–63, 2003.

[171] S. J. Bull. Failure mode maps in the thin film scratch adhesion test. *Tribology International*, 30(7):491–498, 1997.

[172] Vectra® A950 datasheet, 2008. (Available at www.ides.com).

[173] G. Pritchard. *Anti-corrosion polymers: PEEK, PEKK and other polyaryls*. RAPRA, 1995.

[174] A. Goldchmidt and H. J. Streitberger. *Handbook on Basics of Coating Technology*. William Andrew Publishing, 2003.

[175] N. Liberto, editor. *User's Guide to Powder Coating*. Society of Manufacturing, 4th edition, 2003.

[176] Y. Bao. *Plasma spray deposition of polymer coatings*. PhD thesis, Brunel University, London, 1995.

[177] H. Herman, S. Sampath, and R. McCune. Thermal spray: Current status and future trends. *MRS Bulletin*, 25(7):17–25, 2000.

[178] M. Ivosevic, R. A. Cairncross, and R. Knight. 3D predictions of thermally sprayed polymer splats: Modeling particle acceleration, heating and deformation on impact with a flat substrate. *International Journal of Heat and Mass Transfer*, 49(19-20):3285–3297, 2006.

[179] M. Ivosevic, V. Gupta, J. A. Baldoni, R. A. Cairncross, T. E. Twardowski, and R. Knight. Effect of substrate roughness on splatting behavior of HVOF sprayed polymer particles: Modeling and experiments. *Journal of Thermal Spray Technology*, 15(4):725–730, 2006.

[180] S. Sampath and R. McCune. Thermal-spray processing of materials. *MRS Bulletin*, 25(7):12–16, 2000.

[181] M. Ivosevic. *Splat formation during thermal spraying of polymer particles: Mathematical modeling and experimental analysis*. PhD thesis, Drexel University, Philadelphia, July 2006.

[182] Y. Bao, T. Zhang, and D. T. Gawne. Influence of composition and process parameters on the thermal spray deposition of UHMWPE coatings. *Journal of Materials Science*, 40(1):77–85, 2005.

[183] E. Lugscheider, C. Herbst, and A. Fischer. Thermal spraying of high performance thermoplastics. In *Proceedings of the International Thermal Spray Conference*, volume 1, pages 19–24, 1998.

[184] T. Zhang, D. T. Gawne, and Y. Bao. The influence of process parameters on the degradation of thermally sprayed polymer coatings. *Surface and Coatings Technology*, 96(2-3):337–344, 1997.

[185] B. P. Withy, M. M. Hyland, and B. J. James. The effect of surface chemistry and morphology on the properties of HVAF PEEK single splats. *Journal of Thermal Spray Technology*, 17(5-6):631–636, 2008.

[186] G. Zhang, W. Li, M. Cherigui, C. Zhang, H. Liao, J. Bordes, and C. Coddet. Structures and tribological performances of PEEK (poly-ether-ether-ketone)-based coatings designed for tribological application. *Progress in Organic Coatings*, 60(1):39–44, 2007.

[187] C. Pierlot, L. Pawlowski, M. Bigan, and P. Chagnon. Design of experiments in thermal spraying: A review. *Surface and Coatings Technology*, 202(18):4483–4490, 2008.

[188] A. Vardelle, C. Moreau, and P. Fauchais. Dynamics of deposit formation in thermal-spray processes. *MRS Bulletin*, 25(7):32–37, 2000.

[189] T. Palathai, J. Tharajak, and N. Sombatsompop. Hardness, adhesion index and microstructure of PEEK coating on Al or Fe substrate by LVOF flame spray. *Materials Science and Engineering A*, 485(1-2):66–73, 2008.

[190] Y. Wang, C. Li, and A. Ohmori. Influence of substrate roughness on the bonding mechanisms of high velocity oxy-fuel sprayed coatings. *Thin Solid Films*, 485(1-2):141–147, 2005.

[191] H. Liu, E. J. Lavernia, and R. H. Rangel. Modeling of molten droplet impingement on a non-flat surface. *Acta Metallurgica Et Materialia*, 43(5):2053–2072, 1995.

[192] A. A. Syed, A. Denoirjean, B. Hannoyer, P. Fauchais, P. Denoirjean, A. A. Khan, and J. C. Labbe. Influence of substrate surface conditions on the plasma sprayed ceramic and metallic particles flattening. *Surface and Coatings Technology*, 200(7):2317–2331, 2005.

[193] J. R. Fincke and R. A. Neiser. Advanced diagnostics and modeling of spray processes. *MRS Bulletin*, 25(7):26–31, 2000.

[194] M. Ivosevic, R. A. Cairncross, and R. Knight. Melting and degradation of nylon-11 particles during HVOF combustion spraying. *Journal of Applied Polymer Science*, 105(2):827–837, 2007.

[195] Y. Bao and D. T. Gawne. Process modelling of thermal spray deposition of thermosets. *Surf.Eng.*, 11(3):215–222, 1995.

[196] Y. Bao, D. T. Gawne, and T. Zhang. Effect of feedstock particle size on the heat transfer rates and properties of thermally sprayed polymer coatings. *Transactions of the Institute of Metal Finishing*, 73(pt 4):119–124, 1995.

[197] Cetex® PEI datasheet, 2008. (Provided by: Tencate Advance Composites, Inc.).

[198] A. Offringa. Thermoplastics in aerospace, new products through innovative technology. *SAMPE Journal*, 41(7):19–27, 2005.

[199] M. Lu, L. Ye, and Y. Mai. Thermal deconsolidation of thermoplastic matrix composites. II. Migration of voids and reconsolidation. *Composites Science and Technology*, 64(2):191–202, 2004.

[200] C. Zhang, G. Zhang, V. Ji, H. Liao, S. Costil, and C. Coddet. Microstructure and mechanical properties of flame-sprayed PEEK coating remelted by laser process. *Progress in Organic Coatings*, 66(3):248–253, 2009.

Acknowledgments

This *trip* has come to the end. I have been cycling Dutch paths for four years and I have met some wonderful people along the way. Some people have made it more exciting and some have made it unforgettable; with some I spent a great deal of the time, and with others time was too short. But the length was not related to the intensity, and **all** of them have made this trip what it was: Amazing.

I would like to thank the people that joined me in this adventure not in order of importance (if there is such a thing), but in a (more or less) chronological order.

Despite everything, the one person that ignited in me the motivation to cycle Delft's roads was a girl called Indriati. I am forever thankful for how you changed the course of my world.

Once in the Netherlands, the first person on this bike-path was Gemma. Since the moment that (out of the blue) I knocked on the door of her office and explained why I was there, she has been one of the most helpful travel companions along this four-years trip. But most important of all, she directed me to the next person on the path. Thanks a lot!

She put me on the way of René Alderliesten. He was "the" person that *offered* me the bike and helped me find the way along. Of course, the next person on the path is Rinze Benedictus. He was the one who *gave* me the bike and the freedom to follow my instincts to find the way. Thanks to both of you for trusting me!

Then, I met the bunch of guys from Clean-Era. Ronald, Michiel, Hui, Marios, Francois, Durk, Chara, Sonell, Marcel, Arvind, and Dipanjay. You are some of the oldest friends I have in this continent! How can I thank you for that?

Soon I learned to prepare home-made supplies in the lab, and for that I thank Theo, Chris, Maruti, and Mazhar. Thanks for the *cooking* lessons!

Right after that, I met the guys from the Structural Integrity and Composites group (ex-Aerospace Materials). As it usually happens in this academic environment, people leave and new people come; but they never replace each other... Along the way, I have been cycling together with many friends (who were more than just colleagues!). Some already **left**:

Amir, Riccardo, Rik-Jan, Ligeia, Patricio, Gianni, Alessandro, Maria Luisa, Bas, Chris, Arjan, Greg W., Cory, Sharif, and Milan. Some are **still** around: Daniel, Freddy, Bea, Maria, Adrian L.Q., Adrian F.V., Freek, Nat, Natcha, Lei, Huajie, Paola, Marcelo, Mayank, Nick, Greg. R., Konstantin, Ilhan, Morteza, Alfonso, Irene, Derek, Srikant, Frederik, Vincent, Roger, Jos, Marianne, Roger, and Calvin... You made me feel at home: $Thanks \times 10^{45}$.

One of the most important groups of people I met is the technicians. Without them, it would have been impossible to **fix** my bike on the way, to build some new parts, and to TEST them. I am thankful to them also for having made it not just friendly, but also a lot of fun: so thanks to Frans, Anemike, Bob, Berthil, Hans, Johan, Fred, Cees, Peter, Rob, Ed, and Herman.

I biked quite a bit outside the aerospace bike-paths, where I met Raymond, Erik, and Ron. I also traveled some long paths to other countries, where I biked together with Thomas Warda. Thanks for letting me use your bikes there!

After some time, when the destination was not yet at sight, I met a person on the way that helped me pedaling *up-hill*: Santiago. Thanks for the unselfish help and fruitful discussions!

Finally, when I could see the finish-line, some people also biked together with me to make sure things went well until the end: John-Alan and Hamideh (the first *civilians* to **entirely** read my book).

And at the very end of the `voyage`: Thanks a lot to the doctoral committee members, who spared their time to review this report of my trip and offered me the chance to have rich and fruitful discussions.

It has been an honor to bike side-by-side with each of you!

-Gus.

About the Author

"Left or right?" the author said. He chose the right; and nine months later he was born. It was the 7th of December 1981, in Buenos Aires, Argentina. After more right and some left turns, he obtained his masters degree with honors in the field of materials science at the *Prof. Jorge Sabato Institute of Technology* in August 2008. He performed his final master's project in the topic of photonic nanostructures manufactured in thin polymeric films by focused ion-beam lithography at the *Max Planck Institute for Polymer Research*, in Mainz, Germany. In September 2008, he started his Ph.D. research in the group of Aerospace Materials (currently Structural Integrity and Composites) at the *Delft University of Technology*, in the Netherlands, under the supervision of Prof. dr. ir. Rinze Benedictus and Dr. ir. René Alderliesten. During his time as a Ph.D. researcher in Delft, he learned to ride a bike without hands (among other important things), and kept turning left and right.